UNIVERSITY OF OKLAHOMA

GRADUATE COLLEGE

INTERVALLEY SCATTERING IN III-V HETEROSTRUCTURES AND ITS APPLICATION TO VALLEY PHOTOVOLTAIC HOT CARRIER SOLAR CELLS

A DISSERTATION

SUBMITTED TO THE GRADUATE FACULTY

in partial fulfillment of the requirements for the

Degree of

DOCTOR OF PHILOSOPHY

By

KYLE R. DORMAN
Norman, Oklahoma
2022

INTERVALLEY SCATTERING IN III-V HETEROSTRUCTURES AND ITS APPLICATION TO VALLEY PHOTOVOLTAIC HOT CARRIER SOLAR CELLS

A DISSERTATION APPROVED FOR THE
HOMER L. DODGE DEPARTMENT OF PHYSICS AND ASTRONOMY

BY THE COMMITTEE CONSISTING OF

Dr. Ian R. Sellers, Chair

Dr. Michael B. Santos, Chair

Dr. Kieran Mullen

Dr. Eric R. I. Abraham

Dr. Jivtesh Garg

Acknowledgments

During my time at the University of Oklahoma, I have had the great fortune to become involved in the development of photovoltaics at a crucial time for the field of renewable energy. Throughout the many challenges presented by the pandemic and the difficulties of striding forwards alongside the leading edge of third generation solar cells, which has been at times both frustrating and exhilarating as I grappled with novel developments, I have felt proud to contribute to the scientific community. And very thankful for the support of my colleagues and mentors at times when the answers seemed out of my grasp, both inside and outside of the laboratory.

To **Professor Michael B. Santos**, I am eternally grateful for your guidance from my earliest days as a graduate student to the finalization of my dissertation. It was you who helped me find my feet in this field and brought me into the project that is presented in this thesis. And to **Professor Ian R. Sellers**, I am thankful for your supervision and advice throughout the length of my many months of experimentation and the attendant process slowly drawing out comprehension from the resultant data. As my advisors, your help has been irreplaceable.

I am grateful to **Dr. Hamidreza Esmaielpour** for both his efforts in furthering the field of hot carrier solar cells and his advice and training during our time together in the Photovoltaic Materials and Devices Group. In these past few years my research has come far, and I am grateful to affirm that this accomplishment began by building upon the solid ground of his research. **Dr. Vincent R. Whiteside** has been a tremendous help in countless ways, a steady guide in unexpectedly turbulent times. I have relied upon

his experience many times, be it to solve problems in the lab or to navigate the bureaucratic aspects of the scientific process.

And though there has always been substantial physical distance between our places of work, it cannot be left unsaid the impact our collaborator **Professor David K. Ferry** at Arizona State University has made upon my research. My thanks for both his crucial theoretical calculations and the keen insights he shared during our discussions.

I am grateful to the other members of my doctoral committee, who have provided both advice and flexibility at times when both have been required. My thanks to *Professor Jivtesh Garg*, *Professor Kieran Mullen,* and *Professor Eric R. I. Abraham*.

And to my colleagues who I have worked together with and relied upon in ways large and small, I offer my thanks. With particular gratitude towards my most immediate compatriots: *Dr. Collin Brown*, *Dr. Tetsuya Mishima*, *Dr. Brandon Durant*, *Hadi Afshari*, *Shashi Sourabh* and *Jeremy Massengale*. And though our time together has been more limited I would also like to thank those who later joined the photovoltaics group: *Israa Yusuf*, *Megh Khanal*, *Hasan Ahmed*, *Sergio Chacon* and *Sethulakshmi Sudhakara*. Your companionship and aid have been greatly appreciated.

Finally, I am grateful to my parents and my brother for their support, and their belief and trust in me throughout my studies. My thanks and love to you, Mom, Dad, Logan. To you and to all my wider family who have expressed their interest and joy at my research and publications thus far, I deeply appreciate everything you have done for me. It is my hope that through this dissertation I may once more share my efforts not only with the scientific community and the general public, but with all of you as well.

Table of Contents

List of Figures

Abstract

The efficiency limit of 33% for a single gap solar cell is not fundamental. Mitigation of thermalization losses which occur when high energy ‘hot’ carriers are only extracted at the same energy as low energy carriers is a viable route towards a solar power conversion efficiency as high as 66%. Previous efforts to develop such a hot carrier solar cell have focused on slowing thermalization through restricting electron-phonon interactions in quantum well structures. This bottleneck effect enables hot phonons to reheat the carrier distribution under high illumination powers. Despite recent success in demonstrating hot carrier effects, maintaining a population of carriers at enhanced energy under more practical conditions (room temperature and weak illumination) remains a challenge.

Here, after observing that hot carrier behavior is affected by scattering to high energy valleys of the conduction band in InAs/AlAsSb multi-quantum well structures, a more robust means of hot carrier maintenance is examined in proof-of-principle InGaAs based heterostructure devices. In these systems, photogenerated hot carriers are preferentially transferred to high energy valleys in the band structure via intervalley phonon scattering rather than thermalizing to the conduction band edge via LO phonon emission. And through inclusion of a doping profile to generate an electric field across the absorber during operation, low energy carriers can also transfer to the high energy upper valleys: the Gunn Effect.

These two mechanisms of intervalley scattering, via intervalley phonons and via the Gunn Effect, result in a simple device structure that demonstrates detectable hot carrier

behavior at room temperature and at low incident illumination power. These mechanisms are investigated comprehensively through a series of structures that enable control of the electric field strength (via altered absorber thickness) to better understand how to leverage the benefits of intervalley transfer for hot carrier maintenance, and to the extraction pathway (via altered top n^+ layer) to reveal how to overcome the complexities of extracting from an upper valley. While operational photovoltaic devices are yet to be realized, this work provides strong evidence for their practicality and routes toward the realization of such valley photovoltaic hot carrier solar cells.

Chapter **1**

An Introduction to Hot Carrier Solar Cells

1.1. The Single Gap Limit

To provide the electricity required for present day infrastructure and the global society that relies upon it, solar energy is becoming an increasingly important contributor. The sun provides an incredible amount of energy, and photovoltaic solar cells allow for direct and immediate transformation of sunlight to electrical power. Despite the majority of commercial photovoltaic modules being limited to below 30% solar power conversion efficiency [1], and the difficulties of competing economically with more entrenched power generation technologies, the total photovoltaic capacity worldwide has increased by more than tenfold since 2010 [2]. For both the expanding terrestrial requirements and the continued interest in solar photovoltaics for space applications where efficient thin film solar cells may pay for their weight many times over in electricity production, continued development of solar cell technology is a necessity. In particular, an improvement in efficiency is both plausible and would be extremely beneficial, as an average commercial crystalline silicon photovoltaic module feature ~20% efficiency and has an energy payback time of at least three years [3].

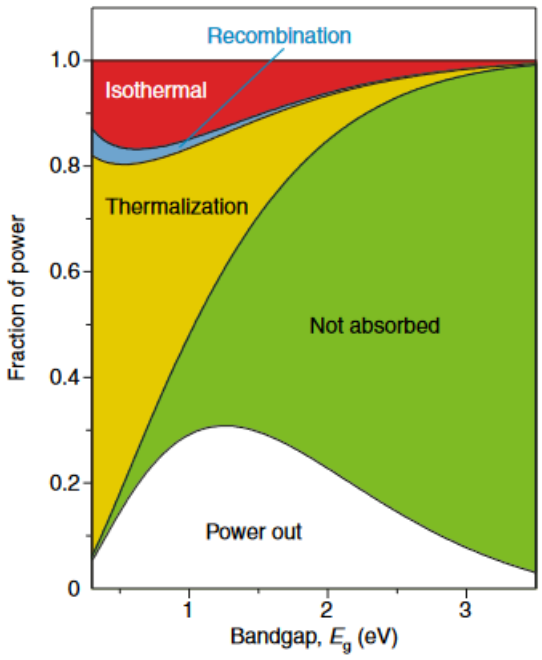

Figure 1. 1. Maximum solar power conversion efficiency as a function of absorber bandgap for a single gap solar cell, with loss mechanisms calculated via the Shockley-Queisser model [4] presuming the solar cell operates at the applied voltage providing maximum output power. [Reproduced from: *Guillemoles, Jean-Francois, et al. "Guide for the perplexed to the Shockley-Queisser limit model for solar cells," Nature Photonics 13, no. 8 (2019): 501-505.*] [5]

Maximizing the solar power conversion efficiency of a photovoltaic device may be approached systematically by minimizing losses. For a given semiconductor material, the most immediate loss mechanisms for solar cell photovoltaic behavior relate to which energies of photons cannot be absorbed (transmission losses) and across what energy gap the material will reliably separate electrons and holes by (thermalization losses) [4]. These are under standard solar cell operation strictly connected by the characteristic

bandgap of the semiconductor material, which is electronically responsible for the semiconducting behavior so crucial to modern electronic devices and optically forbids absorption of photons with less energy than the bandgap. A breakdown of the loss mechanisms as a function of the bandgap under sunlight is presented in Figure 1.1 [5], with transmission losses in green and thermalization losses in yellow. There are additional losses due to fundamental heat engine efficacy limitations (red) and recombination of carriers (blue), and in a non-ideal solar cell the efficiency will often be further limited, for example by imperfectly ohmic contacts, non-radiative recombination due to defects, and the reality that (especially in indirect semiconductors or thin films) absorption of photons does not behave as a perfect step function (no light absorbed below the bandgap, but all light absorbed above it) [5].

For any given absorber material, the result is a material-specific intrinsic (though not *fundamental*) efficiency limit for solar power conversion efficiency due to the bandgap connecting absorption of light and the photovoltaic effect. As determined by the shape of the solar spectrum, the output power of an 'ideal' single gap solar cell (white in Figure 1.1) reaches a maximum of ~33% efficiency. The long-standing and still economically dominant usage of crystalline silicon has a theoretical maximum of ~29% according to current simulations [6] and record setting practical examples feature ~26% [1]. Yet this by no means indicates that solar cells are genuinely limited to this efficiency range. The most mature technology that breaches the single gap limit is the multi-junction solar cell, utilizing multiple absorber materials to efficiently produce electricity from more of the solar spectrum. While primarily used for space applications due to high financial costs, with a record example under concentrated sunlight exceeding 45% efficiency [7].

But a multi-junction approach is not the only option, as a single gap device is only *fundamentally* limited by isothermal and recombination losses (red and blue in Figure 1.1). It is possible to create intermediate energy states in the bandgap or couple a solar cell to up or down converters that alter the wavelengths supplied by the solar spectrum, diverging from assumptions about the relationship between the bandgap and the efficiency due to altered transmission or thermalization losses [8]. However, the approach that will be examined in depth in this thesis is the 'hot carrier' methodology for mitigating thermalization losses proposed by Ross and Nozik [9].

1.2. Hot Carriers and Thermalization

The single gap model [4] presumes that high energy photons absorbed by a solar cell will not result in a difference in extracted carrier energies, as interactions with the crystal lattice are capable of swiftly thermalizing the 'hot carriers' that absorb high energy photons back to the conduction band edge. This assumption is reasonably accurate in many devices, but is not necessarily true. However briefly the hot carriers maintain their additional energy, a solar cell indeed captures that energy, and sufficiently swift carrier extraction could mitigate thermalization losses. The carrier distribution on both sides of the bandgap (conduction and valence band edges) as modified absorption of pulsed high energy photons is schematically presented in Figure 1.2 [10].

At time interval (2) in Figure 1.2, Electrons are raised across the material-specific bandgap to the conduction band by absorption of photons, leaving an equivalent distribution of holes in the valence band. On the sub-picosecond timescale, the carriers interact with each other to redistribute the energy between the new high energy carriers

and the carriers at the band edge during equilibrium conditions (time intervals (1) and (8)). This results in a 'hot carrier distribution' at time interval (4), where the Fermi-Dirac distribution has enhanced peak energy and an extended high energy tail. If a 'temperature' describing the distribution were calculated, it would diverge from the lattice temperature at this time. It is also observed that the distribution is different in the conduction and valence bands, due to differing effective mass in each band.

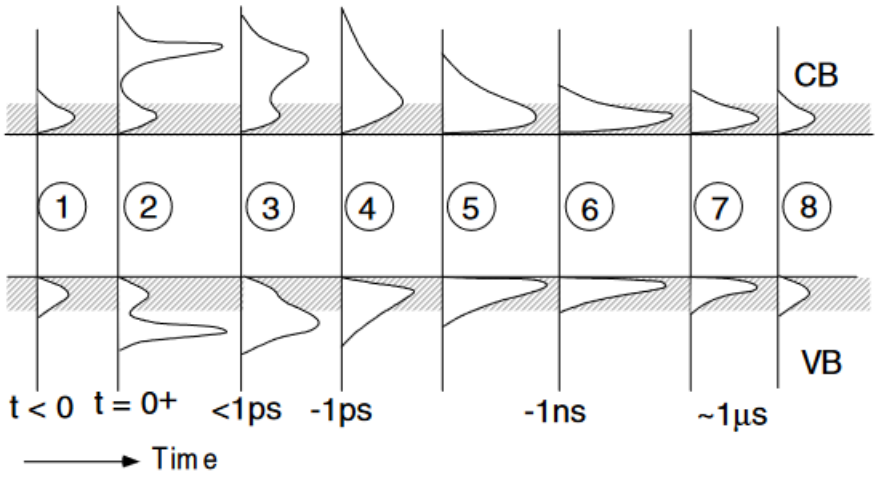

Figure 1. 2. Time lapse of carrier distributions in the conduction and valence bands from absorption of a pulse of high energy photons at t = 0 until return to equilibrium via thermalization and recombination. [Reproduced from: *Green, M. A. Third Generation Photovoltaics. 1. Aufl. ed. Vol. 12. Springer Series in Photonics. Berlin, Heidelberg: Springer-Verlag, 2006.*] [10]

Past the picosecond timescale, thermalization interactions lower the energy of the distribution to match the lattice temperature (6), and then recombination rates (comparatively slow in typical semiconductor materials) decrease the carrier population until equilibrium is regained at (8). In an electronic device, as opposed to an optical

sample, extraction becomes an alternative to recombination, if the extraction occurs with sufficient haste. In principle, if the extraction occurs on a competitive timescale with the thermalization, then a device could extract from a higher energy ('hotter') carrier distribution than if the extraction was only competitive with the recombination rate. As the hot carrier distribution has higher peak energy and an extended high energy tail, if the device features energy selective contacts fitted to the enhanced carrier distribution, then a hot carrier solar cell could feature *enhanced photovoltage*.

The goal of a hot carrier solar cell is therefore enhanced efficiency by decoupling the bandgap of the solar cell absorber material from the electrical characteristics of the solar cell. If the photovoltage is coupled to the enhanced carrier distribution rather than the bandgap, this allows for mitigation of thermalization losses and furthermore enables the use of lower bandgap absorber materials (decreasing transmission loss) while maintaining a higher photovoltage. These are substantial efficiency gains rendered viable in a hot carrier solar cell, which would permit a single junction solar cell to approach a theoretical maximum of ~66% [9].

While this is undoubtedly an exciting goal, the caveat is that not all materials are viable candidates for hot carrier absorbers. A low thermalization rate is of particular importance, and therefore understanding of the dominant mechanisms by which thermalization occurs in these semiconductor materials is a necessity. The predominant thermalization mechanism in high quality semiconductor materials, such as the III-V thin films studied in this thesis, occurs through the emission of longitudinal optical (LO) phonons by high energy carriers (the Fröhlich interaction [11]), followed by triple phonon processes whereby the LO phonon decays to acoustic phonons [12, 13]. If the

three phonon decay processes are limited in rate compared to the emission, then high energy carriers have the potential to be ‘re-heated’ by absorption of the supply of ‘hot’ LO phonons rather than continue to thermalize. This is often referred to as the ‘phonon bottleneck’ effect. As a result, while LO phonon emission is the dominant standard thermalization process, the most important step for thermalization to occur is the decay of the LO phonons. Figure 1.3 presents the key LO phonon decay processes in a zinc blende crystal structure, for visual clarity and relevance to the zinc blende structures examined in this thesis.

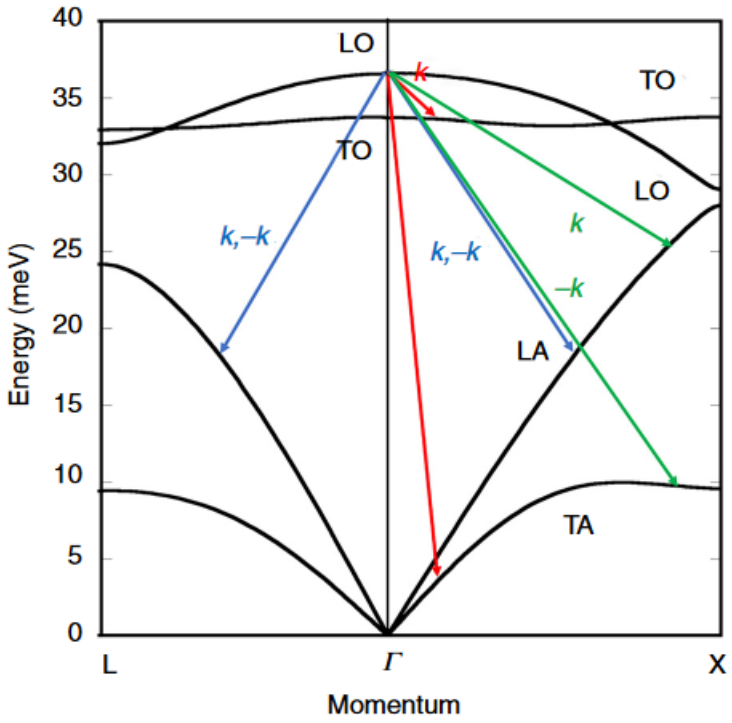

Figure 1. 3. LO phonon decay mechanisms, presented for a GaAs zinc blende crystal modeled with a valence band force field model via the NanoHub.org band structure lab tool. [Reproduced from: *Ferry, D. K. “Non-Equilibrium Longitudinal Optical Phonons and their Lifetimes.” Applied Physics Reviews 8, no. 2 (2021): 021324.*] [13]

The Klemens interaction [14] (blue in Figure 1.3) decays the LO phonon into two longitudinal acoustic (LA) phonons of equal and opposite momentum, and is the dominant decay process when available. However, energy and momentum conservation may forbid this strict transition, as while the GaAs example in Figure 1.3 has a small phononic bandgap, materials such as InN [12] are have no available phonon states to enable the Klemens decay process. The Ridley interaction [15] (red in Figure 1.3) is the next most dominant, though it notably disperses less energy to the lattice. The LO phonon decay processes are, in the correct crystal structure, possible to inhibit or block entirely. However, preventing all decay mechanisms is not viable; even were the Ridley and Klemens interactions prevented, for the case of GaAs there is also a third lesser but still significant three phonon mechanism [16] (green in Figure 1.3).

For purposes of thermalization mitigation, it suffices to work with materials that mitigate dominant processes such as Klemens or Ridley interactions, which allows the LO phonon population to become very large under high illumination intensities. Carriers will preferentially emit phonons rather than absorb phonons for any given phonon type, due to the dependence on the phonon mode's population (with ~N+1 for emission, ~N for absorption) [13]. As such, a phonon bottleneck will support a hot carrier distribution under sufficient photon flux for the scattering rate of LO phonon emission and absorption to be comparable, but as the emission is never exceeded by reabsorption of LO phonons this will only slow thermalization rather than halt it. The phonon bottleneck effect is the result of slowed LO phonon decay rendering reabsorption of LO phonons by carriers more viable *combined with* a large concurrent LO phonon population that makes emission and absorption more comparable in rate; the better the decay mitigation, the

less high energy photon flux is required, but the bottleneck effect requires a minimum input to activate. As a result, at low incident illumination intensity the phonon bottleneck deactivates [17, 18].

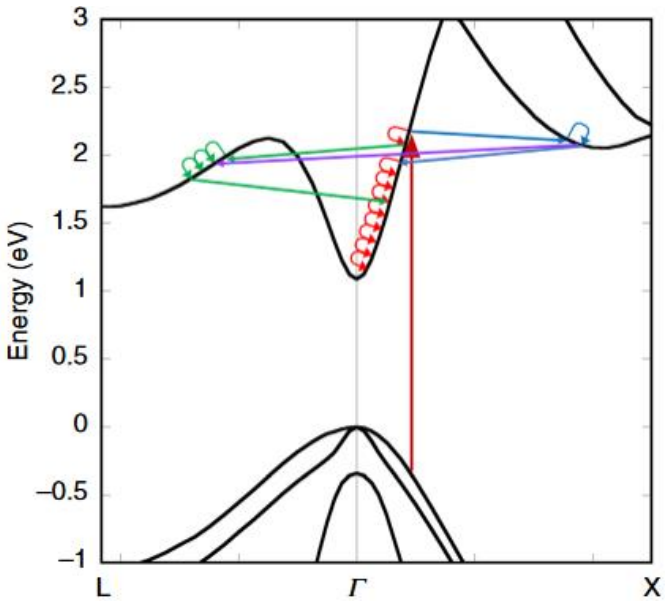

Figure 1. 4. Schematic representation of hot carrier thermalization through phonon emission. In addition to thermalization towards the conduction band minimum at the Γ valley (red), intervalley transfer of the carrier between Γ and L (green) or X (blue) or between X and L directly (purple) become viable with sufficient carrier energy and high momentum phonons. [Reproduced from: *Ferry, D. K. "Non-Equilibrium Longitudinal Optical Phonons and their Lifetimes." Applied Physics Reviews 8, no. 2 (2021): 021324.*] [13]

In addition to phonon scattering rates related to transition towards the conduction band edge at the zero momentum point of the Brouillon zone (Γ valley), certain III-V materials preferentially scatter carriers to other metastable upper valleys of the conduction band,

associated with different symmetries such as the L or X valleys. Figure 1.4 illustrates how these phonon mediated thermalization pathways function in practice; notably, even the comparatively high energy LO phonons will need multiple interactions to return a high energy ‘hot’ carrier to the conduction band minimum.

Given sufficient energy, access to the upper valleys of the conduction band becomes available via high momentum intervalley phonon interactions. As intervalley scattering processes are a means of temporarily storing carriers at higher energy, it is a viable means of thermalization mitigation [19, 20, 21], although as a means of creating hot carrier solar cells it has only recently become a focus compared to the more widely studied phonon bottleneck, in large part due to the experimental results presented in later chapters of this thesis.

1.3. Hot Carrier Temperature

By convention, the enhanced energy of a ‘hot carrier distribution’ is described with a characteristic ‘temperature’ [22]. This is a very useful analytical technique, allowing succinct comparison between different studies and analysis of a carrier distribution’s dependencies, but it is equally important to understand that the description as a ‘temperature’ is not strictly accurate. As the time lapse in Figure 1.2 illustrates, a hot carrier distribution is not an equilibrium feature. When under continuous wave rather than pulsed illumination, hot carrier behavior has been observed (typically through photoluminescence techniques) under steady state conditions, and this has historically been treated as a quasi-equilibrium for purposes of carrier temperature analysis. Nevertheless, this is a far-from-equilibrium effect that is under examination, and as such

simple detailed balance descriptions are not necessarily appropriate. Indeed, and perhaps most relevantly, one such detailed balance analysis that the hot carrier solar cell diverges from is the single gap efficiency limits discussed in Section 1.1 [4].

Hot carrier temperatures are often determined through photoluminescence measurements, where a sample is exposed to illumination, prompting the process of absorption, thermalization, and recombination. Radiative recombination across a direct (momentum consistent) bandgap between conduction and valence bands produces a detectable photoluminescence (PL) spectrum, and treating the steady state as quasi-equilibrium, this may be analyzed in a useful fashion according to the generalized Planck relation:

$$I_{PL}(E) = \frac{A(E)\,(E)^2}{4\pi^2 h^3 c^2}\left[exp\left(\frac{E-\Delta\mu}{k_B T_H}\right) - 1\right]^{-1}, \tag{1.1}$$

where I_{PL} is the PL intensity, E is the photon energy, $A(E)$ is the energy-dependent absorptivity of the absorber material, h is Planck's constant, c is the speed of light, $\Delta\mu$ is the quasi-Fermi level splitting (chemical potential difference), k_B is Boltzmann's constant, and T_H is the carrier temperature [23]. The full fitting to the photoluminescence spectrum is non-trivial, but in complex devices is a necessity for accurate temperature analysis, particularly in the case of quantum well systems subject to band filling effects at high excitation powers [24, 25, 26, 27].

In the case of structures with absorptivity that is not prone to fluctuation across the wavelengths of interest, as is often the case in high quality III-V material bulk layers such as the ones that will be examined at length in this thesis, the analysis can be

simplified to a linear fitting of the natural logarithm of the high energy tail of the photoluminescence [26, 27, 28] as follows:

$$\ln\left(I_{PL}(E)\right) = \ln\left(\varepsilon(E)\right) - \frac{E}{k_B T_H}, \tag{1.2}$$

where $\varepsilon(E)$ is the previous absorptivity dependent terms collapsed into the emissivity. The resulting slope is then inversely proportional to the desired carrier temperature of the distribution. In quantum well systems, this analysis has been observed to produce 11% uncertainty in T_H compared to the full fitting [23], however analysis of hot carrier temperatures in bulk $In_{0.53}Ga_{0.47}As$ absorber devices with this method [29] are within error of the full fitting results.

1.4. Recent Progress in the Field of Hot Carrier Solar Cells

In the past decade, the hot carrier solar cell has transitioned from the realm of theory to a subject of practical experimentation. Hirst *et al.* [30] demonstrated evidence of hot carrier-supported photocurrent in a $In_{0.16}Ga_{0.84}As$ single quantum well solar cell. Taking current density-voltage measurements of the quantum well at 10 K lattice temperature under 1.41 eV laser energy revealed that the quantum well is able to confine carriers only for a small segment of forward bias, shown in Figure 1.5 (a). This provided the opportunity to modify the temperature of the distribution by two different means, and observe when the current increased under each circumstance, shown in Figure 1.5 (b).

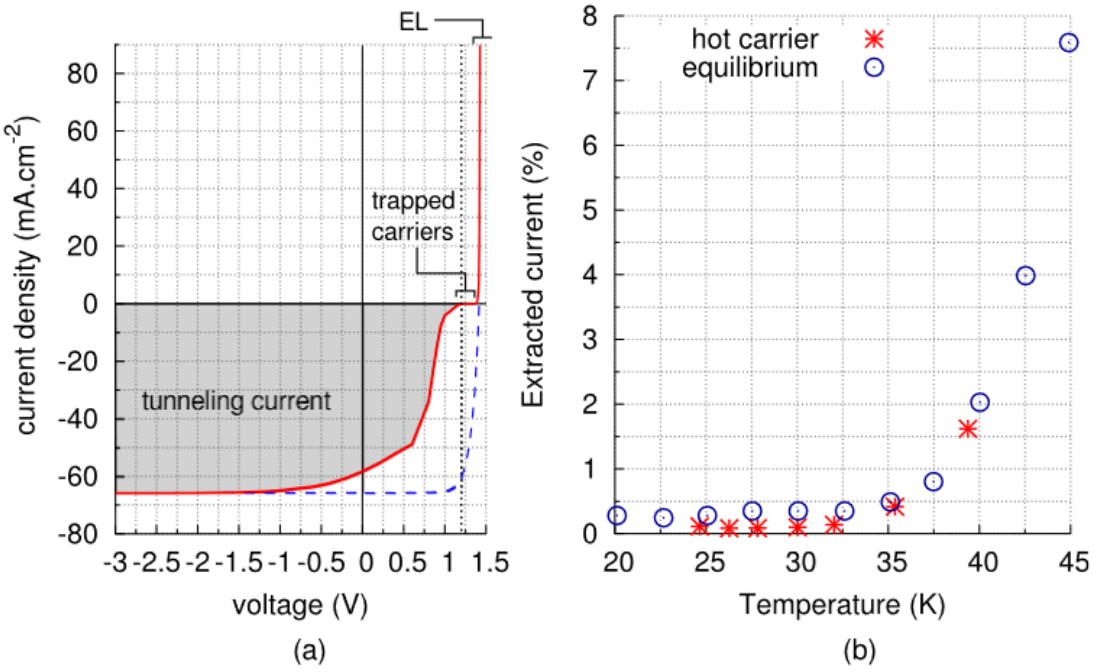

Figure 1. 5. (a) Current-voltage characteristic of the GaAs/InGaAs single quantum well under a monochromatic laser source (1.41 eV) at 10 K (red curve) and under 1 Sun AM 1.5G illumination at 295 K, but artificially matched to reverse bias current density and *Voc* for the monochromatic case (dashed blue line) to illustrate fill factor. (b) Extracted current percentage (ratio between photo-excited current at 1.2 V and reverse bias saturation current) versus carrier temperature for non-equilibrium hot carriers due to applying incident power sufficient to create the specified temperature of hot carrier distribution (red stars) and carriers in thermal equilibrium at the specified lattice temperature (blue circles). [Reproduced from: *Hirst, L. C., et al. "Experimental Demonstration of Hot-Carrier Photo-Current in an InGaAs Quantum Well Solar Cell." Applied Physics Letters 104, no. 23 (2014): 231115.*] [30]

Figure 1.5 (a) reveals the presence of an inflection in the current density-voltage characteristic, decreasing the fill factor of the solar cell photovoltaic regime compared to idealized (blue dashed) behavior scaled from high temperature measurements unrestricted by the quantum well confinement, and preventing all extraction at approximately + 1.2 V. This s-shape is evidence of a barrier to extraction [31] which is presented schematically in Figure 1.6 below. Figure 1.6 demonstrates the GaAs p-i-n structure and the carrier distribution in the InGaAs quantum well.

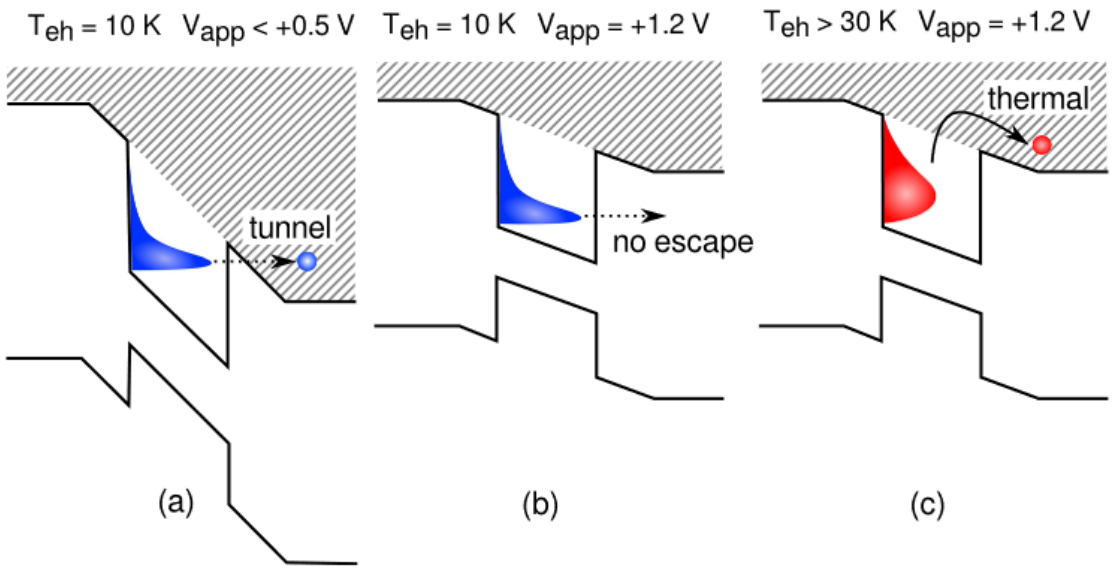

Figure 1. 6. Schematic representation of a carrier distribution in the GaAs/InGaAs single quantum well under bias and altered carrier distribution temperature to illustrate (a) tunneling conditions, (b) trapped conditions, and (c) thermionic emission conditions. [Reproduced from: *Hirst, L. C., et al. "Experimental Demonstration of Hot-Carrier Photo-Current in an InGaAs Quantum Well Solar Cell." Applied Physics Letters 104, no. 23 (2014): 231115.*] [30]

Figure 1.6 (a) demonstrates the extraction pathway prior (smaller positive or negative applied bias) to the inflection in Figure 1.5 (a), where tunneling allows carriers to escape. Figure 1.6 (b) and (c) demonstrate the confinement at 10 K carrier temperature but the escape of carriers in the high energy tail at > 30 K. These are two means of enhancing the carrier distribution to allow the high energy tail of the distribution in the quantum well to escape at + 1.2 V bias, producing a detectable current, both shown in Figure 1.5 (b). The first mechanism is simply by increasing the lattice temperature, and raising the equilibrium temperature of the carrier distribution along with it (blue circles). The alternative approach is producing by increasing the laser power to induce a hot carrier distribution via the bottleneck effect, determining the temperature of the carrier distribution via power dependent photoluminescence measurements at 10 K lattice temperature, and plotting the current against the calculated carrier temperature as the red stars in Figure 1.5 (b). The clear outcome is that in both cases the temperature of the carrier distribution rose above 30 K lattice temperature before current extraction began, *solid evidence* of hot carrier behavior driven photocurrent.

The work of Nguyen *et al.* [32] in contrast demonstrated evidence of photovoltage enhancement due to hot carrier behavior in a InP/InGaAsP single quantum well at room temperature. While the device's absorption was very limited, it nevertheless featured a bottleneck type power dependence: enhanced carrier temperature with excitation power but deactivated hot carrier temperatures at low laser fluence, as shown in Figure 1.7.

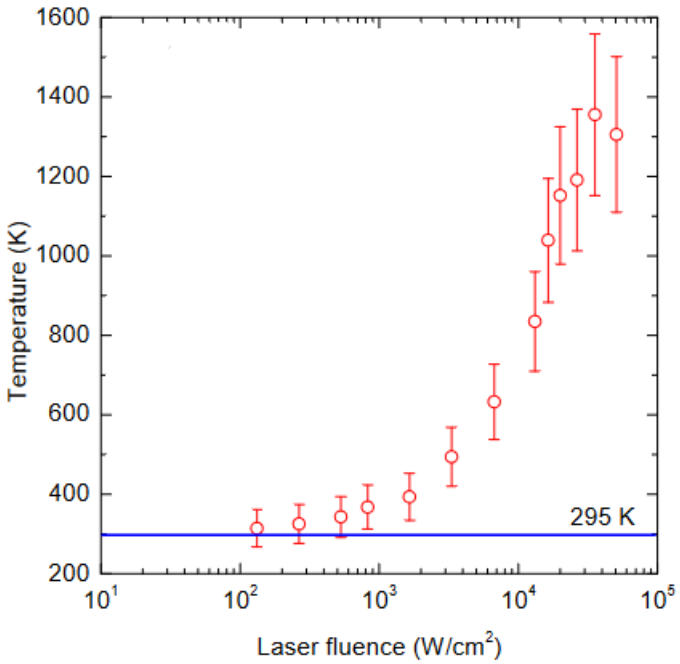

Figure 1. 7. Power dependence of the carrier temperature of the InP/InGaAsP single quantum well at room temperature with a 980 nm wavelength laser. [Reproduced from: *Nguyen, D., et al. "Quantitative Experimental Assessment of Hot Carrier-Enhanced Solar Cells at Room Temperature," Nature Energy 3, (2018): 236–242.*] [32]

But it is in Figure 1.8 that we can see the electronic consequences. The lowest energy quantum well transition is indicated by the green line in Figure 1.8, serving as the modified bandgap due to the quantum well confinement. The open circuit voltage (V_{oc}) exceeds this value at high laser fluence (black dots and lines), indicating the device is likely operating outside thermodynamic equilibrium. The major alternative for quantum well cases (that this is the result of band filling) does not adequately explain the results of fitting the photoluminescence with the electrochemical potential in the barriers (red circles) and well (blue triangles). If the chemical potential in the quantum well rose above

the green line, that would have been indicative of the high laser fluence pushing the quasi-Fermi level above the former ground state, but this emphatically does not occur, with the chemical potential associated with the barriers instead increasing. This is attributed to a Seebeck type behavior [33], with the temperature gradient between the well temperature (as shown in Figure 1.7) and the barrier temperature (in equilibrium with the lattice) driving a transfer of carriers from the well to the enhanced electrochemical potential and V_{oc}.

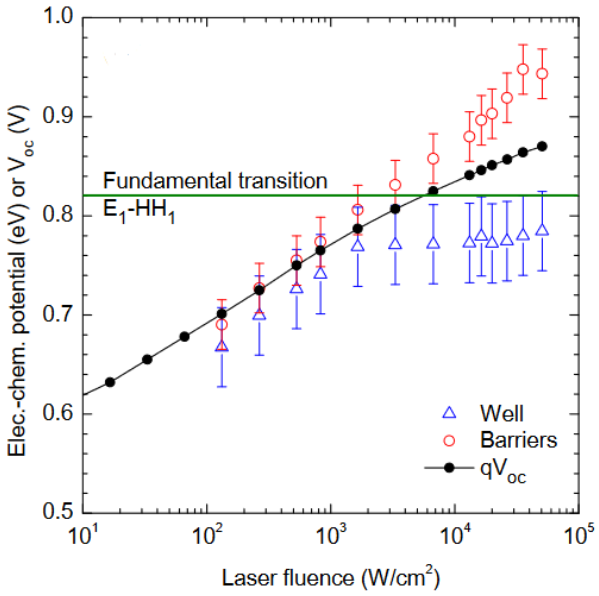

Figure 1. 8. Power dependence of the electrochemical potential of the well (blue triangles) and barriers (red circles), as well as the Voc (black lines and dots) of the InP/InGaAsP single quantum well at room temperature with a 980 nm wavelength laser. [Reproduced from: *Nguyen, D., et al. "Quantitative Experimental Assessment of Hot Carrier-Enhanced Solar Cells at Room Temperature," Nature Energy 3, (2018): 236–242.*] [32]

But of perhaps most relevance among preceding literature to this thesis is the work of Esmaielpour *et al.* [34] with a Type II InAs/AlAsSb multi-quantum well optical sample. Through photoluminescence using 442 nm wavelength laser illumination, analysis of the hot carrier temperature presented in Figure 1.9 demonstrates unanticipated temperature and power dependence.

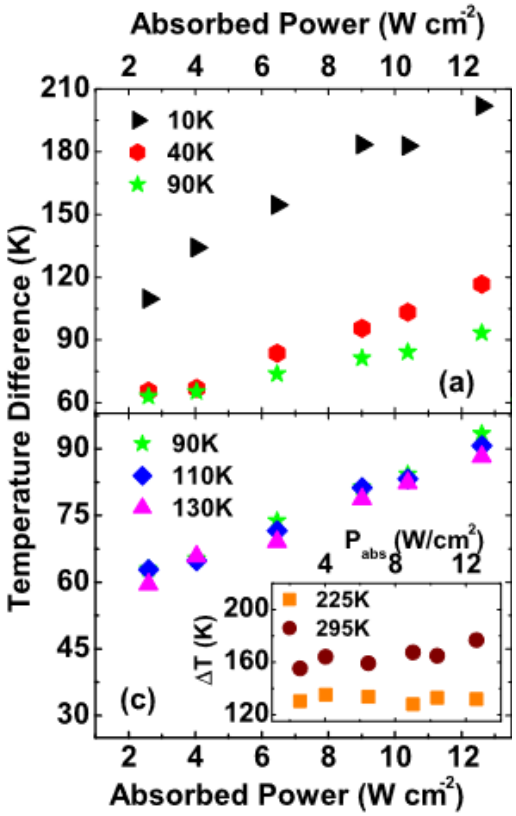

Figure 1. 9. Power dependence of the carrier temperature of the Type II AlAsSb/InAs multi-quantum well sample at multiple temperatures under a 442 nm wavelength laser. [Reproduced from: *Esmaielpour, H., et al. "Suppression of Phonon-Mediated Hot Carrier Relaxation in Type-II InAs/AlAs$_x$Sb$_{1-x}$ Quantum Wells: A Practical Route to Hot Carrier Solar Cells." Progress in Photovoltaics: Research and Applications 24, no. 5 (2016): 591-99.*] [24]

The power dependence shown in Figure 1.9 is comparable to that demonstrated in Figure 1.7 in its general trend, yet examination of the x-axis scale reveals that despite the data taken in Figure 1.9 being measured at comparatively very low absorbed powers, the temperature difference from the lattice is unexpectedly strong. A literature review of power dependent PL analysis of hot carrier temperatures [17, 18, 32] reveals this is contrary to the behavior in most samples, but was also not unheard of – similar hot carrier behavior at low illumination powers was observed in silicon quantum dots [34]. This is attributed to the indirect bandgap of silicon interfering with thermalization transitions in a dimensionally confined system. A large body of experimental work has shown that phonon interactions can be mitigated by simply decreasing the dimensions to a quantum well or quantum dot, owing to the nature of phonons as quanta of lattice vibrations, a smaller lattice is simply more limited in that regard, and this has been shown to be of benefit for inhibited thermalization in low dimensional systems [35].

One plausible explanation for additional thermalization mitigation in the InAs multi-quantum well sample stems from the Type II nature of the quantum well/barrier pair with AlAsSb, which appears to be temperature dependent. Due to alloy fluctuations in this system [36], at low temperatures and power densities there are interface states that force the device to operate in a Type I like quantum well regime (hole and electron wavefunctions overlapping in the InAs region) rather than the desired fundamental Type II state of the system, which limits recombination of carriers (hole wavefunctions in the barriers, electron wavefunctions contained in the wells). State filling passivates the localization at ~100 K, enabling longer carrier lifetimes due to the shift to Type II behavior [37].

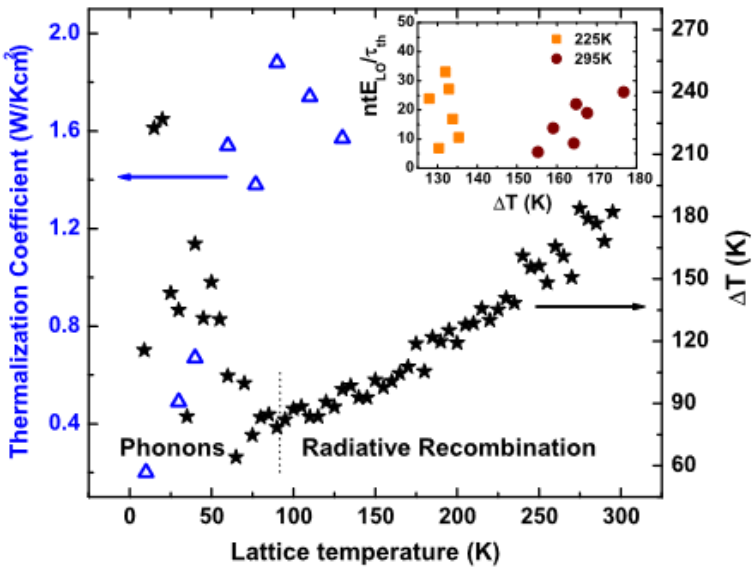

Figure 1. 10. Temperature dependence of the difference from lattice temperature of the carrier temperature (right y-axis, black stars) and the thermalization coefficient (left y-axis, blue triangles) of the Type II AlAsSb/InAs multi-quantum well sample under a 442 nm wavelength laser. Above 130 K lattice temperature, the analysis of the thermalization coefficient (Q) breaks down, shown in the inset where Q should be the slope of the best fit line of the scatter plot for each temperature. [Reproduced from: *Esmaielpour, H., et al. "Suppression of Phonon-Mediated Hot Carrier Relaxation in Type-II InAs/AlAsxSb1−x Quantum Wells: A Practical Route to Hot Carrier Solar Cells." Progress in Photovoltaics: Research and Applications 24, no. 5 (2016): 591-99.*] [24]

The continued shift to weaker power dependence at higher temperatures in Figure 1.9 is difficult to fully explain with the shift to Type II behavior however. Another piece of the puzzle is presented in Figure 1.10, while compares temperature dependence at fixed

illumination power for both the carrier temperature and a thermalization coefficient *Q*, defined as:

$$P_{th} = \frac{n\,t\,E_{LO}}{\tau_{th}} exp\left(-\frac{E_{LO}}{k_B T_e}\right) = Q\Delta T exp\left(-\frac{E_{LO}}{k_B T_e}\right), \quad (1.3)$$

Where P_{th} is the thermalized power (absorbed power at V_{oc}), n is carrier density, t is thickness, E_{LO} is the LO phonon energy (~29 meV for InAs), τ_{th} is the thermalization time, k_B is Boltzmann's constant, T_e is the carrier temperature, ΔT is the difference between carrier and lattice temperatures, and Q is the thermalization coefficient [24]. When the LO phonon scattering rates dominate the thermalization, Q is a helpful metric that represents the dominance or strong of electron-phonon relaxation pathways, with a smaller Q inferring less Fröhlich coupling which is better for hot carrier behavior [17]. However, a Q of zero or even negative is unphysical – and as the inset of Figure 1.10 demonstrates, for this sample using the slope of ntE_{LO}/τ_{th} vs ΔT at the higher temperatures to determine Q is ineffective.

The LO phonon scattering rate becomes less dominant at high temperatures, as the power dependence becomes weaker. This result is difficult to explain in terms of a phonon bottleneck, but it nevertheless clearly results in hot carrier behavior, and through a more robust mechanism with respect to low illumination power. In this thesis, this behavior will be explained more effectively through intervalley mechanisms that exceed the dominance of the LO phonon scattering rate, both in a set of InAs/AlAsSb multi-quantum well devices and in subsequent bulk InGaAs absorber heterostructures, where the benefits of this approach are explored at length.

Outline of the Thesis

This dissertation is an in-depth study of the application of intervalley mechanisms to the field of hot carrier solar cells, experimentally demonstrating robust hot carrier behavior under practical operating conditions in a series of InGaAs based heterostructure devices. Analysis with different laser wavelengths provides evidence of two mechanisms that support the intervalley behavior: intervalley phonon scattering and electric field-induced scattering to upper valleys of the conduction band. The mechanisms are investigated in detail, intent to discern a means to efficiently extract the hot carriers from the upper valleys and provide a path to a fully operational hot carrier solar cell.

Chapter 1 introduces the concept of the hot carrier solar cell, the motivation for the following studies, and summarizes the prior work that serves as the foundation upon which this thesis stands. Chapter 2 explains the experimental techniques employed throughout the later chapters for optical and electronic characterization. Chapter 3 examines a study of InAs/AlAsSb multi-quantum well devices with differing barrier thicknesses, theorized to feature intervalley transfer that supports hot carrier behavior.

Chapter 4 presents experimental demonstration of practical hot carrier behavior in a proof-of-concept bulk InGaAs absorber heterostructure device that operates on intervalley scattering-based ‘valley photovoltaic’ principles. Chapter 5 is an analysis of the barriers to carrier extraction from an upper valley, via a series of InGaAs heterostructures with altered top (n^+) barrier layers. Finally, Chapter 6 presents a more focused analysis of the role of the electric field inside these structures through modification of the InGaAs absorber thickness without variation of the doping profile. In addition, the potential for a phonon bottleneck type effect to occur *concurrently* with

intervalley scattering based hot carrier maintenance is demonstrated, resulting in robust hot carrier behavior that is enhanced with increasing illumination power density.

References

[1] Green, Martin A., Ewan D. Dunlop, Jochen Hohl-Ebinger, Masahiro Yoshita, Nikos Kopidakis, Karsten Bothe, David Hinken, Michael Rauer, Xiaojing Hao. “Solar Cell Efficiency Tables (Version 60).” *Progress in Photovoltaics: Research and Applications* 30, no. 7 (2022): 687-701.

[2] Philipps, Simon and Werner Warmuth. “Fraunhofer I.S.E. Photovoltaics Report.” Fraunhofer ISE. Published 22 September 2022. Accessed 29 October 2022. https://www.ise.fraunhofer.de/content/dam/ise/de/documents/publications/studies/Photovoltaics-Report.pdf,.

[3] Mehedi, Tanveer Hassan, Eskinder Gemechu, and Amit Kumar. "Life Cycle Greenhouse Gas Emissions and Energy Footprints of Utility-scale Solar Energy Systems." *Applied Energy* 314 (2022): 118918.

[4] Shockley, William, and Hans J. Queisser. "Detailed Balance Limit of Efficiency of p-n Junction Solar Cells." *Journal of Applied Physics* 32, no. 3 (1961): 510-19.

[5] Guillemoles, Jean-Francois, Thomas Kirchartz, David Cahen, and Uwe Rau. "Guide for the Perplexed to the Shockley–Queisser Model for Solar Cells." *Nature Photonics* 13, no. 8 (2019): 501-05.

[6] Andreani, Lucio Claudio, Angelo Bozzola, Piotr Kowalczewski, Marco Liscidini, and Lisa Redorici. "Silicon Solar Cells: Toward the Efficiency Limits." *Advances in Physics: X* 4, no. 1 (2019): 1548305.

[7] Geisz, John F., Myles A. Steiner, Nikhil Jain, Kevin L. Schulte, Ryan M. France, William E. McMahon, Emmett E. Perl, and Daniel J. Friedman. "Building a Six-

Junction Inverted Metamorphic Concentrator Solar Cell." *IEEE Journal of Photovoltaics* 8, no. 2 (2018): 626-32.

[8] Strandberg, Rune. "Analytic JV -Characteristics of Ideal Intermediate Band Solar Cells and Solar Cells With Up and Downconverters." *IEEE Transactions on Electron Devices* 64, no. 5 (2017): 2275-282.

[9] Ross, Robert T., and Arthur J. Nozik. "Efficiency of Hot-carrier Solar Energy Converters." *Journal of Applied Physics* 53, no. 5 (1982): 3813-818.

[10] Green, M. A. *Third Generation Photovoltaics*. 1. Aufl. ed. Vol. 12. Springer Series in Photonics. Berlin, Heidelberg: Springer-Verlag, 2006.

[11] Fröhlich, H., H. Pelzer, and S. Zienau. "Properties of Slow Electrons in Polar Materials." *Philosophical Magazine (London, England: 1945)* 41, no. 314 (1950): 221-242.

[12] Conibeer, G., N. Ekins-Daukes, J-F. Guillemoles, D. König, E. C. Chou, C-W. Jiang, S. Shrestha and M. A. Green. “Progress on hot carrier solar cells.” *Solar Energy Materials & Solar Cells* 93, (2009): 713-719.

[13] Ferry, D. K. “Non-Equilibrium Longitudinal Optical Phonons and their Lifetimes.” *Applied Physics Reviews* 8, no. 2 (2021): 021324.

[14] Klemens, P. G. "Anharmonic Decay of Optical Phonons." *Physical Review* 148, no. 2 (1966): 845-48.

[15] Ridley, B. K, and R. Gupta. "Nonelectronic Scattering of Longitudinal-optical Phonons in Bulk Polar Semiconductors." *Physical Review B: Condensed Matter* 43, no. 6 (1991): 4939-944.

[16] Vallee, F., and F. Bogani. "Coherent Time-resolved Investigation of LO-phonon Dynamics in GaAs." *Physical Review B: Condensed Matter* 43, no. 14 (1991): 12049-2052.

[17] Hirst, Louise C., Hiromasa Fujii, Yunpeng Wang, Masakazu Sugiyama, and Nicholas J. Ekins-Daukes. "Hot Carriers in Quantum Wells for Photovoltaic Efficiency Enhancement." *IEEE Journal of Photovoltaics* 4, no. 1 (2014): 244-52.

[18] Le Bris, A., L. Lombez, S. Laribi, G. Boissier, P. Christol, and J.-F. Guillemoles. "Thermalisation Rate Study of GaSb-based Heterostructures by Continuous Wave Photoluminescence and Their Potential as Hot Carrier Solar Cell Absorbers." *Energy & Environmental Science* 5, no. 3 (2012): 6225-232.

[19] Ferry, D. K. "In Search of a True Hot Carrier Solar Cell." *Semiconductor Science and Technology* 34, no. 4 (2019): 44001.

[20] Zhang, Yi, Xuguang Jia, Shuang Liu, Kefan Wu, Jiayu Zhang, and Gavin Conibeer. "Explore the Correlation between Intervalley Scattering and Phonon Bottleneck Effect on the Hot Carrier Relaxation in Bulk GaSb and InN for Hot Carrier Solar Cells." *Journal of Applied Physics* 130, no. 20 (2021): 205705.

[21] Ferry, D. K., S. M. Goodnick, V. R. Whiteside, and I. R. Sellers. "Challenges, Myths, and Opportunities in Hot Carrier Solar Cells." *Journal of Applied Physics* 128, no. 22 (2020): 220903.

[22] Wurfel, Peter. "The chemical potential of radiation." *Journal of Physics C: Solid State Physics* 15, no. 18 (1982): 3967.

[23] Gibelli, François, Laurent Lombez, and Jean-François Guillemoles. "Accurate radiation temperature and chemical potential from quantitative photoluminescence analysis of hot carrier populations." *Journal of Physics: Condensed Matter* 29, no. 6 (2016): 06LT02.

[24] Esmaielpour, H., V. R. Whiteside, J. Tang, S. Vijeyaragunathan, T. D. Mishima, S. Cairns, M. B. Santos, B. Wang, and I. R. Sellers. "Suppression of Phonon-Mediated Hot Carrier Relaxation in Type-II InAs/$AlAs_xSb_{1-x}$ Quantum Wells: A Practical Route to Hot Carrier Solar Cells." *Progress in Photovoltaics: Research and Applications* 24, no. 5 (2016): 591-99.

[25] Esmaielpour, Hamidreza, Vincent R. Whiteside, Louise C. Hirst, Joseph G. Tischler, Chase T. Ellis, Matthew P. Lumb, David V. Forbes, Robert J. Walters, and Ian R. Sellers. "Effect of Occupation of the Excited States and Phonon Broadening on the Determination of the Hot Carrier Temperature from Continuous Wave Photoluminescence in InGaAsP Quantum Well Absorbers." *Progress in Photovoltaics: Research and Applications* 25, no. 9 (2017): 782-90.

[26] Whiteside, V. R., B. A. Magill, Matthew P. Lumb, H. Esmaielpour, M. A. Meeker, R. R. H. H. Mudiyanselage, A. Messager, S. Vijeyaragunathan, T. D. Mishima, M. B. Santos, I. Vurgaftman, G. A. Khodaparast, and I. R. Sellers. "Valence Band States in an InAs/AlAsSb Multi-quantum Well Hot Carrier Absorber." *Semiconductor Science and Technology* 34, no. 2 (2019): 25005.

[27] Lim, Jia Wei Melvin, Yue Wang, Jianhui Fu, Qiannan Zhang, and Tze Chien Sum. "Spotlight on Hot Carriers in Halide Perovskite Luminescence." *ACS Energy Letters* 7, no. 2 (2022): 749-56.

[28] Esmaielpour, H., L. Lombez, M. Giteau, J.-F. Guillemoles, and D. Suchet. “Impact of Excitation Energy on Hot Carrier Properties in InGaAs Multi-Quantum Well Structure,” *Progress in Photovoltaics: Research and Applications* 30, no. 11 (2022): 1354-362.

[29] Esmaielpour, Hamidreza, Kyle R. Dorman, David K. Ferry, Tetsuya D. Mishima, Michael B. Santos, Vincent R. Whiteside, and Ian R. Sellers. "Exploiting Intervalley Scattering to Harness Hot Carriers in III–V Solar Cells." *Nature Energy* 5, no. 4 (2020): 336-43.

[30] Hirst, L. C., R. J. Walters, M. F. Führer, and N. J. Ekins-Daukes. "Experimental Demonstration of Hot-Carrier Photo-Current in an InGaAs Quantum Well Solar Cell." *Applied Physics Letters* 104, no. 23 (2014): 231115.

[31] Saive, Rebecca. "S-Shaped Current-Voltage Characteristics in Solar Cells: A Review." *IEEE Journal of Photovoltaics* 9, no. 6 (2019): 1477-484.

[32] Nguyen, D.-T., L. Lombez, F. Gibelli, S. Boyer-Richard, A. Le Corre, O. Durant, and J-F. Guillemoles. “Quantitative Experimental Assessment of Hot Carrier-Enhanced Solar Cells at Room Temperature,” *Nature Energy* 3, (2018): 236–242.

[33] Rodière, Jean, Laurent Lombez, Alain Le Corre, Olivier Durand, and Jean-François Guillemoles. "Experimental Evidence of Hot Carriers Solar Cell Operation in Multi-Quantum Wells Heterostructures." *Applied Physics Letters* 106, no. 18 (2015): 183901.

[34] Zhang, Pengfei, Yu Feng, Xiaoming Wen, Wenkai Cao, Rebecca Anthony, Uwe Kortshagen, Gavin Conibeer, and Shujuan Huang. "Generation of Hot Carrier

Population in Colloidal Silicon Quantum Dots for High-efficiency Photovoltaics." *Solar Energy Materials and Solar Cells* 145, no. Part 3 (2016): 391-96.

[35] Rosenwaks, Y., M. C. Hanna, D. H. Levi, D. M. Szmyd, R. K. Ahrenkiel, and A. J. Nozik. "Hot-carrier Cooling in GaAs: Quantum Wells versus Bulk." *Physical Review. B, Condensed Matter* 48, no. 19 (1993): 14675-4678.

[36] Hirst, Louise C., Matthew P. Lumb, Josh Abell, Chase T. Ellis, Joseph G. Tischler, Igor Vurgaftman, Jerry R. Meyer, Robert J. Walters, and María González. "Spatially Indirect Radiative Recombination in InAlAsSb Grown Lattice-matched to InP by Molecular Beam Epitaxy." *Journal of Applied Physics* 117, no. 21 (2015): 215704.

[37] Tang, J., V. R. Whiteside, H. Esmaielpour, S. Vijeyaragunathan, T. D. Mishima, M. B. Santos, and I. R. Sellers. "Effects of Localization on Hot Carriers in InAs/$AlAs_xSb_{1-x}$ Quantum Wells." *Applied Physics Letters* 106, no. 6 (2015): 061902.

Chapter **2**

Experimental Methods

2.1. Current Density-Voltage

To determine how effective a diode operates, application of a bias voltage and measurement of current passing through the contacts is a standard and highly informative measurement. For solar cell applications in particular, measurement of the current *density* (a 2-D density defined by the surface area of the device exposed to illumination) as a function of external bias when illuminated is of particular importance. Knowledge of the carrier extraction with respect to the size of the device permits useful estimation of how much output power a small laboratory device could provide if expanded to a module scale, and perhaps more importantly current densities may be compared directly between devices of very different specifications. For a photovoltaic solar cell, the current density-voltage (*J*-*V*) response can be described (using the Shockley-Queisser [1] assumptions used to define the single gap solar cell efficiency limit) as:

$$J = J_0 exp\left(\frac{qV}{nk_BT_{cell}} - 1\right) - J_{SC} \tag{2.1}$$

Where J is the total current density, J_{SC} is the short circuit current density introduced by the photovoltaic effect (absorption of photons and subsequent extraction of carriers), J_0 is the dark saturation current density (related to the recombination), q is the elementary carrier charge, V is the bias voltage, k_B is the Boltzmann constant, n is an ideality factor

dependent on which recombination processes are dominant in the device, and T_{cell} is the operating temperature of the solar cell.

In addition to short circuit current density (J_{SC}) at zero bias, it is useful to define open circuit voltage (V_{OC}) in forward bias where the current density (J) becomes zero, solving for which in Equation 2.1 provides:

$$V_{OC} = \frac{nk_BT_{cell}}{q} ln\left(\frac{J_{SC}}{J_0} + 1\right) \tag{2.2}$$

A real solar cell diverges from these values. The limitations involved can be traced through the impact on the key parameters for describing the photovoltaic (PV) response. J_{SC} and V_{OC} describe the maximum limits of the PV regime, which when the J-V curve is plotted with the sign convention of Equation 2.1 corresponds to the fourth (bottom-right) quadrant of a current density-voltage figure. A solar cell will in practice operate at whatever forward bias provides the maximum output power, the corresponding J_{max} and V_{max} being limited by J_{SC} and V_{OC} but not described by them. This is usefully described through the Fill Factor (FF):

$$FF = \frac{J_{max}V_{max}}{J_{SC}V_{OC}} \tag{2.3}$$

As realistic impediments to photovoltaic behavior are accounted for, shown in Figure 1.1 (with reversed sign convention for current density to provide better visual clarity), the output power of the device decreases. First, the bandgap of the absorber results in transmission losses (green) for low energy photons and thermalization losses (yellow) for high energy photons; as discussed in Chapter 1, a hot carrier solar cell attempts to mitigate thermalization loss, and hence a fully functional hot carrier solar cell *would feature enhanced photovoltage*.

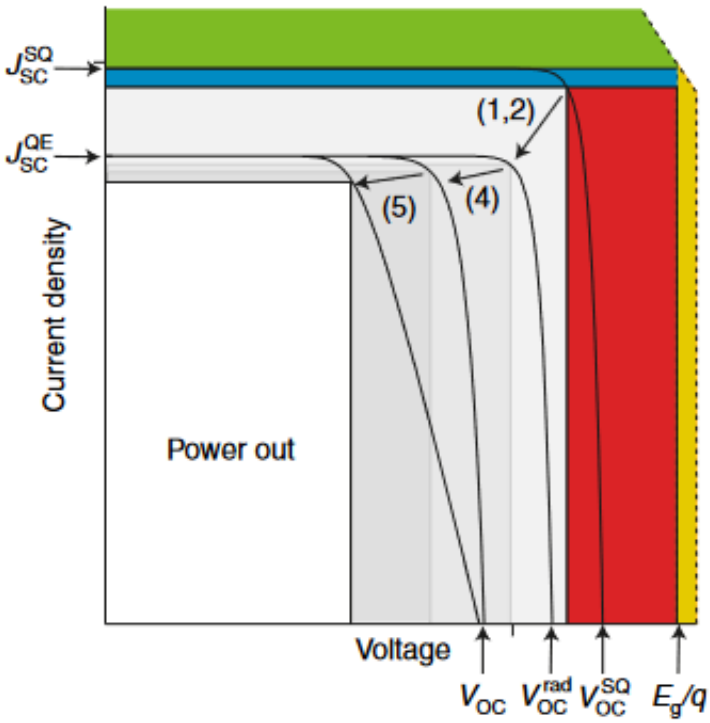

Figure 2. 1. Progressive introduction of realistic losses to the Shockley-Queisser (SQ) model [1] estimation of solar cell limitations through current density-voltage measurement values. The shaded regions represent bandgap (*Eg*) dependent losses shown in Figure 1.1, green for transmission, yellow for thermalization, blue for recombination, and red for isothermal losses. The arrows indicate violation of SQ assumptions: (1,2) step function absorption and perfect quantum efficiency (QE), (4) only radiative recombination, and (5) perfect contacts. The assumption (3) that the solar cell will not heat up during operation and modify device behavior is not included, as temperature dependence can be highly device specific. [Reproduced from: *Guillemoles, J.-F. et al. "Guide for the Perplexed to the Shockley–Queisser Model for Solar Cells." Nature Photonics 13, no. 8 (2019): 501-05*.] [2]

Careful calculation [2] of isothermal (red) and recombination losses (blue) will cause the real values of *Voc* and *Jsc* to decrease below the values predicted by Shockley and Queisser with step function absorption and generation of two carriers per photon that are both extracted [1], shown as transition (1, 2) in Figure 1.2. Inclusion of non-radiative recombination results in enhancement of J_0 to the detriment of V_{OC} in particular as shown in Equation 2.2 (transition (4)), while inclusion of non-negligible resistivity of materials and imperfectly ohmic contacts permits a notable decrease of *FF* (transition (5)). The final result is more limited output power and hence more limited solar power conversion efficiency η:

$$\eta = \frac{P_{max}}{P_{Sun}} \tag{2.4}$$

Where P_{max} is the power density $J_{max}V_{max}$ obtained at the maximum power point and P_{Sun} is the power density provided by the solar spectrum.

A set of standard illumination spectra are specified by the scientific community for simulated solar illumination. A 5800 K black-body can serve as a functional first order approximation, however as the development of photovoltaic technology has advanced, more accurate representations have become the global standard, produced by ASTM International, formerly the American Society for Testing and Materials. These are referred to as AM0 [3], AM1.5D, and AM1.5G [4], shown in Figure 2.1 for comparison. AM0 is used for space applications, hence zero 'Air Mass' modifying the solar spectrum.

For terrestrial applications, the AM1.5 spectrum accounts for average atmospheric conditions and ground reflectivity to provide realistic estimates of sunlight a practical solar cell would experience, as determined from measurements across the 48 contiguous

states of the United States of America. Air Mass 1.5 is the result of accounting for the average 41.81° the sun rises above the horizon (averaged across one year) at those latitudes, resulting in a longer path through the atmosphere than the perpendicular (AM1) path would provide. While this spectrum remains a compromise, especially when used by laboratories dispersed across the globe, it serves as an improvement over each laboratory employing a unique spectrum or all laboratories employing an unrealistic 5800 K black-body without modification

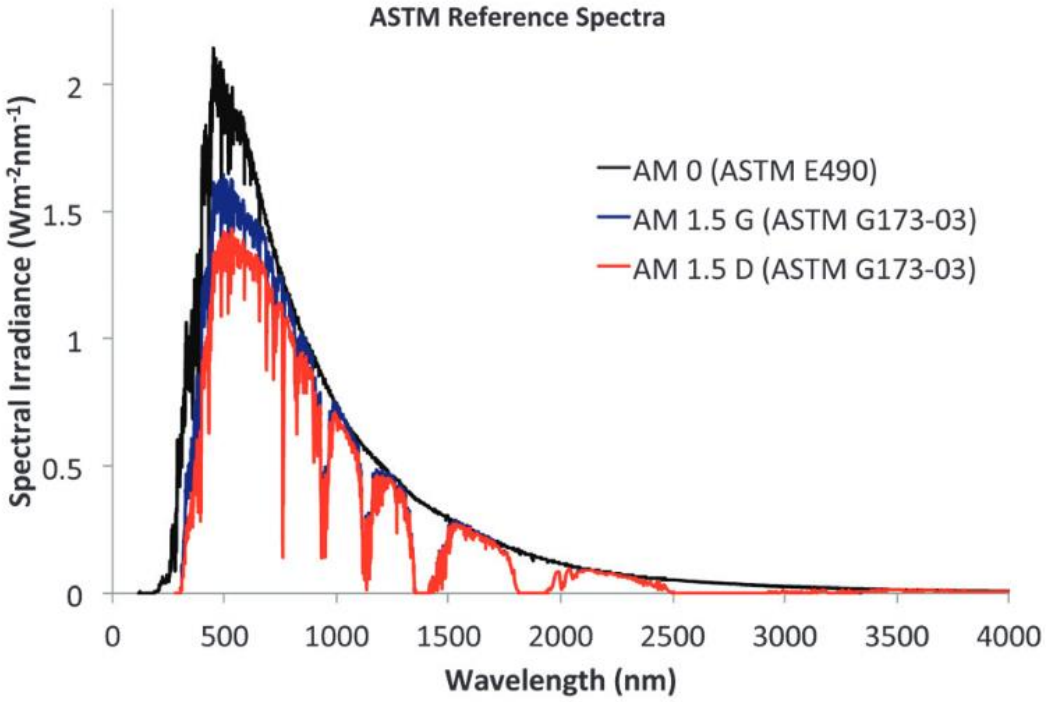

Figure 2. 2. Power dependence of the electrochemical potential of the well (blue triangles) and barriers (red circles), as well as the *Voc* (black lines and dots) of the InP/InGaAsP single quantum well at room temperature with a 980 nm wavelength laser. [Reproduced from: *Mazzio, Katherine A., and Christine K. Luscombe. "The Future of Organic Photovoltaics." Chemical Society Reviews 44, no. 1 (2014): 78-90.*] [5]

The AM1.5D spectrum is specifically employed for solar concentrators, and the decrease in intensity shown in Figure 2.1 results from only including illumination incident from within 2.5° of the sun. The AM1.5G spectrum is a more global standard for flat plane solar, and is utilized throughout this thesis for 1 Sun measurements, defined as using an AM1.5G filter over the illumination produced by a 5800 K blackbody, calibrated to the 1 Sun total integrated intensity standard of ~1000 W/m^2.

In this thesis, a Newport Oriel Sol2A™ 94022A Solar Simulator is used to provide 1 Sun solar irradiance for current density-voltage measurements. *J-V* measurements are performed with Keithley 2400 multimeters to apply the external bias and measure the current response. Temperature control for a range of 77 K to room temperature 1 Sun measurements was provided via liquid nitrogen cooling by a Linkam THMS600E cryostat connected to Linkam LNP95 temperature control system.

2.3. External Quantum Efficiency

The external quantum efficiency (EQE) combines the wavelength-dependent absorption, the number of generated carriers, and the number of extracted carriers into a quantitative assessment of the wavelength-dependent capability of a device to engage the photovoltaic effect. A simple detailed balance assumption [1] would conclude that a perfect photovoltaic device would generate a pair of carriers and extract them for each photon with energy in excess of the bandgap, and all photons with lower than bandgap energy will not be absorbed. In practice, absorption is not a step function, extraction is not guaranteed, and the EQE is a helpful characterization technique that sheds light on a solar cell's electronic properties and parasitic losses within the device structure. And

where transfer matrix calculations [6] provide a theoretical means of assessing a device's absorption, in devices with well understood extraction, EQE is a means of experimentally determining details of the device's absorptivity. EQE is calculated as:

$$EQE\ (\lambda) = \frac{\#\ of\ Extracted\ Electrons}{\#\ of\ Incident\ Photons} = \frac{I/q}{P_{in}/hv}. \tag{2.5}$$

Where I is current, q is elementary charge, P_{in} is the total incident illumination power at the specified wavelength λ, and $hv = hc/\lambda$ is the photon energy.

This measurement requires exposure to a range of monochromatic wavelengths, with care taken to ensure the measured photocurrent and monochromatic light pulses are linked via careful calibration. A schematic representation of the experimental setup is provided in Figure 2.3.

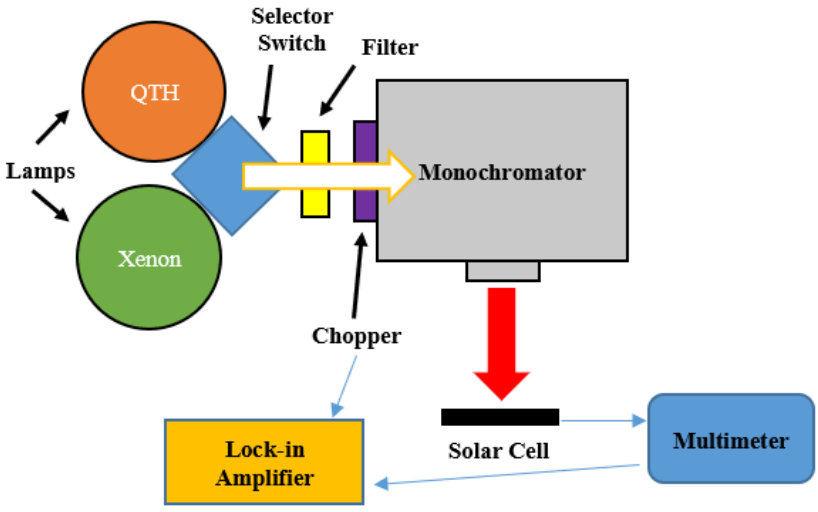

Figure 2. 3. Schematic representation of experimental setup for EQE measurements. The large white arrow is broad spectrum light. The large red arrow is monochromatic light selected by the grating inside the monochromator. Small blue arrows represent key electrical connections.

In this thesis, EQE measurements were accomplished using an Oriel Cornerstone 260 monochromator and a Stanford Research Systems Model SR830 lock-in amplifier. Two lamps were available for providing broad spectrum illumination to the monochromator: a Xenon lamp and a quartz tungsten halogen (QTH) lamp. Calibration was performed with silicon (for 300 to 1100 nm) and germanium (700 to 1800 nm) detectors of known responsivity to generate accurate references for determining incident photon counts. Current levels were recorded with a Keithley 2400 source-measurement multimeter.

Once EQE is determined, it is possible to convolute the data with an illumination source to calculate the total photocurrent. This is of particular use with the AM1.5G solar spectrum, it is possible to calculate a 1 Sun J_{SC} in this manner.

$$J_{SC} = q \int \Phi(\lambda)\, EQE(\lambda)\, d\lambda, \tag{2.6}$$

Where $\Phi(\lambda)$ is incident photon flux for each wavelength.

As in the case of current density-voltage measurements, the EQE may be measured at cryogenic temperatures with the aid of a Linkam THMS600E cryostat and a Linkam LNP95 temperature control system.

2.4. Photoluminescence

The primary means of assessing sample's optical properties employed in this thesis is photoluminescence (PL) spectroscopy. By illuminating a sample with laser light, absorption of photons results in excited carriers. If these carriers are not extracted, they will eventually undergo recombination. Radiative recombination, from electrons in the zero momentum Γ valley of the conduction band recombining with holes in the valence band, will result in photon emission. The variance of the photon energies produced in

this process provides a great deal of information about the carrier distribution, and enables analysis varying from determination of a material's bandgap to enabling the hot carrier temperature analysis discussed in Chapter 1. The laser light may be applied to the sample at an angle (in the current set up), while a series of lenses in front of the sample can focus the light produced by photoluminescence to a spectrometer. Figure 2.4 provides a schematic representation of this experimental setup used for this work.

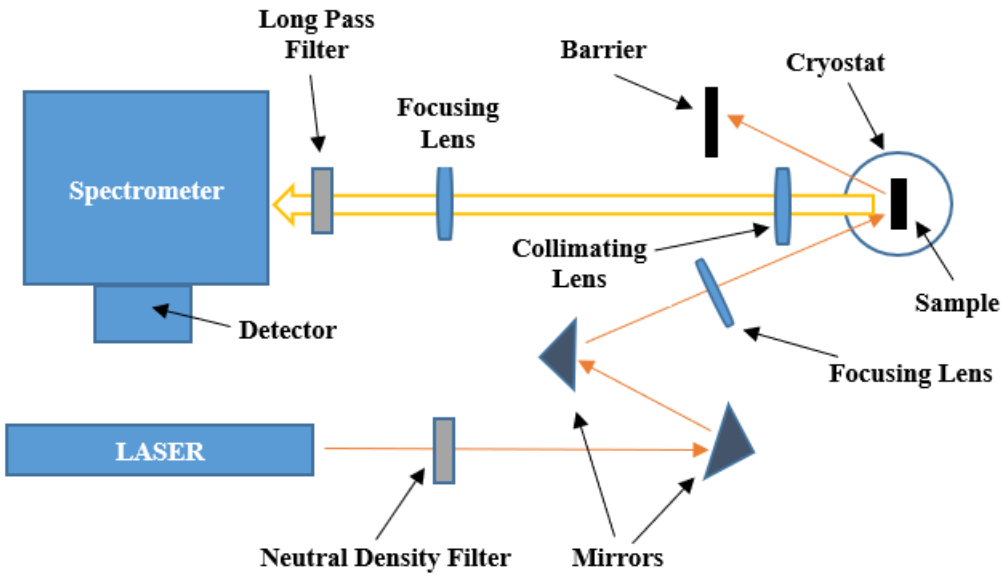

Figure 2. 4. Schematic representation of the experimental setup for PL measurements with the closed cycle helium cryostat and the InGaAs detector. The thin orange arrows show the beam path of the laser, while the white block arrow outlined in gold shows the PL spectrum.

A 442 nm He-Cd laser, a 1064 nm solid state laser diode, and a 532 nm Nd:YVO_4 crystal-based laser provided the laser illumination for the PL measurements. Samples were mounted in a cryostat with integrated electrical connections for both PL and

monochromatic *J-V* measurements (via a Keithley 2400 multimeter), with two experimental arrangements employed. For a wider range between 4.2 K and 300 K, a Janis SHI-4 closed cycle helium system and a Lake Shore Cryogenics Model 335 temperature controller were used, and PL data recorded via a Princeton Instrument Acton SP2500 spectrometer and InGaAs linear array cooled by liquid nitrogen for 750 nm to 1600 nm detection. Shorter wavelengths may be detected via an attached silicon charged couple device 2-D array, though the longer wavelength range better served the studies presented in this thesis.

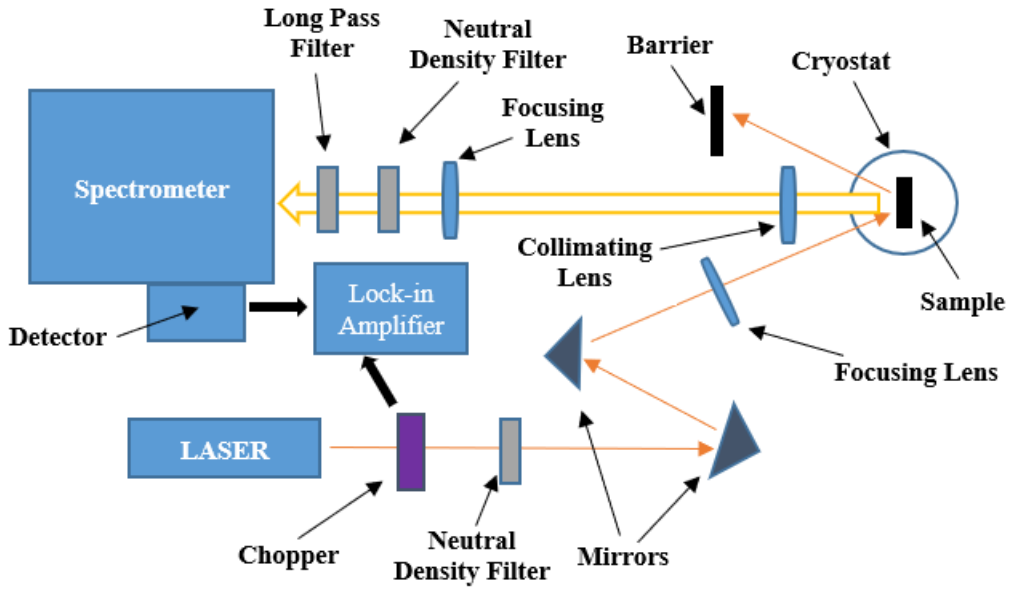

Figure 2. 5. Schematic representation of the experimental setup for PL measurements with the liquid nitrogen cooled cryostat and the Ge detector. The thin orange arrows show the beam path of the laser, while the white block arrow outlined in gold shows the PL spectrum. The black block arrows show connections to the lock-in amplifier.

The second PL system comprised an Edinburgh Instruments single channel Ge photodiode cooled by liquid nitrogen and paired to a SPEX 270m spectrometer, as shown in Figure 2.5, with 77 K to 300 K temperature variation through liquid nitrogen cooling enabled by a Janis ST-100 cryostat and a second Lake Shore Cryogenics Model 335 temperature controller. The use of a Ge (rather than InGaAs) detector in this system enables measurement of long wavelengths due to the lower band gap of germanium (1800nm). A chopper is placed in the beam path prior to the cryostat, and synced to the detector signal via a Stanford Research Systems Model SR830 lock-in amplifier.

For power dependent measurements, neutral density filters are inserted into the laser beam path prior to the cryostat for the 442 nm or 1064 nm lasers. The power control system of the 532 nm laser permitted the widest range of power dependence to be examined without introducing additional optical elements. Very high-power measurements with the single channel Ge photodiode were comparatively prone to saturation due to the SPEX 270m lacking the integrated exposure time control the Acton SP2500 spectrometer features via to an attached high-speed shutter. Placing neutral density filters in the path between the cryostat and the spectrometer compensated for this, though calibration was necessary to account for resulting the modification of the detected PL spectrum.

References

[1] Shockley, William, and Hans J. Queisser. "Detailed Balance Limit of Efficiency of p-n Junction Solar Cells." *Journal of Applied Physics* 32, no. 3 (1961): 510-19.

[2] Guillemoles, Jean-Francois, Thomas Kirchartz, David Cahen, and Uwe Rau. "Guide for the Perplexed to the Shockley–Queisser Model for Solar Cells." *Nature Photonics* 13, no. 8 (2019): 501-05.

[3] "ASTM E-490 Reference Spectra." National Renewable Energy Laboratory. Accessed 1 November 2022. https://www.nrel.gov/grid/solar-resource/spectra-astm-e490.html

[4] "ASTM G173 - 03 Reference Spectra." National Renewable Energy Laboratory. Accessed 1 November 2022. http://rredc.nrel.gov/solar/spectra/am1.5/

[5] Mazzio, Katherine A., and Christine K. Luscombe. "The Future of Organic Photovoltaics." *Chemical Society Reviews* 44, no. 1 (2014): 78-90.

[6] Deng, Xin-Hua, Jiang-Tao Liu, Ji-Ren Yuan, Qing-Hua Liao, and Nian-Hua Liu. "A New Transfer Matrix Method to Calculate the Optical Absorption of Graphene at Any Position in Stratified Media." *Europhysics Letters* 109, no. 2 (2015): 27002.

Chapter **3**

Hot Carrier Behavior in InAs/AlAsSb Multi-Quantum Well Devices

3.1. Introduction

A proposed method for surpassing the single gap device efficiency limits [1] via hot carrier protocols [2] is the Type-II Quantum Well [3]. Dimensional constraints result in a smaller population of the acoustic phonons that feature in the Klemens [4] or Ridley [5] pathways of the dominant III-V material thermalization mechanisms, and hence quantum wells or quantum dots have enhanced potential for thermalization loss mitigation [6,7]. A Type-II system further separates electrons and holes, which lowers recombination rates and enables the properties of the barrier layers to become more influential [8]. This provides a potential pathway to improved hot carrier devices, via careful choice of absorber and barrier materials.

Prior work at the University of Oklahoma examined InAs/AlAsSb Multi-Quantum Well (MQW) samples. These structures were not devices, but rather undoped structures for optical analysis via photoluminescence, and subsequent analysis of the hot carrier temperature revealed promising evidence of a hot carrier population. Analysis of the localization properties [9], phononic behavior [10] and carrier lifetimes [11] supported the claim that this system could maintain a hot carrier population, and was improved in this purpose at temperatures >100 K, whereupon delocalization occurred and the

structure fully featured Type-II behavior (holes to the barrier layer, electrons to the InAs layers) rather than trapping carriers into a quasi-Type I configuration (low energy traps due to interface states and alloy fluctuations preventing the carriers from separating) [9].

This chapter presents the study of full devices based upon the InAs/AlAsSb multi-quantum well structure, with a focus on the hot carrier mechanisms prompted by the intriguing intransigence with regards to power observed in the hot carrier temperatures of the optical samples [9, 10, 11].

3.2. Device Structure

The first device structure consisted of n^+-$Al_{0.35}In_{0.65}As$ atop an intrinsic InAs/$AlAs_{0.16}Sb_{0.84}$ Multi-Quantum Well region, with p^+-$AlAs_{0.16}Sb_{0.84}$ finalizing the diode [12]. This was grown atop p^+ GaAs substrate by molecular beam epitaxy, and is schematically illustrated in Figure 3.1. To allow the quantum well region to be lattice matched, the p^+-AlAsSb layer was grown well beyond epitaxial thickness to allow strain relaxation and thereafter grow the quantum wells epitaxially upon the lattice parameters of the AlAsSb. The GaSb cap layer in the schematic was grown to prevent oxidation. The active absorber region consists of a set of 2.1 nm InAs quantum wells, separated by 5 nm AlAsSb barrier layers, with additional thickness of intrinsic AlAsSb included on each side of the absorber region to protect the quantum wells from dopant infiltration, and further confines the carriers in the quantum well region.

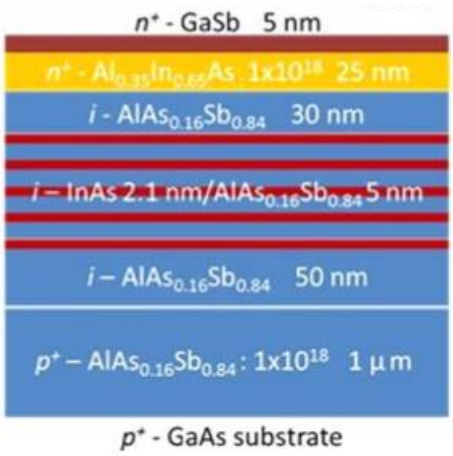

Figure 3. 1. Schematic summary of device layers for the first device. Device layers as grown for this study by molecular beam epitaxy. [Reproduced from: *Whiteside, V. R., et al. "The Role of Intervalley Phonons in Hot Carrier Transfer and Extraction in Type-II InAs/AlAsSb Quantum-well Solar Cells." Semiconductor Science and Technology 34, no. 9 (2019): 94001.*] [12]

Subsequently, a further set of three structures were grown in the same fashion, schematically illustrated in Figure 3.2 below. The majority of the structure is maintained, however the n^+ layer is n-doped AlAsSb rather than AlInAs, with the intent of significantly altering the extraction pathway, as the previous sample was designed to probe dependencies of tunneling and thermionic emission, rather than aim for an effective extraction mechanism [12]. The central alteration between the three devices is the thickness of the AlAsSb barrier layers. The set of ten 2.1 nm InAs quantum wells is maintained, while the AlAsSb layers that separate them are varied between 2.12 nm, 5.15 nm and 10 nm in thickness.

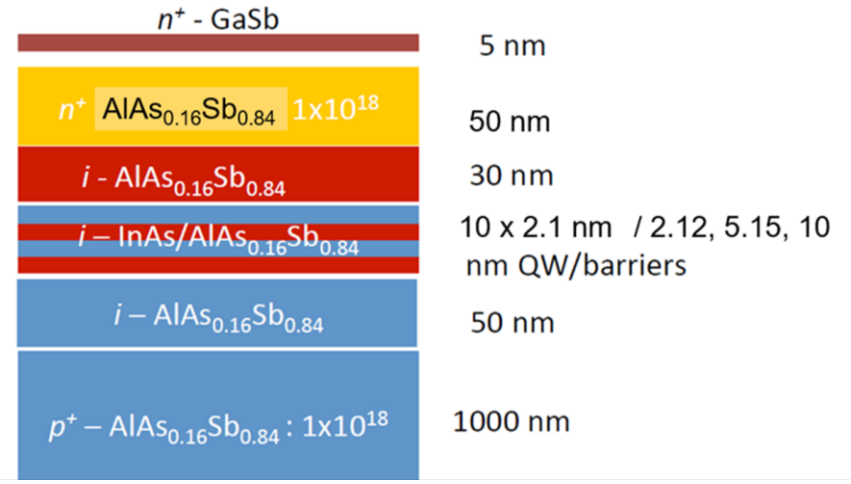

Figure 3. 2. Schematic summary of device layers for the altered barrier thickness devices. The devices were grown by molecular beam epitaxy atop p^+ GaAs substrate.

The alteration of the barrier thickness substantially alters the thickness of the intrinsic region, and has an impact on the phonon properties of the multi-quantum well region [13]. To provide clarity on the energy levels of the quantum wells, Figure 3.3(a) schematically illustrates a portion of the superlattice. It should be noted that AlAsSb is an indirect gap material, with the lowest energy valley of the conduction band being the X-valley rather than the Γ-valley (the direct bandgap). Using NRL Multibands ® for k·p analysis to determine an appropriate bandgap (based on the ground state of the quantum well and first heavy hole band) that could be used to model the InAs/AlAsSb superlattice as a hypothetical material with such a bandgap, then employing the integrated Poisson solver to determine band alignments for the structure, Figure 3.3(b) below was created to illustrate the band offsets [14]. The extraction pathway via the Γ valley and quantum well ground state is evidently non-viable due to the potential offset, leaving extraction to involve upper valleys of the band structure and tunneling.

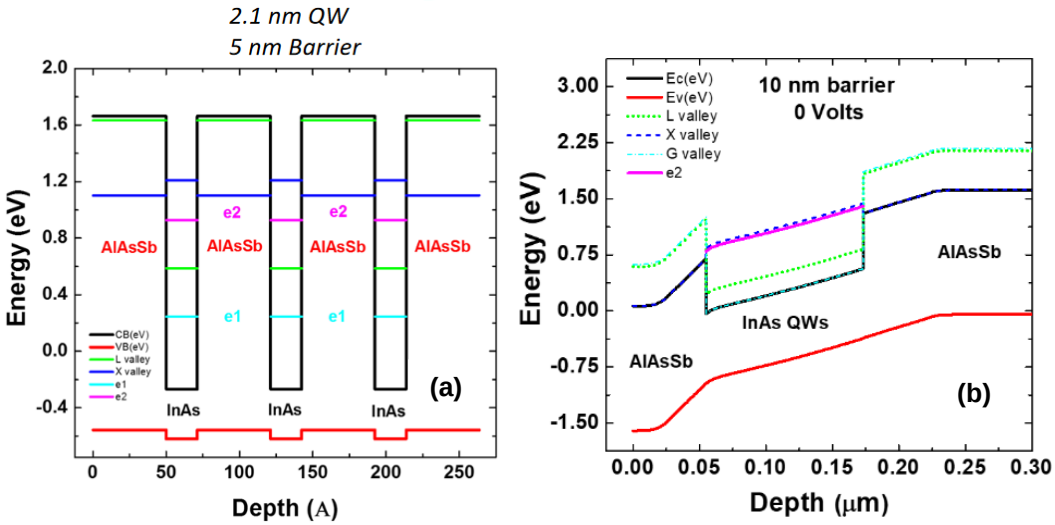

Figure 3. 3. (a) Schematic representation of the energy levels of the InAs/AlAsSb multi-quantum well region. In addition to the upper valleys of the conduction band (L and X), the ground (e1) and first excited (e2) states of the InAs quantum wells are shown. [Reproduced from: *Whiteside, V. R., et al. "The Role of Intervalley Phonons in Hot Carrier Transfer and Extraction in Type-II InAs/AlAsSb Quantum-well Solar Cells." Semiconductor Science and Technology 34, no. 9 (2019): 94001.*] [12] (b) NRL Multibands ® simulation of the structure for the 10 nm barrier case.

The upper valleys of the conduction band are relevant in this device, as they are rendered accessible in two ways. First, through intervalley phonon scattering, the rates for which are presented in Figure 3.4(a) in contrast with the polar optical phonons (labeled Γ-valley) that are key to the Fröhlich to Klemens or Ridley thermalization pathway that is dominant in III-V materials [11, 15]. Second, through the Gunn Effect in the presence of electric field, carriers may transition between metastable states of the conduction band, being provided with energy and momentum by the field to transition

away from the Γ valley [16]. Valley occupancy calculations for InAs as a function of electric field strength are presented in Figure 3.4 (b).

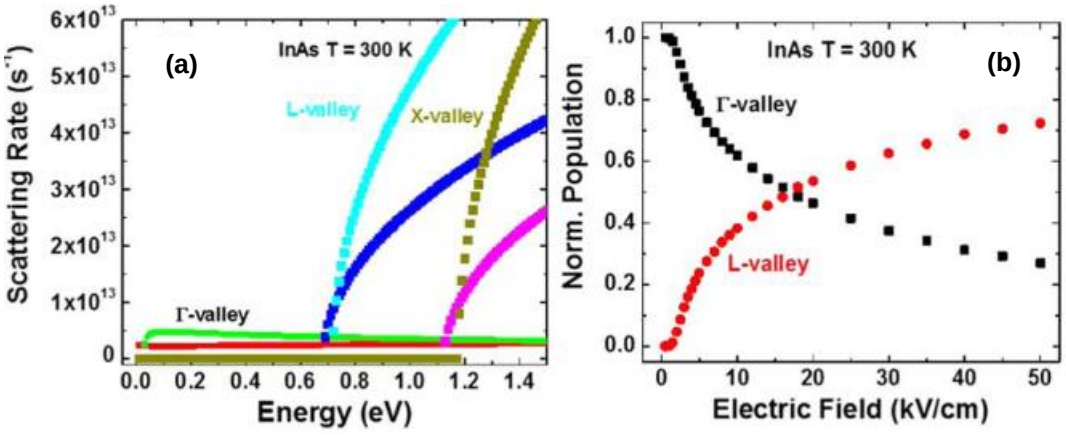

Figure 3. 4. (a) Comparison of the scattering rates as a function of carrier energy above the bandgap for emission (green, cyan, saffron) and absorption (red, blue, magenta) for polar optical phonons (marked Γ-valley) and intervalley phonons (from Γ to L or X) in InAs at 300 K. (b) Occupation probability in the Γ- and L-valleys as a function of electric field in InAs at 300 K. [Reproduced from: *Whiteside, V. R., et al. "The Role of Intervalley Phonons in Hot Carrier Transfer and Extraction in Type-II InAs/AlAsSb Quantum-well Solar Cells." Semiconductor Science and Technology 34, no. 9 (2019): 94001.*] [12]

Given the confinement provided by the quantum wells, it may be somewhat presumptive to assume consistent acceleration across a thickness equal to the sum of the InAs wells or across the whole superlattice. Moreover, Figure 3.4(b) holds the implicit assumption that all carriers start at the conduction band edge, which artificially depreciates the upper valley occupancy, especially in a system with high intervalley

phonon scattering rates. It is nontrivial to ascertain the error this results in when comparing to a real system, but given that the electric field strength in this device is expected to exceed 25 kV/cm in the quantum well region [12], then while the precise occupancy percentages are not anticipated to match this idealistic calculation, the Gunn Effect should certainly not be discounted. The Gunn Effect is highly prevalent in InAs and its role high-electron-mobility transistor structures [17].

The ability of electrons to reach the L or X valleys of InAs is important to both the extraction mechanisms and the hot carrier behavior. Intervalley transfer is a means of thermalization loss mitigation in InAs due to the heightened energy at which the carriers are stored. Time resolved spectroscopy of GaAs has demonstrated experimentally that intervalley scattering may slow carrier return to the conduction band edge, and the resulting photoluminescence spectra are characterized by heightened temperatures as a result [18]. In regards to the current density, Figure 3.3(a) illustrates that electron occupancy in the L or X may substantially improve extraction, as compared to the ground state of the quantum well the L or X valleys face lower potential offsets and shorter tunneling distances.

The samples were processed via standard photolithographic and wet etching techniques into a 6.25 mm^2 mesa, and via thermal evaporation was finalized into devices with top (n-type) finger contacts of 120 nm Indium then 30 nm Au, and bottom (p-type) contact of 10 nm Ni then 120 nm Au/Ge alloy (12% by weight Ge).

3.3. Photoluminescence Measurements

Temperature dependent photoluminescence measurements were taken with 442 nm wavelength laser illumination, providing 2.8 eV per photon. When compared to the energy levels in Figure 3.3(a), this is more than sufficient to enable a carrier in one of the InAs quantum wells to reach any of the available energy levels, and as shown in Figure 3.4(a) provides intervalley scattering the opportunity to dominate the over the Γ-valley state occupancies (e1 and e2, the ground and first excited states of the quantum well). The results for the 10 nm barrier case, with carrier temperature as difference from lattice temperature ΔT determined from the generalized Planck relation, are presented in Figure 3.5.

In these devices with built in field due to dopants and attendant enhanced carrier extraction, photoluminescence intensities are not as large as was observed in the first device with the n^+ InAlAs top layer (Figure 3.1) [12], which indicates improved electrical behavior. Given the *Jsc* for the 442 nm monochromatic illumination was ~0.005 mA/cm^2 in the initial device [12] an improvement in operation can easily be achieved. The consequence is unfortunate however, as low signal to noise ratio limits the available data for full temperature analysis, seen in the noise of Figure 3.5(a) and (b), and the ΔT against lattice temperature plot (Figure 3.5(c)). The runaway increase in ΔT as lattice temperature increased, especially above 200 K, is primarily a product of increasing thermal noise, and as such these data provide little physical information.

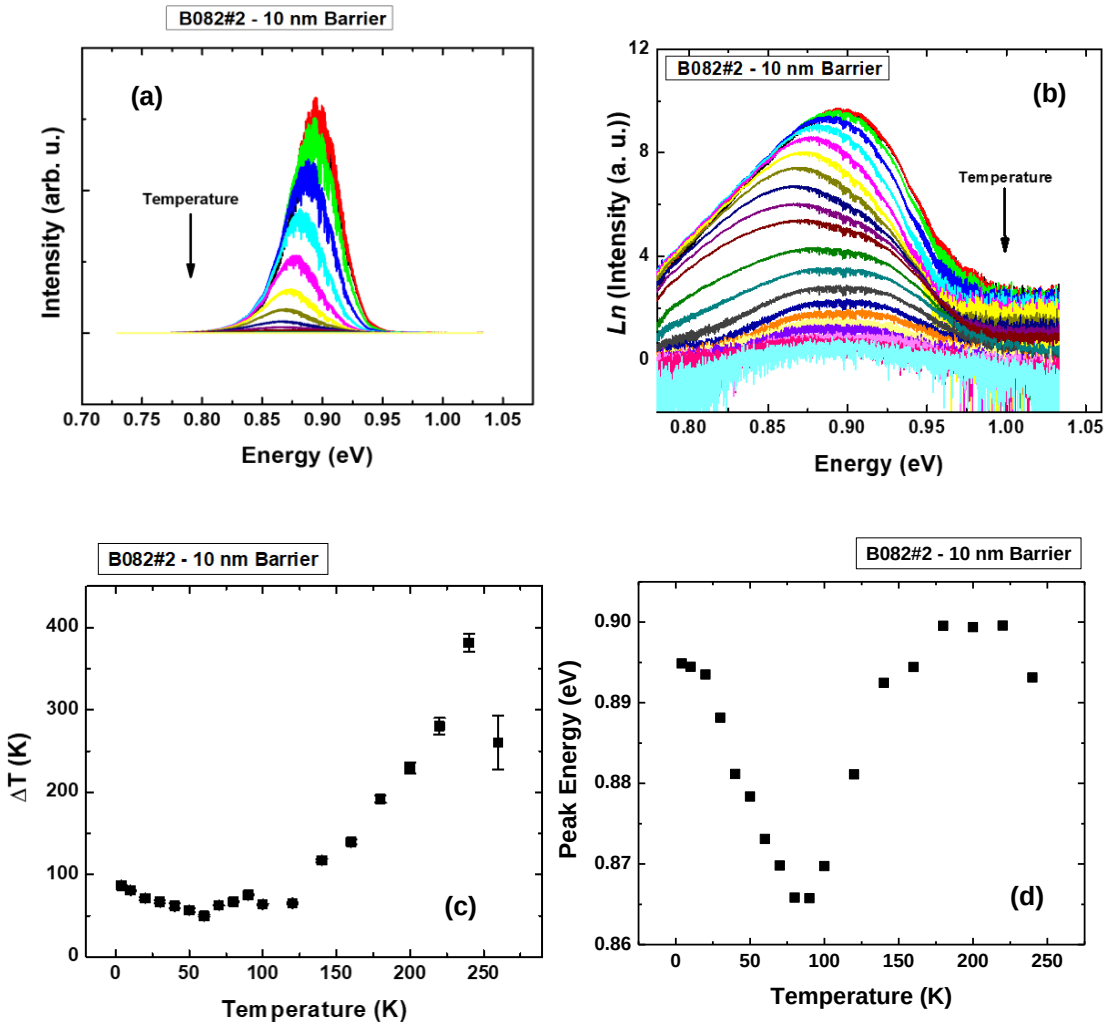

Figure 3. 5. (a) Temperature dependent photoluminescence measurements of the 10 nm barrier sample. (b) As (a), but taking the natural logarithm to fit the high energy tail to the generalized Planck relation and determine the temperature of the carrier distribution. (c) Carrier temperature as difference from lattice temperature, plotted against lattice temperature. (d) Peak energy of the photoluminescence as a function of lattice temperature.

These caveats established, the presence of an observable hot carrier population is in good agreement with prior results [9, 10, 11, 12], and a change in behavior at ~100 K is also consistent. The existence of a relatively stable ΔT before ~100 K in Figure 3.5(c) has been observed in prior optical samples [9], and the peak energy trend shifting at ~100 K in Figure 3.5(d) is also familiar [9, 12]. This temperature trend is associated with the delocalization of carriers from defects and alloy fluctuations, and the ionization of such carriers at elevated temperatures such that the type-II nature of the MQW is revealed [11]. This behavior further mitigates thermalization and recombination, and is responsible for the altered temperature dependence with ΔT now increasing with temperature [11].

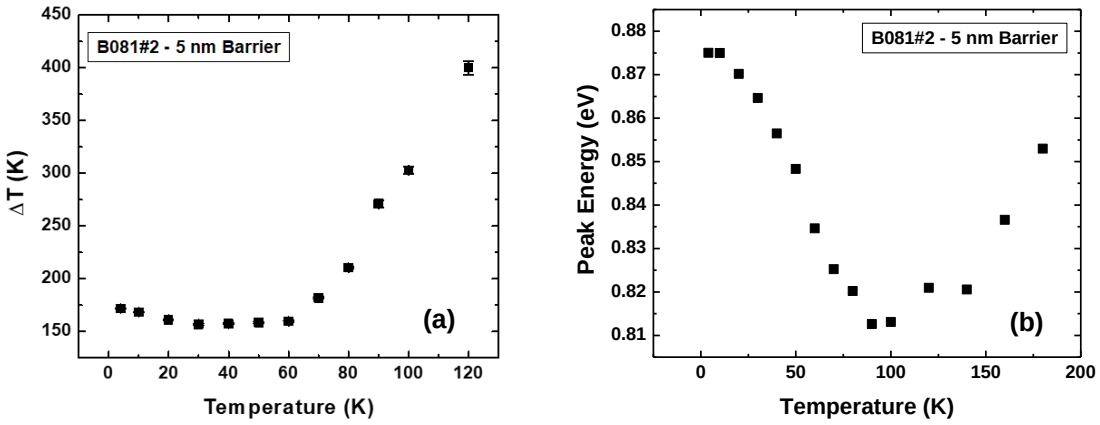

Figure 3. 6. (a) Carrier temperature as difference from lattice temperature, plotted against lattice temperature for the 5 nm AlAsSb barrier thickness device. (b) Peak energy of the photoluminescence as a function of lattice temperature.

A similar analysis is presented for the 5 nm barrier layer device, shown in Figure 3.6. This device is further limited by the signal to noise ratio, likely due to a combination of

thinner quantum well region and weaker confinement. It can be seen in Figure 3.6(b) that the peak energy follows the previous pattern, but in Figure 3.6(a) the carrier temperature begins increasing earlier. Given the same proportion of data points as before are increasing, and the peak energy is consistent, this is more readily attributable to thermal noise becoming a problem earlier due to low signal than *to any more fundamental change*.

Regrettably, this trend continues for the 2 nm barrier thickness, and there is little that may be successfully analyzed from the photoluminescence. It is noisy, and a simple to analyze high energy tail is difficult to identify above that noise. The spectrum is presented in Figure 3.7 below, but no analysis of the carrier temperature can confidently accompany it.

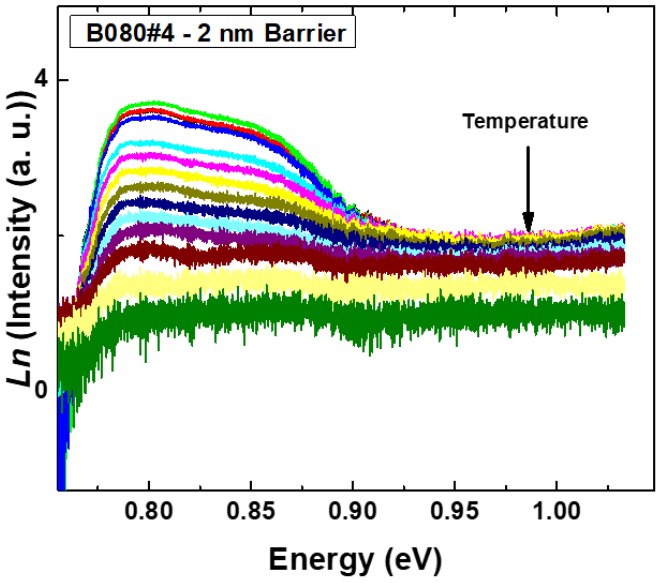

Figure 3. 7. Natural logarithm of the intensity of the photoluminescence as a function of energy for the 2 nm barrier thickness device.

At this juncture, it becomes necessary to raise the question of how far and to what extent any of the presented carrier temperature may be relied upon. The issue of signal to noise ratio is a solvable one in this case, though not trivially in practice due to equipment limitations. The overarching, more fundamental concern is that this analysis of a quantum well system is being performed with a technique designed for bulk systems. There have been substantial gains made in understanding the requirements and difficulties of hot carrier temperature analysis recently [19], and a major result of that analysis is that it cannot be assumed that this analysis will apply with accuracy to any given quantum well system.

In this case, however, a more full-fledged analysis has been performed that lends credence to the data in Figure 3.5(c) and Figure 3.6(a). Careful full spectral fitting, and fitting of the hole and electron temperatures separately for InAs/AlAsSb, has produced the same numerical results as the fitting of the high energy tail to the generalized Planck relation [20]. It is simply necessary to keep in mind that the hot carrier temperature truly refers to hot electrons in this system – the hole confinement is much weaker, as can be seen in Figure 3.3(a), and the holes are not transferred to or maintained in enhanced energy states with the same techniques as the electrons are.

In these measurements ultimately, the relatively low fluence of the 442 nm He-Cd laser limited the access to high signal to noise, which coupled with the type-II band alignments screened much of the hot carrier physics in the system. Follow-up measurements (after later setup of a 532 nm wavelength laser) were performed on these devices by Dr. Brandon Durant, enabling exploration of a wider range of powers, revealing the previously identified power insensitivity at low powers [10, 12] eventually changes into

power dependence at very high power. This is not attributed to laser heating, as analysis of the GaAs substrate's photoluminescence peak allowed the change in temperature to be determined relative to the lattice temperature indicated by the GaAs substrate spectrum.

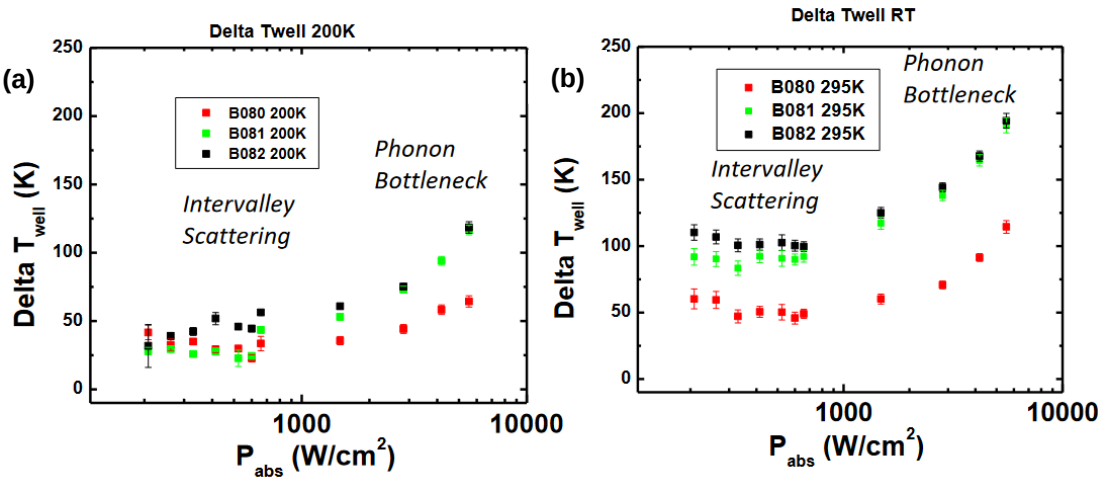

Figure 3. 8. Power dependent difference from lattice temperature (determined by comparison to GaAs substrate peak) at (a) 200 K and (b) 295 K lattice temperature for 2 nm (red), 5 nm (green) and 10 nm (black) AlAsSb barrier thicknesses. Credit: Brandon K. Durant

This result also demonstrates a relation between stronger confinement in MQWs with thicker barriers and higher hot carrier temperature at room temperature (Figure 3.8 (b)), but a less orderly distinction at 200 K (Figure 3.8 (a)). This trend robustly matches the results from hyperspectral imaging performed on these samples at L'Institut Photovoltaïque d'Ile de France [13]. This associates the higher hot carrier temperatures with enhanced relevance of AlSb phononic properties, which helps mitigate thermalization mechanisms [11, 13].

3.4. Electronic Behavior

Simultaneous with the photoluminescence measurements, at each temperature the mounted sample under 442 nm laser excitation was also measured for its current density-voltage characteristic. Figure 3.9(a) shows this measurement for the 2 nm barrier sample, and reveals the presence of an inflection that decreases the open circuit voltage (*Voc*). This is similar to results seen for the first device (Figure 3.1) [12] and indicates a limitation in the carrier extraction. Key data for the solar cell behavior (*Voc* and *Jsc*) is extracted from the curves to Figure 3.9(b).

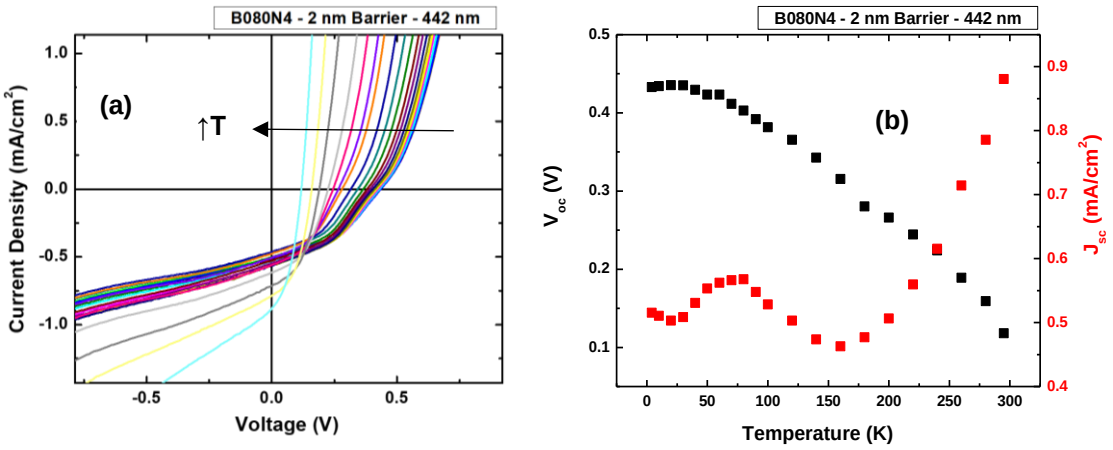

Figure 3. 9. (a) Temperature dependent current density-voltage measurements under 442 nm wavelength illumination for the 2 nm barrier sample. (b) Extracted *Voc* (black) and *Jsc* (red) values from the *J-V* curves in (a).

The *Voc* decreases with temperature, which is a trend matched to the decreasing bandgap as temperature rises, however there are subtleties to this that must be noted. First and foremost, while a simple comparison of the bandgap of InAs to the open circuit voltage appears promising at low temperature this requires some care. Indeed, the

bandgap of InAs at 4 K is ~ 0.415 eV, which the *Voc* exceeds [21]. However, as was discussed previously regarding Figure 3.3(b), the quantum well ground state is of higher energy than the conduction band edge of bulk InAs, and this is not indicative of hot carrier behavior exceeding normal quantum well effective bandgap enhancement. The quantum well's enhanced ground state is not an efficiency gain, as it merely causes a higher effective bandgap. The normal (although usefully tunable) tradeoff between transmission loss and thermalization loss remains for such a single gap device [22]. Figure 3.3(a) shows with more clarity that even at room temperature, a *Voc* in excess of 0.9 eV would be desirable for hot carrier solar cell operation, and at 4 K the bandgap is increased rather than decreased in III-V materials. The *Voc* is visibly depreciated by the inflection at low temperatures, and trades photovoltage for current density at room temperature.

Figure 3.9(b) shows the temperature dependence of *Jsc* extracted from 3.9(b) plotted as positive values for clarity. As the temperature increases as does the *Jsc*, which indicated increased carrier extraction at high temperatures. Compared to an efficient bulk device, these current density values are relatively low, however in comparison to the first device (10 nm barrier) measured in this series of MQWs with an AlInAs barrier (Figure 3.1) the *Jsc* is improved by more than an order of magnitude despite possessing the same InAs absorber thickness [12]. This is attributed to the n^+ AlAsSb layer, which permits a reasonable X to X valley alignment (Figure 3.3(b)) and therefore carrier extraction at the top interface and does not face a L to Γ valley transfer and a large barrier to extraction observed in the AlInAs based system, which requires tunneling [12], which is unfavorable due to the high density of states difference across the L and Γ valley [23].

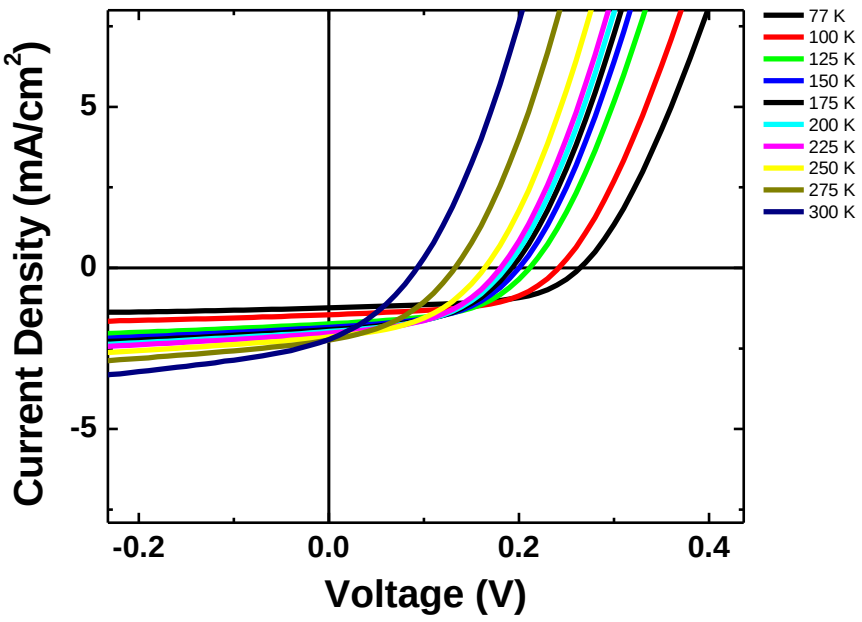

Figure 3. 10. Temperature dependent current density-voltage measurements under 1 Sun AM1.5G illumination for the 2 nm barrier sample.

Temperature dependent current density-voltage (J-V) measurements at 1-sun AM 1.5G equivalence are shown Figure 3.10. The temperature dependence was performed in a liquid nitrogen microstat rather than a closed cycle helium system, limiting the range of temperatures that may be probed, but providing the utility of examining the behavior under more practical broad band illumination. For the previously examined 2 nm InAs/ 5 nm AlAsSb MQW device (Figure 3.1), as temperature decreased, both *Voc* and *Jsc* decreased due to the inflection of the *J-V* curve [12]. The results shown in Figure 3.10 for the *J-V* curve under the solar simulator with a 2 nm barrier appear more conventional, and under broad spectrum illumination there is little evidence of an inflection as was seen under 442 nm wavelength monochromatic illumination in Figure 3.9. This suggests that the enhanced temperature of the carrier distribution due to the increased lattice

temperature - as well as the previously the residual field aided non equilibrium carrier effects results in enhanced current extraction due to the degeneracy of the carrier with respect to the parasitic barrier in the system.

The next sample in this series was a InAs/AlAsSb p-i-n solar cell with a 5 nm AlAsSb barrier, upon which the measurements described above were repeated. The monochromatic *J-V* measurements excited at 442 nm are shown in Figure 3.11(a) and the extracted *Jsc* and *Voc* in Figure 3.11(b). The *Voc* follows a similar trend to that of the 2 nm barrier device, but the *Jsc* has taken on a more step-like form, rather than a smooth dependence.

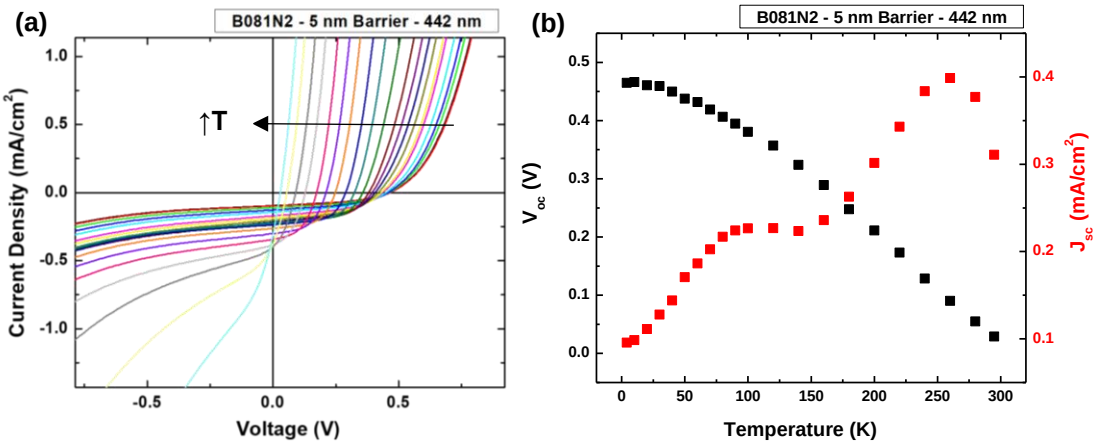

Figure 3. 11. (a) Temperature dependent current density-voltage measurements under 442 nm wavelength illumination for the 5 nm barrier sample. (b) Extracted *Voc* (black) and *Jsc* (red) values from the *J-V* curves in (a).

At higher temperatures, and particularly when approaching ambient, a depreciation of *Voc* provides a negative impact on the *Jsc*, despite the qualitative trend of the current density following an expected dependence up to ~ 280 K where thermal energy might be

expected to improve thermionic emission from the QWs and result in enhanced carrier collection. Above 280 K a parasitic channel resulting in a loss of rectification and high resistance becomes evident in both the *J-V* and extract *Jsc*, the origin of which remains unclear. The unusual effects in the temperature dependent *J-V* between 100 K and 150 K also represent atypical behavior not observed in either the 2nm (Figures 3.9 and 3.10) and 10 nm (Figure 3.11 and 3.12) barrier devices. As such, it appears that this may represent a transition regime in which carrier transport is perturbed by a subtle combination of thermionic emission and tunneling, coupled with the effect of the transition from a localized quasi-Type-I like regime to that of a purely Type-II system as carriers ionize from alloy fluctuations and defects at the AlAsSb/InAs interface, a property seen several times in optical measurements from analogous superlattice structures [9,10]. As Figure 3.5(d) and Figure 3.6(b) demonstrated, defects and alloy fluctuations are resolved with increasing temperature until the available thermal energy resolves the non-idealities sufficiently at ~150 K. The electrons and holes then separate into the InAs and AlAsSb portions of the superlattice respectively, decreasing radiative losses via the spatial separation of the photogenerated charges that results in Type-II systems [11].

The *J-V* measurements under the solar simulator for the MQW with the 5 nm barrier is presented in Figure 3.12, and once more features little evidence of the inflection viewed in the 2 nm barrier sample. This 5 nm barrier thickness is also well the matched to the MQW device with a AlInAs – rather than AlAsSb - top layer (Figure 3.1), but the inflection present in both the monochromatic (442 nm) and 1 Sun measurements in that

previous study [12] is no longer present in this *new* 5 nm barrier sample, and the electrical characteristics are significantly improved [12].

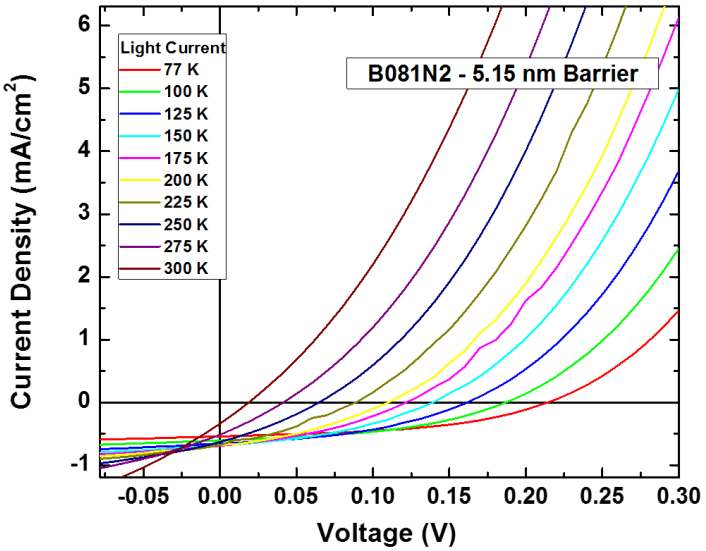

Figure 3. 12. Temperature dependent current density-voltage measurements under 1 Sun AM1.5G illumination for the 5 nm barrier sample.

Figure 3.13 concerns the 442 nm wavelength *J-V* data for the 10 nm barrier device. The dependence of the current density with temperature fits with the established trend, but it is the *Voc* that is shown in black in Figure 3.13(b) that presents novel behavior in this device. The value of the *Voc* above 150 K has a value consistent with the energy levels of the bands (~0.7 eV) seen in Figure 3.3(b) at ~ 0.33 eV, with a drop of ~ 0.4 eV with respect to the bandgap typical in solar cells operating via traditional electron and hole quasi-fermi levels. Once again, below 150 K the *Voc* is low, which presumably reflects the strong confinement in these MQWs due to the thicker barriers and enhanced radiative losses at lower temperature.

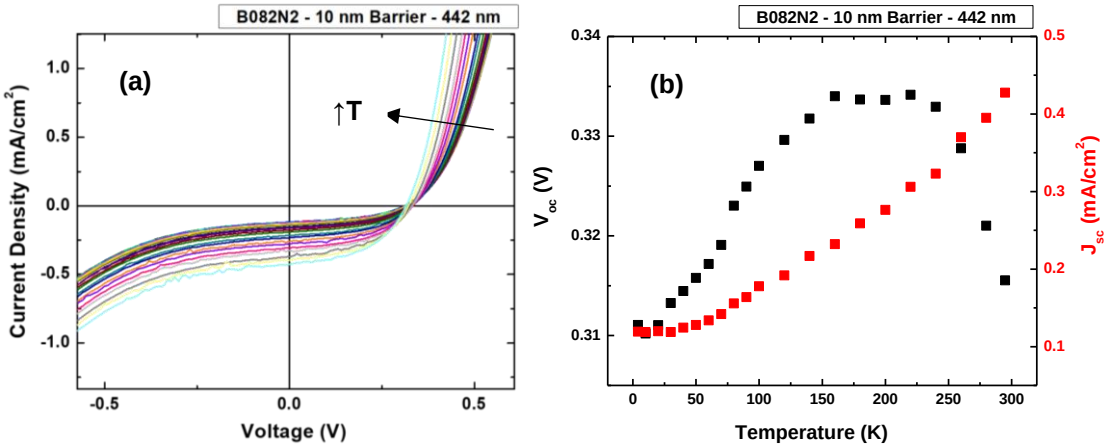

Figure 3. 13. (a) Temperature dependent current density-voltage measurements under 442 nm wavelength illumination for the 10 nm barrier sample. (b) Extracted Voc (black) and Jsc (red) values from the *J-V* curves in (a).

When considering the temperature dependent J-V under 1-sun AM 1.5G illumination in Figure 3.14, once again the while the *Jsc* increases as might be expected with a thermal reduction in the absorber bandgap, there is also a non-traditional (or larger) reduction in *Voc* than expected, which typically represents the thermal activation of non-radiative channels. This large reduction is well matched to the region of carrier delocalization at the MQW interfaces and implies the activation of non-radiative states have a negative effect on the diode likely due to the presence of traps and/or parasitic effects on the background doping concentration in the device and the quality of the p-n junction within the diode.

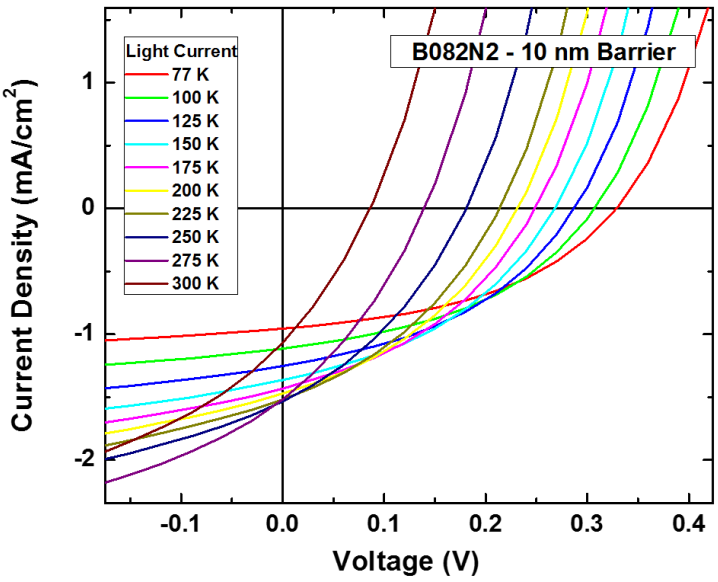

Figure 3. 14. Temperature dependent current density-voltage measurements under 1 Sun AM1.5G illumination for the 10 nm barrier sample.

Figure 3.15(a) provides a comparison of the temperature dependence of *Voc* for the three devices with various barrier thicknesses under monochromatic illumination. The *Voc* is approximately static for the 10 nm case (green) and it is also clear that although this device has a lower *Voc* at low temperatures with respect to devices with 5 nm (red) and 2 nm (black) barriers, respectively, it *exceeds* the others at higher temperatures, above 150 K. Here, the voltage clearly represents a truer reflection of the absorber bandgap once the recombination losses are circumvented at low T. In the case of the devices with thinner barriers, the voltage appears strongly perturbed by parasitic tunneling at low biases, supported by defect mediated carrier escape presumably due to defects at the interfaces and dominant role these have on the relatively thin barriers. This is supported by the low carrier extraction observed for the MQW with a 10 nm

barrier with respect to those with thinner barriers shown in Figure 3.15(b). While the thinner barriers demonstrate larger Jsc, these numbers are still poor and further reflect the dominance of non-radiative processes at higher temperatures in this series of devices.

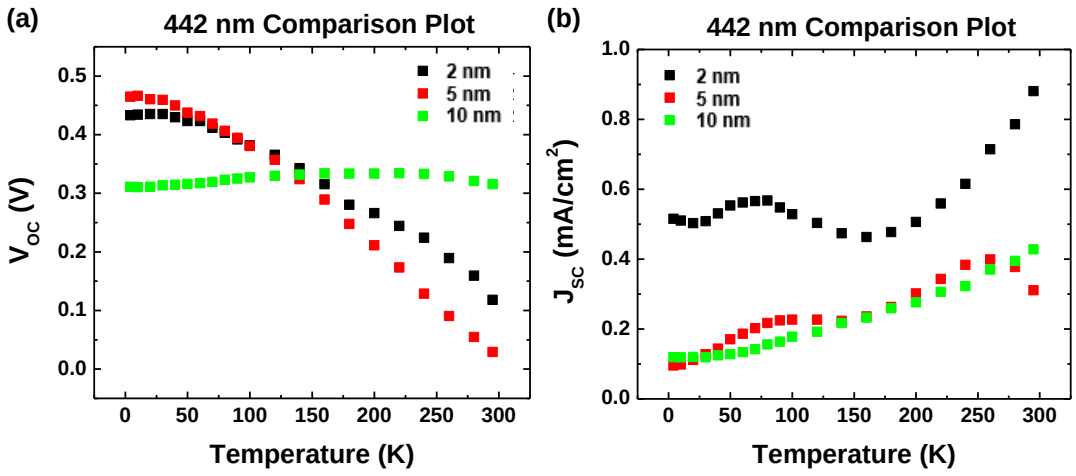

Figure 3. 15. Temperature dependence of the open circuit voltage (a) and short circuit current (b) under 442 nm wavelength laser illumination for the 2 nm (black), 5 nm (red) and 10 nm (green) barrier thickness devices.

Figure 3.16 presents the temperature dependent *Voc* and *Jsc* of the three devices under 1 sun AM 1.5G illumination. The devices with the 10 nm thick barriers provide better confinement and consequently the highest *Voc* (Figure 3.16(a)), while the 2 nm barrier device features the greatest *Jsc* (Figure 3.16(b)). Once again, the Voc is dominated in all cases by non-radiative losses and at room temperature the devices all operate at voltage levels significantly lower than their optimum bandgap value (~ 0.4 eV).

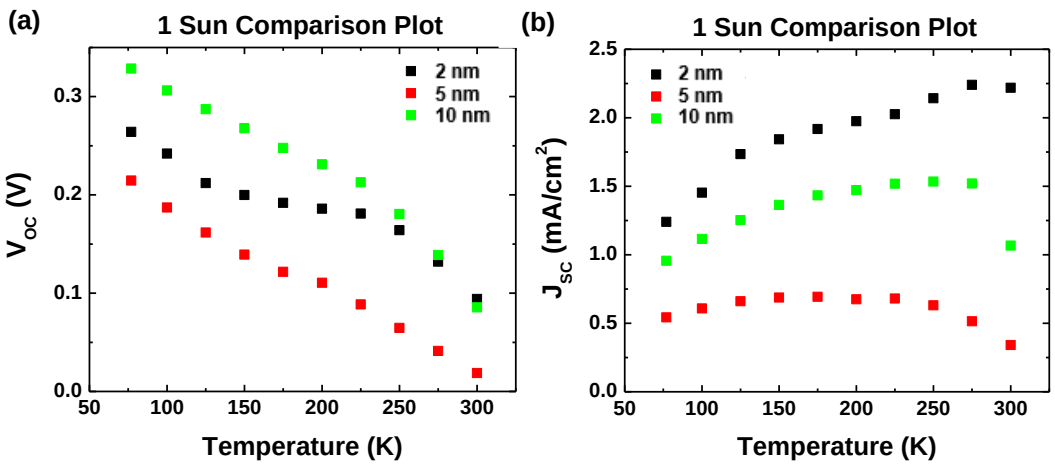

Figure 3. 16. Temperature dependence of the open circuit voltage (a) and short circuit current (b) under 1 Sun AM1.5G illumination for the 2 nm (black), 5 nm (red) and 10 nm (green) barrier thickness devices.

While this series of devices provide several interesting features in terms of their optical properties and the potential of phononic design [13], ultimately the dominance of non-radiative recombination and parasitic transport channels limit the physical information that can be extracted from these systems via their electrical measurements, and a new generation of devices must therefore be designed that build on the experience of these prototypes, or first generation systems, to further understand hot carrier effects in devices based on these systems

3.6. Conclusions

In this chapter, InAs/AlAsSb Multi-Quantum Well (MQW) structures are investigated in a set of devices with different barrier thicknesses. The results are consistent with the intriguing hot carrier behavior that prompted these studies, and the dependencies with

regards to laser fluence in PL measurements are better explained by the intrusion of intervalley phonon scattering rather than by attributing the hot carrier behavior simply to the Type-II QW aided phonon bottlenecks that inhibit the Klemens and/or Ridley processes. The complexities of the multi-quantum well system will require further investigation, but the study favors the thicker barriers for stronger hot carrier effects. The electronic measurements indicate that this device has yet to feature the desired hot carrier behavior, and the current extraction pathways do not suffice. This type-II superlattice is anticipated to be an excellent structure for further development as a hot carrier device. However, in the context of this thesis, this chapter provides a different hypothesis – if the proposition that the hot carrier behavior is power independent at low powers in this system due to intervalley effects is correct, then given appropriate intervalley scattering properties, would it not be possible for similarly robust hot carrier behavior to occur in a bulk system?

References

[1] Shockley, William, and Hans J. Queisser. "Detailed Balance Limit of Efficiency of p-n Junction Solar Cells." *Journal of Applied Physics* 32, no. 3 (1961): 510-19.

[2] Ross, Robert T., and Arthur J. Nozik. "Efficiency of Hot-carrier Solar Energy Converters." *Journal of Applied Physics* 53, no. 5 (1982): 3813-818.

[3] Esmaielpour, Hamidreza. "Type-II Quantum Well Hot Carrier Solar Cells." PhD diss., University of Oklahoma, Norman, 2018. https://hdl.handle.net/11244/316752.

[4] Klemens, P. G. "Anharmonic Decay of Optical Phonons." *Physical Review* 148, no. 2 (1966): 845-48.

[5] Ridley, B. K. "The LO Phonon Lifetime in GaN." *Journal of Physics: Condensed Matter* 8, no. 37 (1996): L511-513.

[6] Rosenwaks, Y., M. C. Hanna, D. H. Levi, D. M. Szmyd, R. K. Ahrenkiel, and A. J. Nozik. "Hot-carrier Cooling in GaAs: Quantum Wells versus Bulk." *Physical Review B: Condensed Matter* 48, no. 19 (1993): 14675-4678.

[7] Conibeer, G., N. Ekins-Daukes, J-F. Guillemoles, D. König, E. C. Chou, C-W. Jiang, S. Shrestha and M. A. Green. "Progress on hot carrier solar cells." *Solar Energy Materials & Solar Cells* 93, (2009): 713-719.

[8] Levard, Hugo. "Phonon Engineering for Hot-Carrier Solar Cells." PhD diss., Université Pierre et Marie Curie, Paris VI, 2015. https://tel.archives-ouvertes.fr/tel-01123624/.

[9] Tang, J., V. R. Whiteside, H. Esmaielpour, S. Vijeyaragunathan, T. D. Mishima, M. B. Santos, and I. R. Sellers. "Effects of Localization on Hot Carriers in InAs/$AlAs_xSb_{1-x}$ Quantum Wells." *Applied Physics Letters* 106, no. 6 (2015): 061902.

[10] Esmaielpour, H., V. R. Whiteside, J. Tang, S. Vijeyaragunathan, T. D. Mishima, S. Cairns, M. B. Santos, B. Wang, and I. R. Sellers. "Suppression of Phonon-Mediated Hot Carrier Relaxation in Type-II InAs/$AlAs_xSb_{1-x}$ Quantum Wells: A Practical Route to Hot Carrier Solar Cells." *Progress in Photovoltaics: Research and Applications* 24, no. 5 (2016): 591-99.

[11] Esmaielpour, H., V. R. Whiteside, H. P. Piyathilaka, S. Vijeyaragunathan, B. Wang, E. Adcock-Smith, K. P. Roberts, T. D. Mishima, M. B. Santos, A. D. Bristow, and I. R. Sellers. “Enhanced Hot Electron Lifetimes in Quantum Wells with Inhibited Phonon Coupling.” *Scientific Reports* 8, no. 1 (2018): 12473-9.

[12] Whiteside, V. R., H. Esmaielpour, T. D. Mishima, K. R. Dorman, M. B. Santos, D. K. Ferry, and I. R. Sellers. "The Role of Intervalley Phonons in Hot Carrier Transfer and Extraction in Type-II InAs/AlAsSb Quantum-Well Solar Cells." *Semiconductor Science and Technology* 34, no. 9 (2019): 94001.

[13] Esmaielpour, Hamidreza, Brandon K. Durant, Kyle R. Dorman, Vincent R. Whiteside, Jivtesh Garg, Tetsuya D. Mishima, Michael B. Santos, Ian R. Sellers, Jean-François Guillemoles, and Daniel Suchet. "Hot Carrier Relaxation and Inhibited Thermalization in Superlattice Heterostructures: The Potential for Phonon Management." *Applied Physics Letters* 118, no. 21 (2021): 213902.

[14] Lumb, Matthew P., Igor Vurgaftman, Chaffra A. Affouda, Jerry R. Meyer, Edward H. Aifer, and Robert J. Walters. "Quantum wells and superlattices for III-V photovoltaics and photodetectors." Paper presented at the Next Generation (Nano) Photonic and Cell Technologies for Solar Energy Conversion III, San Diego, California, October 2012. https://doi.org/10.1117/12.964654

[15] Fröhlich, H., H. Pelzer, and S. Zienau. "Properties of Slow Electrons in Polar Materials." *Philosophical Magazine (London, England: 1945)* 41, no. 314 (1950): 221-242.

[16] Gunn, J. B. "Microwave Oscillations of Current in III-V Semiconductors." *Solid State Communications* 88, no. 11 (1993): 883-86.

[17] Ayubi-Moak, J. S., D. K. Ferry, S. M. Goodnick, R. Akis, and M. Saraniti. "Simulation of Ultrasubmicrometer-Gate $In_{0.52}Al_{0.48}As/In_{0.75}Ga_{0.25}As/In_{0.52}Al_{0.48}As$ /InP Pseudomorphic HEMTs Using a Full-Band Monte Carlo Simulator." *IEEE Transactions on Electron Devices* 54, no. 9 (2007): 2327-338.

[18] Jagdeep Shah, B. Deveaud, T. C Damen, W. T Tsang, A. C Gossard, and P. Lugli. "Determination of Intervalley Scattering Rates in GaAs by Subpicosecond Luminescence Spectroscopy." *Physical Review Letters* 59, no. 19 (1987): 2222-225.

[19] Gibelli, François, Laurent Lombez, and Jean-François Guillemoles. "Accurate Radiation Temperature and Chemical Potential from Quantitative Photoluminescence Analysis of Hot Carrier Populations." *Journal of Physics. Condensed Matter* 29, no. 6 (2016): 06LT02.

[20] Whiteside, V. R., B. A. Magill, Matthew P. Lumb, H. Esmaielpour, M. A. Meeker, R. R. H. H. Mudiyanselage, A. Messager, S. Vijeyaragunathan, T. D. Mishima, M. B. Santos, I. Vurgaftman, G. A. Khodaparast, and I. R. Sellers. "Valence Band States in an InAs/AlAsSb Multi-quantum Well Hot Carrier Absorber." *Semiconductor Science and Technology* 34, no. 2 (2019): 25005.

[21] Fang, Z. M., K. Y. Ma, D. H. Jaw, R. M. Cohen, and G. B. Stringfellow. "Photoluminescence of InSb, InAs, and InAsSb Grown by Organometallic Vapor Phase Epitaxy." *Journal of Applied Physics* 67, no. 11 (1990): 7034-039.

[22] Guillemoles, Jean-Francois, Thomas Kirchartz, David Cahen, and Uwe Rau. "Guide for the Perplexed to the Shockley–Queisser Model for Solar Cells." *Nature Photonics* 13, no. 8 (2019): 501-05.

[23] Ferry, D. K. "In Search of a True Hot Carrier Solar Cell." *Semiconductor Science and Technology* 34, no. 4 (2019): 44001.

Chapter **4**

Hot Carrier Behavior via Intervalley Mechanisms in Bulk Heterostructures

4.1. Introduction

The hot carrier solar cell [1] is a proposal for overcoming the single gap efficiency limit [2], but evidence for practical pathways to implementing such a device have only recently begun to accumulate [3]. The hot carrier device based upon a large phononic bandgap and the creation of a phonon bottleneck has demonstrated proof of principle for detectable hot carrier behavior [4, 5, 6], but this alone is not sufficient for the hot carrier solar cell to become a practical device. To that end, in this chapter, the associated manuscript, and ultimately this thesis as whole, an alternative methodology is presented that obviates many of the difficulties in maintaining a hot carrier population under practical conditions.

The proposed method is to move beyond the bandgap and employ the band structure, which possesses multiple other local minima (‘upper valleys’) associated with the symmetry points of the Brouillon zone. Choosing an absorber material with the appropriate phonon scattering rates and energy levels, this has the potential to provide a robust stabilization effect for a hot carrier population in the upper valleys, which provide a valley-specific minimum energy in excess of the conduction band edge (Γ valley),

supporting a higher energy carrier distribution [7]. For this chapter, an InGaAs absorber heterostructure demonstrates proof-of-concept [8].

4.2. Device Structure and Intervalley Mechanisms

The chosen proof-of-concept device structure [7,8], schematically represented in Figure 4.1, is 20 nm n^+-$Al_{0.48}In_{0.52}As$/250 nm n-$In_{0.53}Ga_{0.47}As$/1000 nm p^+-$Al_{0.48}In_{0.52}As$ grown on p-InP substrate by Molecular Beam Epitaxy, with Si as the n-dopant and Be as the p-dopant. This structure is fully lattice matched zinc blende at that alloy composition, and benefits further from Molecular Beam Epitaxy's precision to minimize defects and calibrate dopant levels and alloy percentages. This is a benefit for the fundamental studies of the proposed mechanisms presented in this chapter, but Molecular Beam Epitaxy is not in any sense required for this device. The layers are well studied III-V materials, grown at bulk thicknesses, and hence the device structure can (and indeed, *has* after collaboration with Rochester Institute of Technology) be grown by industrial scale techniques such as Metalorganic Chemical Vapor Phase Deposition without loss of the relevant phonon scattering rates that drive the intervalley behavior.

The choice of InGaAs as the absorber layer was of primary importance for this structure. A hot carrier device should, with relation to the solar spectrum, have a comparatively low bandgap to better absorb a large portion of the spectrum as high energy (relative to the gap) photons. Hot carrier behavior is intended as a mitigation to thermalization loss, not transmission loss [9], and a large bandgap absorber would be counterproductive. The primary desired feature of a hot carrier solar cell is that this low bandgap would not be chained to a commensurately low operating voltage – that by

extracting from the excited carrier distribution the device maintains, the device would be enhanced in photovoltage beyond the bandgap. In summary, the device would absorb light with a low bandgap absorber, yet extract carriers as if the absorber material had a larger bandgap, ideally becoming more efficient in the process.

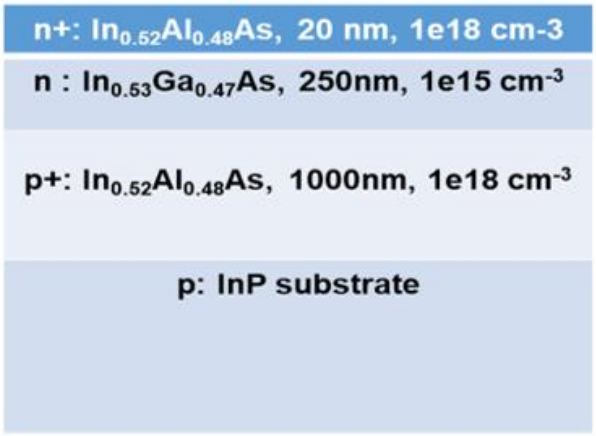

Figure 4. 1. Device layers as grown for this study by molecular beam epitaxy. Dopants in the epilayers were Si for n-type and Be for p-type.

In a conventional 'phonon bottleneck' driven hot carrier device, it is predicted that mitigation of phonons processes at the Klemens mechanism [10] for LO to LA thermalization step allows for a carrier distribution to have high energy carriers (and the 'hot' LO phonons those carriers emit) added to it under high illumination intensities faster than the rate of thermalization (meaning that numerous LO phonons cannot dissipate and are reabsorbed to support the hot carrier distribution) [11,12]. An energy selective contact could then, in principle, extract a large number of carriers from higher in the enhanced distribution than would normally be possible in a single gap device. For a 'valley photovoltaic' based hot carrier device, the principle is altered to take advantage

of the other metastable energy states higher in the conduction band, ‘valleys’ associated with the symmetry of the Brouillon zone [8]. For InGaAs, a Monte Carlo simulation of the band structure is presented in Figure 4.2(a), revealing that the L and X valleys are of higher energy than the direct gap Γ valley, the transition that dominates the optical behavior of InGaAs as the semiconductor bandgap [7].

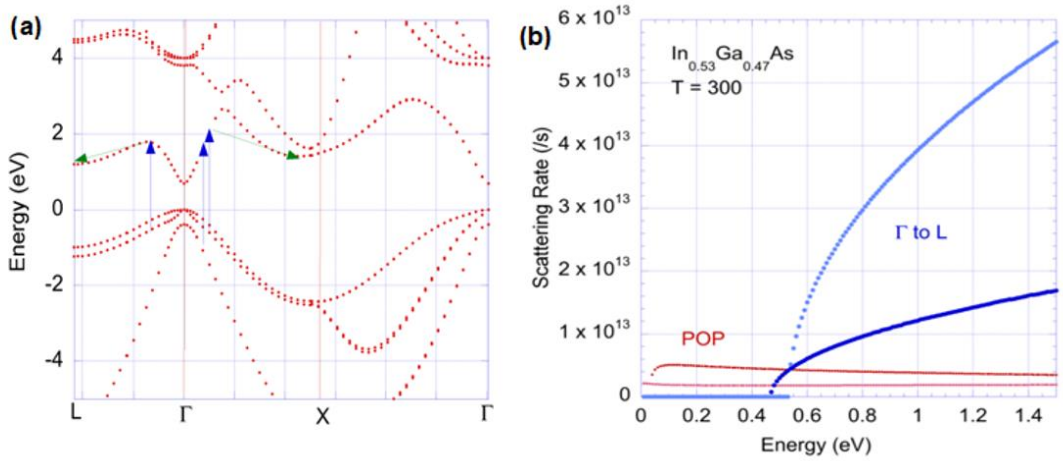

Figure 4. 2. (a) The band structure of InGaAs at room temperature, with symmetry points of the Brouillon zone indicated by L, Γ and X. The blue arrows indicate absorption of high energy photons. The green arrows demonstrate consequently accessible intervalley transitions. (b) Scattering rate calculations of InGaAs at 300 K, for thermalization enabling polar optical phonon transitions in red and for intervalley transitions between Γ and L in blue. [Reproduced from: *Ferry, D. K. "In Search of a True Hot Carrier Solar Cell." Semiconductor Science and Technology 34, no. 4 (2019): 44001.*] [7]

Figure 4.2(b) then illustrates the central mechanism of this hot carrier device, comparing the polar optical phonons scattering rates (associated with the normal

thermalization processes) against the intervalley phonon scattering rates that enable the transition to the upper L valley of the InGaAs conduction band. Due to density of states differences, the return process towards the conduction band edge is substantially less favorable [7]. The result is a temporary transfer and storage into the L valley's higher energy states. Zone edge phonons can still enable small scale thermalization losses via transitions between equivalent L valleys (as, unlike the Γ valley, the L valley symmetry positions of the Brouillon zone are plural) but only the intervalley phonon transition back to the Γ valley will allow the carriers to drop below the minimum energy states of the upper valleys [13]. This allows storage of a high energy carrier distribution based on the energy of the upper valley rather than the bandgap, for the timescale of the intervalley transition from L to Γ. This is expected to be sufficient for extraction from the 250 nm absorber layer based on the transport properties of InGaAs [14].

This discussion, while certainly worthy of investigation on its own merits given potential efficiency gains for thermalization mitigation, presumes that high energy carriers will be available. In laboratory conditions, a laser of sufficient photon energy can certainly provide this. But in the context of a proposal for a hot carrier solar cell, it is only a litany of known material properties; a starting point, rather than a functional plan for creating an efficient solar cell. A successful hot carrier solar cell would feature reasonable photocurrent and *enhanced* photovoltage (in this proposal, based on the energy of the upper valley). This suggests a twofold need. First, a means for exciting lower energy carriers provided by the solar spectrum towards the upper valley for extraction. Second, to enable the enhanced photovoltage, an energy selective contact that extracts carriers from the upper valley's energy rather than the Γ valley.

To accelerate low energy carriers to the upper valleys, an electric field is capable. This is a known technique in III-V materials since the Gunn Effect [15] was identified in the alteration of effective carrier mass with field strength - indicative of carriers transitioning to upper valleys with different density of states. The doping densities indicated in Figure 4.1 were chosen to provide an internal electric field of substantial magnitude.

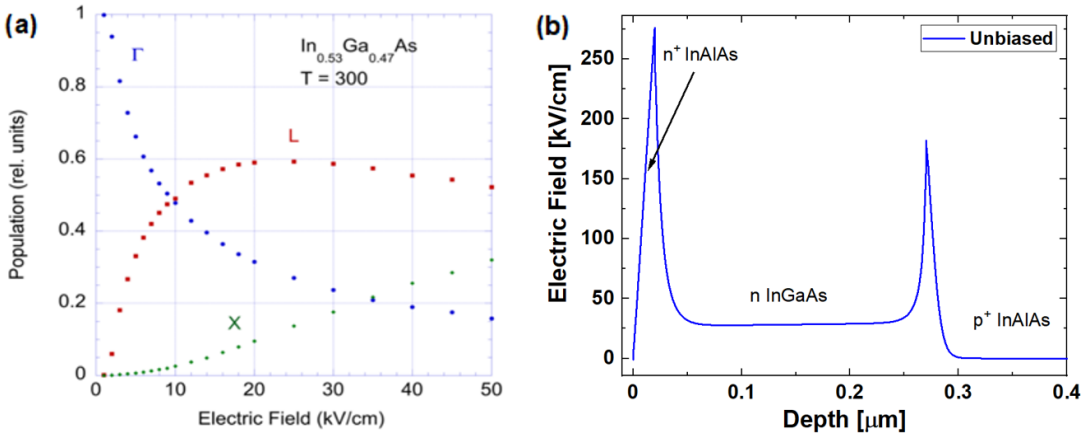

Figure 4. 3. (a) Relative conduction band valley occupancy of InGaAs at room temperature as a function of electric field strength. [Reproduced from: *Ferry, D. K. "In Search of a True Hot Carrier Solar Cell." Semiconductor Science and Technology 34, no. 4 (2019): 44001.*] [7] (b) NRL MultiBands ® simulation of electric field strength at 0 V applied bias for the proof-of-concept structure, as specified in Figure 4.1, as a function of depth from the top (n^+) surface of the device stack.

Figure 4.3(a) shows calculations for a 250 nm InGaAs material's relative valley occupancy as a function of field strength, while the electric field produced by the doping profile is simulated in 4.3(b) through NRL MultiBands ®. The electrical field in the device (~28 kV/cm away from the interface at 0 V external bias) ought to be sufficient

to meaningfully supplement the occupancy of the L valley. This serves as a practical way of mitigating photocurrent losses due to extracting from the upper valley.

There are a range of possibilities to explore in regards to the doping profile beyond the structure chosen for this initial study. The primary limitation to note for further field enhancement by the simple method of doping the n^+ and p^+ layers more heavily is the issue of very highly doped layers behaving as metallic rather than semiconducting, which presents an upper limit for the doping density if the device is to operate by the proposed solar cell mechanisms. But especially with the control over doping density provided by calibrated Molecular Beam Epitaxy, it may be possible (and plausibly more optimal) to grade the doping profile in the absorber layer to provide a better spatial extension of the high field region rather than the current sharp interface spikes. Nevertheless, a field is now present in the sample, and the efficacy of the Gunn Effect-like scattering can be experimentally tested.

In regards to driving the device to operate at higher photovoltage, the energy selective contact mentioned previously is in this device the upper n^+ $In_{0.52}Al_{0.48}As$ layer. As the NRL MultiBands ® 8 band k·p solver simulation below in Figure 4.4 illustrates, there is a potential offset between the Γ valleys of the absorber and n^+ layers. This potential barrier will inhibit extraction via the conduction band edge. The possibility for it to serve as a reasonable energy selective contact at the L valley also exists, given the energy alignment of the L valley of InGaAs and the Γ valley of the top InAlAs layer. Figure 4.4 also reveals a barrier to hole extraction in the back absorber interface; the device is not *optimized*, but being fully lattice matched it could be grown with high quality and examined with available laser wavelengths, photoluminescence and current density-

voltage measurements to probe the prospective hot carrier behavior based on both the electric field acceleration and the intervalley phonon scattering mechanisms.

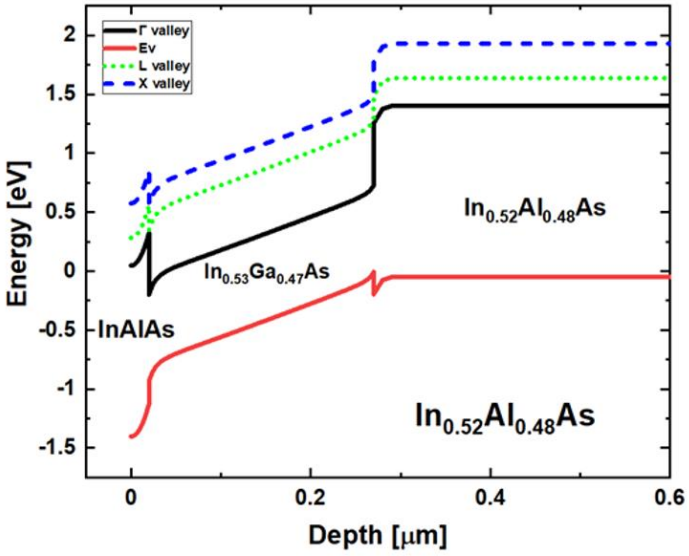

Figure 4. 4. NRL MultiBands ® simulation of the InGaAs heterostructure described in Figure 4.1. [Reproduced from: *Esmaielpour, Hamidreza, et al. "Exploiting Intervalley Scattering to Harness Hot Carriers in III–V Solar Cells." Nature Energy 5, no. 4 (2020): 336-43.*] [8]

The resultant device was fabricated from the grown wafer by standard photolithographic techniques to prepare for contact deposition. Through thermal evaporation, the back contact was 10 nm Ni and then 120 nm AuGe alloy (88% Au, 12% Ge by weight) and the top contact was 120 nm In followed by 30 nm Au. The contacts were finalized by rapid thermal annealing at 300 ℃ for 60 seconds.

4.3. Assessing Valley Photovoltaic Mechanisms via Photoluminescence Spectroscopy

Power dependent photoluminescence was performed with two laser wavelengths: a 442 nm laser that provided sufficient photon energy to enable intervalley phonon scattering, and a 1064 nm infrared laser that excited above the band gap, but below the L valley of the InGaAs absorber (hence, only able to reach the L valley via electric field acceleration). Room temperature data is presented in Figure 4.5 below. The natural logarithm of the photoluminescence provides insight into the carriers in the Γ valley – due to the low momentum nature of photons, recombination to produce the photons recorded in the photoluminescence spectrum is overwhelmingly dominated by the direct gap transitions, and this technique therefore probes the Γ valley distribution as affected indirectly by any intervalley behavior, rather than the upper valleys directly. It can be observed for both laser wavelengths that the spectra diverge from the Gaussian peak standard for a non-hot carrier single bandgap feature.

Analysis of the spectra to extract a hot carrier temperature is therefore a reasonable next step. As the high energy tail of the device is extended, the slope of the natural logarithm in that region may be fit to the generalized Planck relation for a reasonably accurate assessment of the Γ valley carrier distribution in a bulk material [16], assigning a hot carrier temperature that usefully describes the energy enhancement. The results of the analysis (presented as difference from lattice temperature, in this case 300 K) are shown in Figure 4.6.

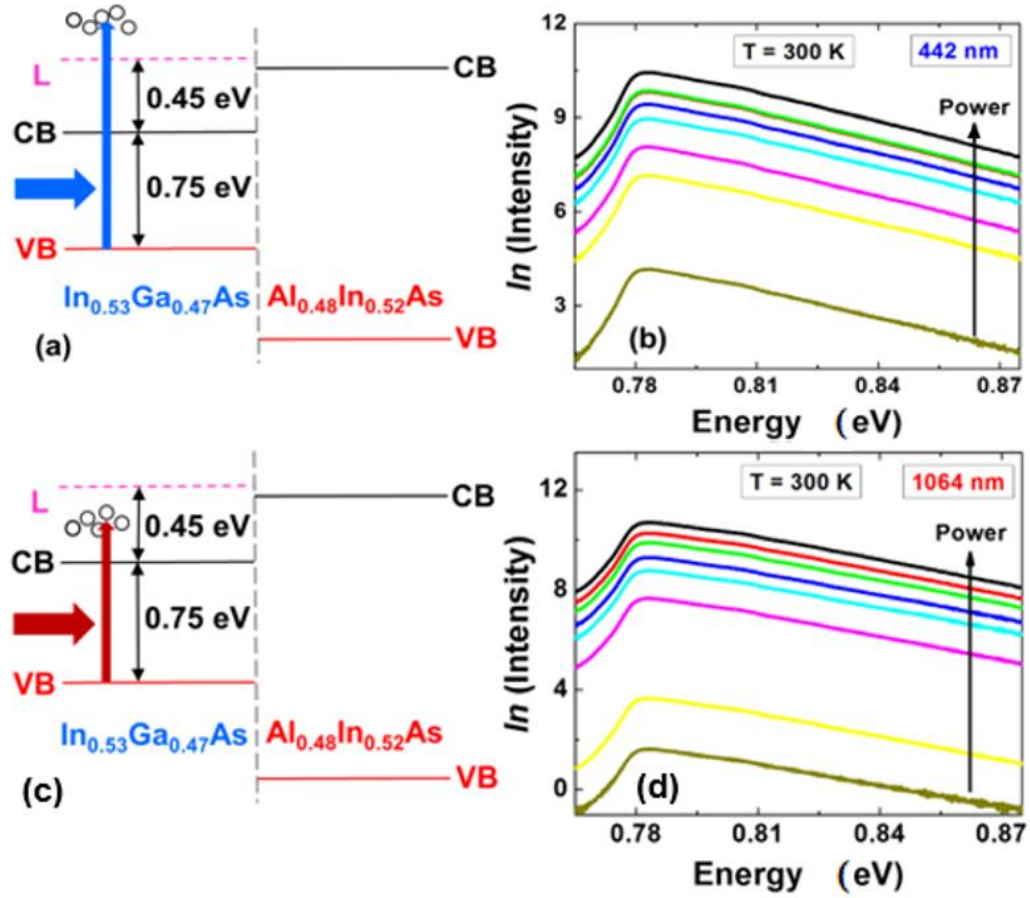

Figure 4. 5. Schematic of carriers excited by (a) 442 nm and (d) 1064 nm photons respective to the energy levels of the top interface of the device. (b) Natural logarithm of the photoluminescence spectrum at room temperature as a function of illumination power for 442 nm (b) and 1064 nm (e) laser light. [Reproduced from: *Esmaielpour, Hamidreza, et al. "Exploiting Intervalley Scattering to Harness Hot Carriers in III–V Solar Cells." Nature Energy 5, no. 4 (2020): 336-43.*] [8]

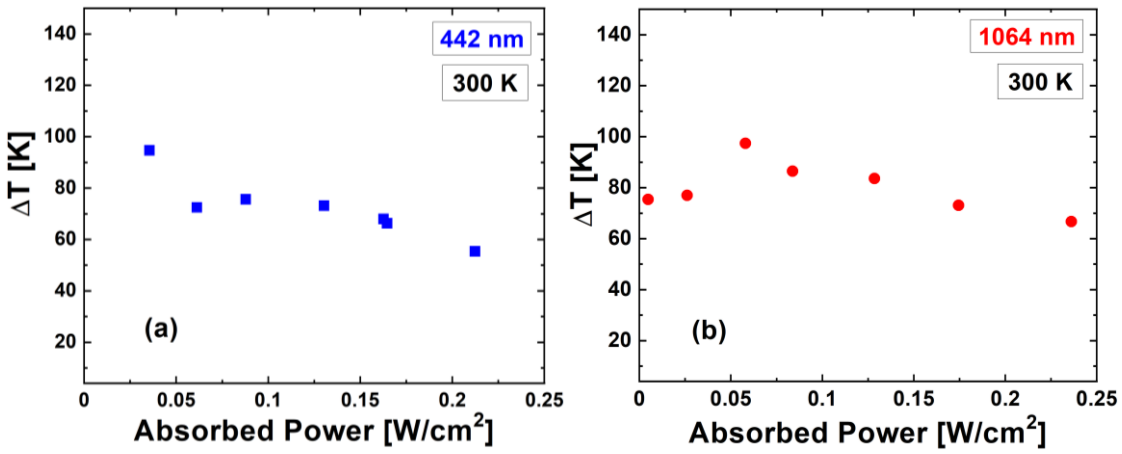

Figure 4. 6. Analysis of hot carrier temperature as difference from lattice temperature as a function of absorbed power density for the photoluminescence spectra in Figure 4.5 for the (a) 442 nm wavelength and (b) 1064 nm wavelength light.

The first point to emphasize is that a non-zero ΔT is an immediate indication of hot carrier behavior. The Γ valley distribution is at heightened energy. This carrier temperature does not serve well to accurately help predict the potential enhanced output of the solar cell, however, as that will depend on the efficacy of the energy selective contact and the precise temperature of the upper valley's carrier distribution. What the ~70 K ΔT in both illumination cases indicates, however, is that the processes driving the detectable hot carrier behavior are performing very similarly.

To reiterate, the 442 nm wavelength photons are fully expected to result in intervalley behavior due to the material properties of the InGaAs absorber, but the 1064 nm wavelength case cannot rely on intervalley phonon scattering due to the photo generation of lower energy carriers. This suggests that the electric field acceleration is functional and, importantly, many carriers are transferred to the *same* upper valley location as the

intervalley phonons scattering [8]. If the carriers were stored at higher or lower energy, then return processes injecting detectable energy into the carrier distribution in the Γ valley would reasonably be anticipated to provide different ΔT. This is promising for the valley photovoltaic hot carrier solar cell design, as if storage in the L valley is favored by both processes, then extraction from the L valley can provide the desired level of photocurrent in addition to the enhanced photovoltage of the upper valley carrier distribution.

A few additional points should be highlighted before moving onward. First, the hot carrier temperatures shown in Figure 4.6 are comparatively low, and as previously noted, not representative of the distribution in the upper valleys. Calculations for hot carrier temperatures of the L and X valleys of InGaAs [7] indicate substantially higher ΔT, and appear consistent with the measurements presented in this thesis. Second, it must be emphasized that all of the photoluminescence measurements are firmly within the low power regime compared to concurrent examples of the phonon bottleneck in the scientific literature [4, 5, 6]. To reiterate, the phonon bottleneck mechanism for maintaining hot carrier behavior is strongly power dependent, and ultimately becomes inoperable in the low power regime. Thereby, these photoluminescence measurements are strong confirmation that the data presented here is not simply a result of both laser wavelengths activating a phonon bottleneck mechanism. In addition, such would be expected to result in different temperatures for difference photon energies, which is not observed.

Lastly, the absorbed powers in Figure 4.6 are calculated from measured illumination power based on laser spot size and transfer matrix calculations of the absorptivity. This

was checked against external quantum efficiency measurements, the results of which are presented in Figure 4.7 below.

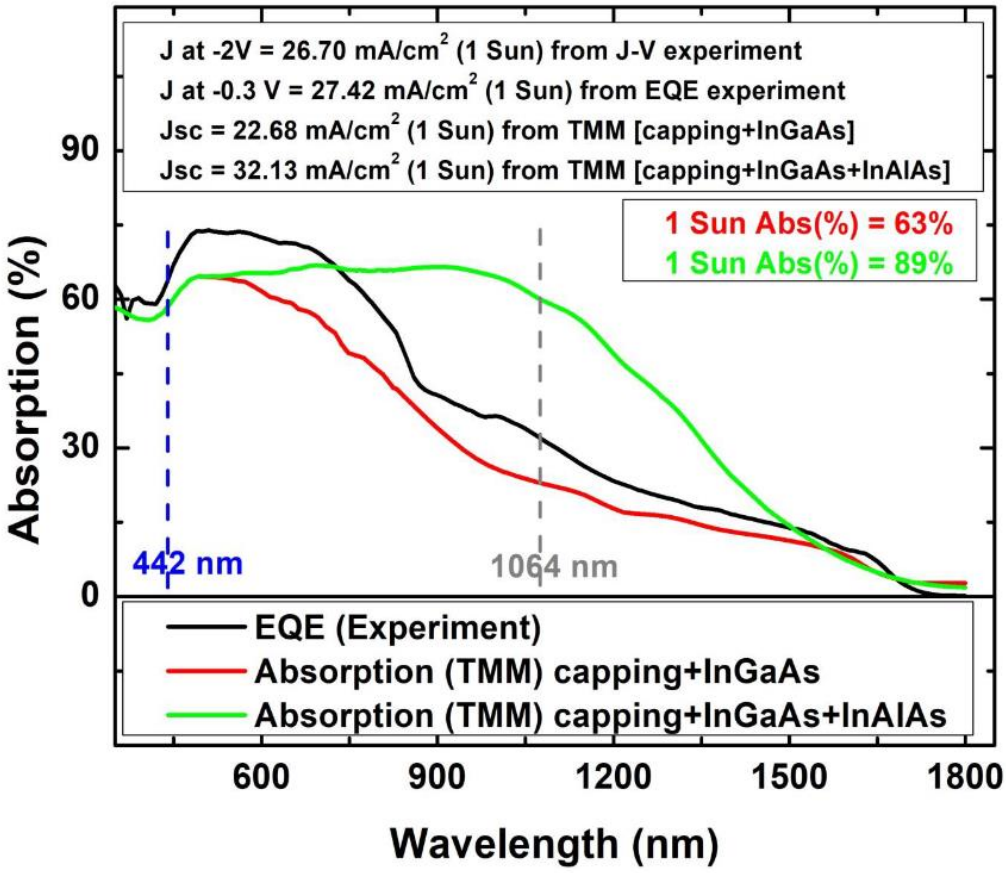

Figure 4. 7. Absorption of the InGaAs device as a function of wavelength, with the 1000 nm p^+ InAlAs layer back layer included in green and excluded in red. The external quantum efficiency measurement (in black) is more consistent with the truncated absorption calculation, as is J_{sc} analysis. [Reproduced from: *Esmaielpour, Hamidreza, et al. "Exploiting Intervalley Scattering to Harness Hot Carriers in III–V Solar Cells." Nature Energy 5, no. 4 (2020): 336-43.*] [8]

The behavior of the device, as indicated by the external quantum efficiency at -0.3 V shown in black in Figure 4.7, is well matched to the calculation for the device through the InGaAs absorber. While the absorber is relatively thin at 250 nm, the EQE indicates absorption by deeper layers do not dominate the device's electrical characteristics. The absorbed lower energy photons further into the device stack are not extracted. However, the higher experimentally measured EQE also suggests that some higher energy carriers absorbed in the InGaAs are also being collected (with reverse bias) perhaps providing some indication that carriers are being collected which typically result in thermalization losses in this structure. For a hot carrier device, this is a desirable property. The reverse bias current density under 1 Sun illumination is consistent with the predicted *Jsc* from convoluting the absorption with the solar spectrum, supporting the claim that the device is high quality. The electronic behavior must be discussed in further depth, as there is some complexity involved, not all of which is immediately beneficial.

4.4. Current Density-Voltage Measurements

Figure 4.8 presents current density-voltage (*J-V*) measurements under 1 Sun AM1.5G solar irradiation as a function of temperature. As can be observed, the fourth (solar cell) quadrant of the *J-V* characteristic is depreciated [8]. First, as compared to the ideal square shape that would provide the most output power for a given short circuit current density (*Jsc*) and open circuit voltage (*Voc*), but also the *Jsc* and *Voc* are below expectations considering conventional photovoltaic behavior. In regards to the photocurrent, while the reverse bias current density is excellent (and the room temperature data used in Figure 4.7 for comparison to the transfer matrix calculations and external quantum efficiency measurements) there is an inflection in the *J-V* characteristic that severely inhibits solar

cell performance. This is indicative of a barrier to minority carrier extraction, and can plausibly be linked to a combination of the potential barrier to extraction via the conduction band edge at the top interface shown in Figure 4.4 (supported by the shift in the inflection with temperature) and the density of states differences between the Γ of the n^+ InAlAs and the L valley of the absorber, similar to the restriction on return from L to Γ within the absorber that supports storage of carriers in the upper valley.

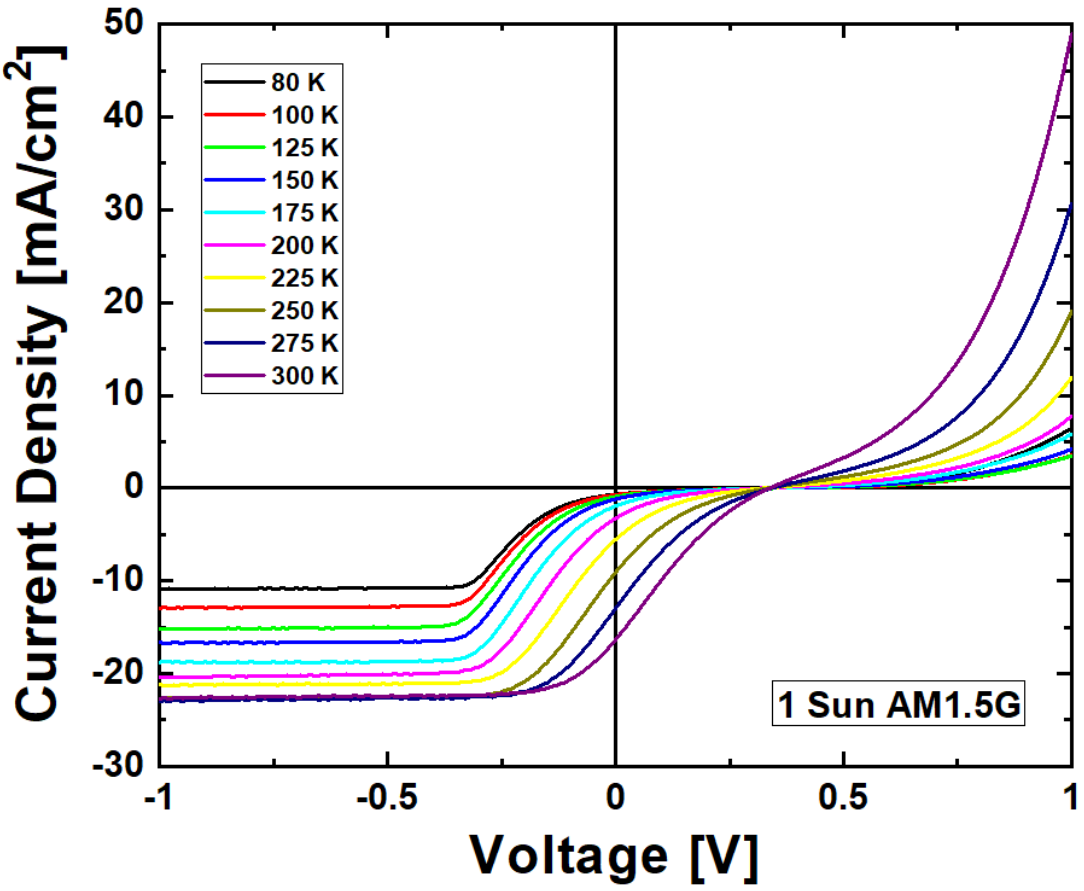

Figure 4. 8. Temperature dependent current density-voltage measurements under 1 Sun AM1.5G illumination as a function of temperature.

The open circuit voltage is a more immediate concern, as improvements to the energy selective contact might enhance photocurrent, but it is necessary for analysis of this device as a potential hot carrier solar cell to determine whether the poor photovoltage is a consequence of the weak extraction or a more intractable problem. The bandgap of InGaAs is ~ 0.75 eV, while the L valley is ~ 0.5 eV higher in energy. If carriers are extracted at that enhanced energy, an achievable photovoltage based on the valley energy would therefore hopefully be approximately ~1.25 eV. This would be mitigated by other semiconductor layers and contacts, and given the presence of hot carrier behavior might be further enhanced depending on the illumination and structural details of the device. The *Voc* of this proof-of-concept device is well below the bandgap of InGaAs at all temperatures, leaving little doubt that the poor carrier extraction has depreciated the *Voc*. What must be determined is by how much – is there evidence that the device could operate at a higher photovoltage were the extraction improved?

Figure 4.9 illustrates monochromatic *J-V* measurements, once more with the above and below valley laser energies, taken in conjunction with the previously presented photoluminescence spectra. A linear fit to the *J-V* curve above 1.5 V forward bias returns a similar turn-on voltage in both cases of ~1.375 V [8]. This estimation is clearly enhanced beyond expectation for a InGaAs absorber device, though the potential error in such a projection limits the confidence with which it might be claimed that this system could potentially exceed the proposed 1.25 eV photovoltage, though the possible influence of the higher energy X valley and the previously discussed potential for hot carrier enhancement above the L valley energy do not make such a voltage implausible.

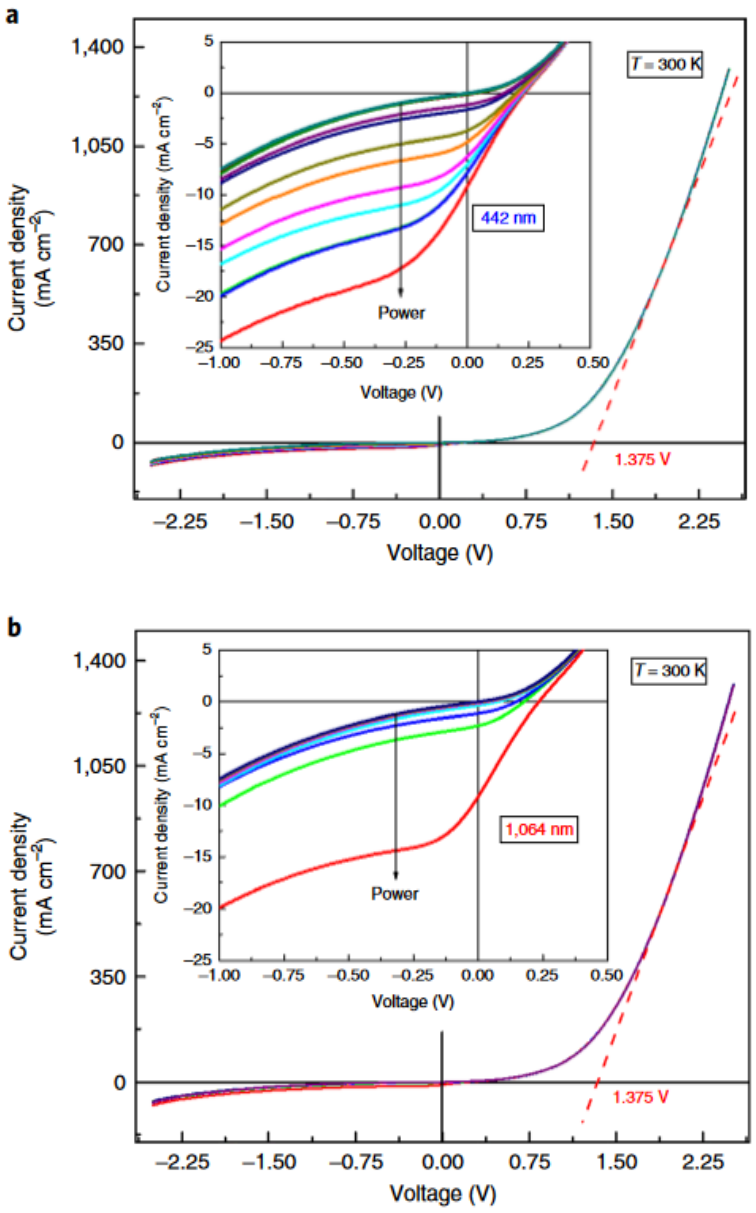

Figure 4. 9. Power dependent current density-voltage data for the InGaAs absorber device at room temperature under (a) 442 nm and (b) 1064 nm wavelength illumination. Presented curves are power matched to the 442 nm data, so as not to give the inaccurate impression that the 1064 nm wavelength results in better extraction. [Reproduced from: *Esmaielpour, Hamidreza, et al. "Exploiting Intervalley Scattering to Harness Hot Carriers in III–V Solar Cells." Nature Energy 5, no. 4 (2020): 336-43.*] [8]

While this does not improve the proof-of-concept device's practical solar cell performance, it indicates the potential of optimized next generation valley photovoltaic structures, as the depreciation of the photovoltage can likely be countered in future designs with better current extraction.

It is also promising to note that the power matched *J-V* data in Figure 4.9 is strikingly similar for both above and below upper valley photon energies. The simplest explanation for this is that the carriers face *the same barriers to extraction*, which would not be the case were this behavior driven by the potential offset at the AlInAs/InGaAs heterointerface, and when this is taken in combination with similar hot carrier behavior under both laser wavelengths it strengthens the claim that the carriers are being stored in the same manner in the upper valley. The structure is simple, and this behavior is robust, and thus future devices can rely on these mechanisms to support the hot carrier behavior.

4.5. Bias Dependent Measurements

To further investigate the electric field acceleration mechanism for exciting low energy carriers to the upper valleys, a suite of applied biases across the regimes of the current density-voltage curves were examined. While the interface spikes of the field strength were very strong, as seen in Figure 4.3(b), the field across the bulk of the absorber as constructed by the doping density contrast is weak enough that applying an external bias could have substantial effects on the operation of the device. Of perhaps most importance is the question of applied forward bias, as while the prospect of operating this proof-of-concept device at its maximum power point is not impressive given the limited solar cell quadrant seen in Figure 4.8 and Figure 4.9, in future work this will become of increasing

relevance. A valley photovoltaic solar cell in full operation, especially given the desired enhanced *Voc*, would operate under notable external forward bias to extract as much power as possible.

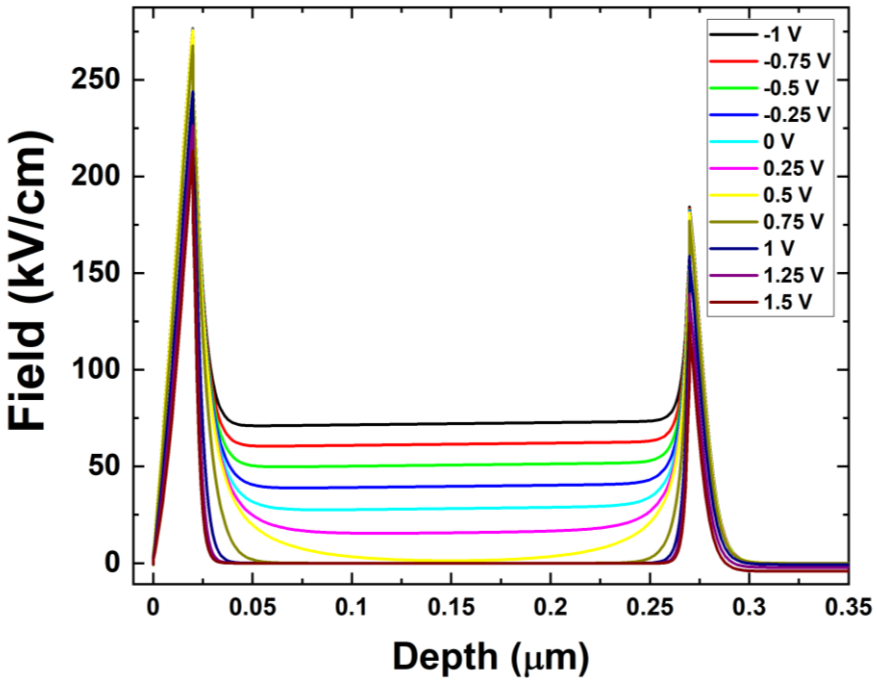

Figure 4. 10. NRL MultiBands ® calculations for the electric field strength as a function of depth at various external applied biases for the proof-of-concept structure (Figure 4.1).

An applied reverse bias strengthens the present fields, while forward bias can be observed in Figure 4.10 to weaken them. Forward bias does not eliminate the interfacial fields within the regime of applied biases that the solar cell might be expected to operate within, but the extent of the field throughout the rest of the absorber becomes increasingly limited. A more advanced version of this structure might have a maximum power point with a voltage between + 0.75 V and + 1.25 V, though in examining the

device in its current form, this is well into the realm of majority carrier extraction. An examination of the photoluminescence under bias is called for, to find the capabilities and limitations of the electric field acceleration for the current doping profile.

Keeping applied bias constant, a further set of power dependent photoluminescence measurements were performed at room temperature with both above and below valley energy illumination. Examination of the behavior in each quadrant through which the current density-voltage characteristic passes inform both of the electric field dependence of the subtler differences in the photoluminescence spectra across the three regimes of electronic behavior is worthy of discussion, and hence Figure 4.11, Figure 4.12, and Figure 4.13 below are presented to assess these conditions.

Most central to the inciting question is the case of applied bias beyond both the *Voc* and the estimated turn-on voltage. Figure 4.11 features extracted carrier temperatures for the InGaAs heterostructure under high forward bias of +1.5 V, the regime of majority carrier extraction. For purposes of enabling comparison between the datasets, the data for the two lasers are presented with only the 1064 nm data that is power matched to the lower intensity 442 nm wavelength laser, based on reverse bias saturation current density. This is the reason for the mismatch in the number of data points presented for each wavelength. There is substantial recombination in this regime, providing clear photoluminescence spectra above thermal noise even at room temperature and low illumination power.

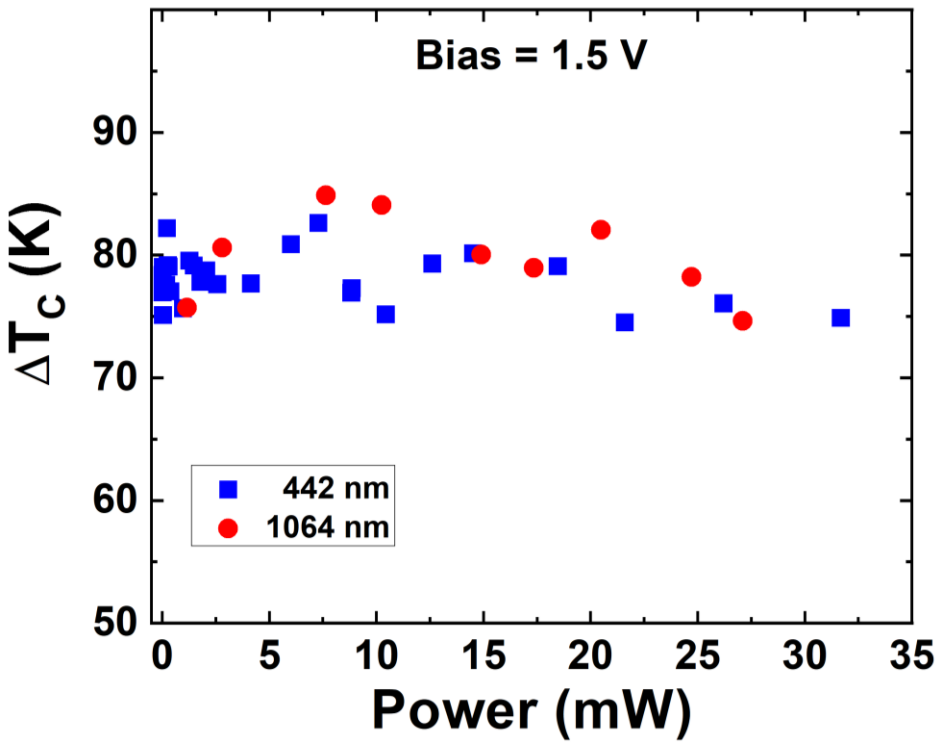

Figure 4. 11. Power dependent carrier temperatures as difference from lattice temperature ΔT at fixed + 1.5 V applied bias, from photoluminescence spectra taken at 300 K, comparing at matched power between 442 nm (blue squares) and 1064 nm (red circles) laser wavelengths. [Reproduced from: Esmaielpour, Hamidreza, et al. "Exploiting Intervalley Scattering to Harness Hot Carriers in III–V Solar Cells." Nature Energy 5, no. 4 (2020): 336-43.] [8]

Aside from the interfacial spikes, there is negligible field to excite carriers from the band edge to the upper valleys at high forward bias, as seen in Figure 4.10, with the field strength become localized within ~20 nm of the interface rather than extending across the absorber as shown in Figure 4.3(b). Nevertheless, the carrier temperatures are essentially consistent with prior unbiased photoluminescence analysis, an especially

notable outcome for the 1064 nm wavelength illumination. For the result to be comparable both to the 442 nm wavelength data in Figure 4.11, but to the results in Figure 4.6(b) indicates that the electric field acceleration is not deactivated as a mechanism for carriers to reach the upper valley.

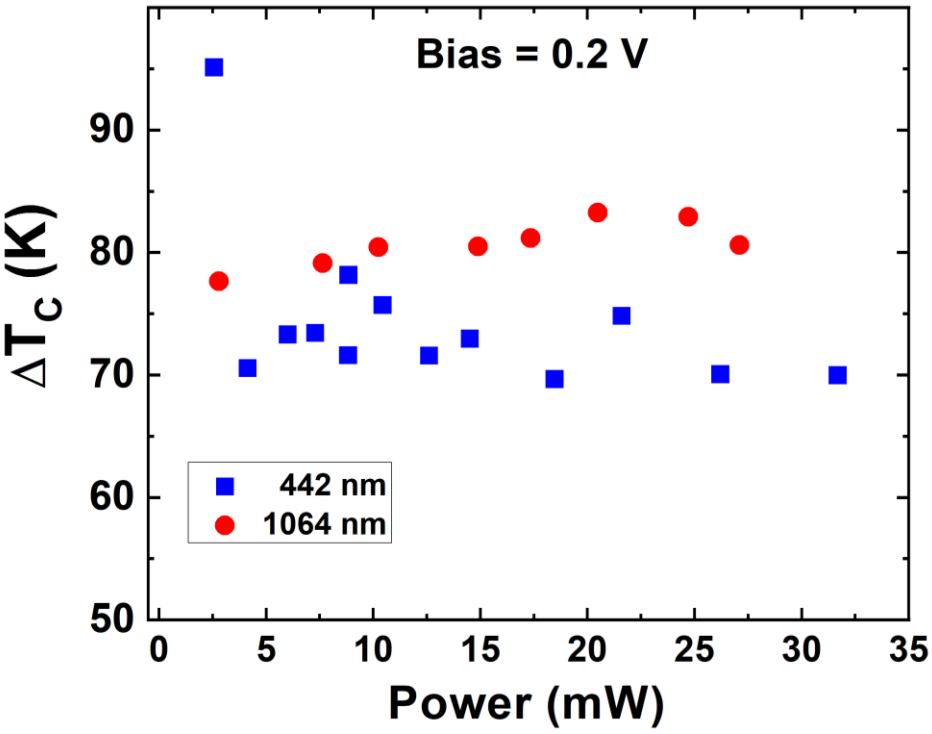

Figure 4. 12. Power dependent carrier temperatures as difference from lattice temperature ΔT at fixed + 0.2 V applied bias, from photoluminescence spectra taken at 300 K, comparing at matched power between 442 nm (blue squares) and 1064 nm (red circles) laser wavelengths. [Reproduced from: Esmaielpour, Hamidreza, et al. "Exploiting Intervalley Scattering to Harness Hot Carriers in III–V Solar Cells." Nature Energy 5, no. 4 (2020): 336-43.] [8]

Within the fourth quadrant of the current density-voltage characteristic, which was achieved with a + 0.2 V applied bias as seen in the carrier temperature analysis in Figure 4.12, the device is in the desired operational regime as a solar cell, albeit limited by the extraction mechanism as previously discussed. As shown in Figure 4.4, the only valley transition between n^+ InAlAs and the InGaAs absorber without a substantial (200 meV or greater) potential offset is the L-to-Γ alignment. This is an inefficient transition due to the difference in density-of-states between the L of the absorber and Γ valley of the top barrier layer.

At + 0.2 V applied bias, the electric field produced by the doping profile is not extinguished across the absorber thickness. Figure 4.10 suggests the field could be well in excess of the minimal 10 kV/cm for L valley dominance predicted by the calculations shown in Figure 4.3(a), and as anticipated with the electric field driven mechanism active, the two laser energies both result in the hot carrier behavior shown in Figure 4.12. The 1064 nm data case now appears to result in a slightly higher carrier temperature, though rather remaining close to the 442 nm data in an absolute sense. The power dependence is, once more, approximately independent across the range of illumination power in this study. Although it must again be emphasized that a future valley photovoltaic device may require substantially higher operating voltage, the consistency of this result and the robustness of the hot carrier behavior at the operating voltage of this admittedly inefficient version of the concept is a hopeful sign indeed.

The photovoltaic regime does not have external field applied to aid minority carrier extraction, and the extraction is depreciated by the inflection seen in the monochromatic current density-voltage data of Figure 4.9. Figure 4.12 reveals that the

photoluminescence intensity (and hence photon emission via recombination) remains relatively strong, though thermal noise is a limitation below ~2.5 mW absolute illumination power, below which errors rapidly accumulate in the analysis of the hot carrier temperature. This provides a useful moment to elaborate on a concern that a scrupulous observer might possess. Setting aside that these measurements are firmly in the low power regime compared to examples of a phonon bottleneck in the literature, how does the estimation of the carrier temperature alter in the low signal data not present in Figure 4.12 or, below, in Figure 4.13? Does it decrease towards the lattice temperature?

The answer is instead the opposite. The carrier temperature for the 442 nm wavelength shown slightly below that power is representative of the error introduced by thermal noise when the signal to noise ratio becomes problematic: the estimation of the carrier temperature increases in a clearly unphysical manner, and plotting abrupt increases in temperature of 100 K or more would neither be usefully representative nor aid analysis of the rest of the data points.

In reverse bias, chosen at - 0.3 V applied bias as presented in Figure 4.13, the minority carrier extraction is enhanced. The presence of the inflection renders this a more dramatic enhancement than expected of a high-quality solar cell, and it is with an eye to the bias at which the inflection (and, presumably, relevant barriers to extraction) are surpassed in the 1 Sun AM 1.5G *J-V* characteristic in Figure 4.8 that - 0.3 V bias was chosen for closer investigation. Figure 4.13 has fewer data points, because photoluminescence intensity under these conditions is weaker as extracted carriers do not recombine to produce photons [17]. As discussed previously in the context of the EQE and Figure 4.7, the

reverse bias saturation current density under 1 Sun AM 1.5G is at least comparable to theoretically calculated values, indicative of the excellent quality of the device. While a pleasing result from an electronic perspective, this limits the data points for the power dependent photoluminescence at this bias, as Figure 4.13 reveals.

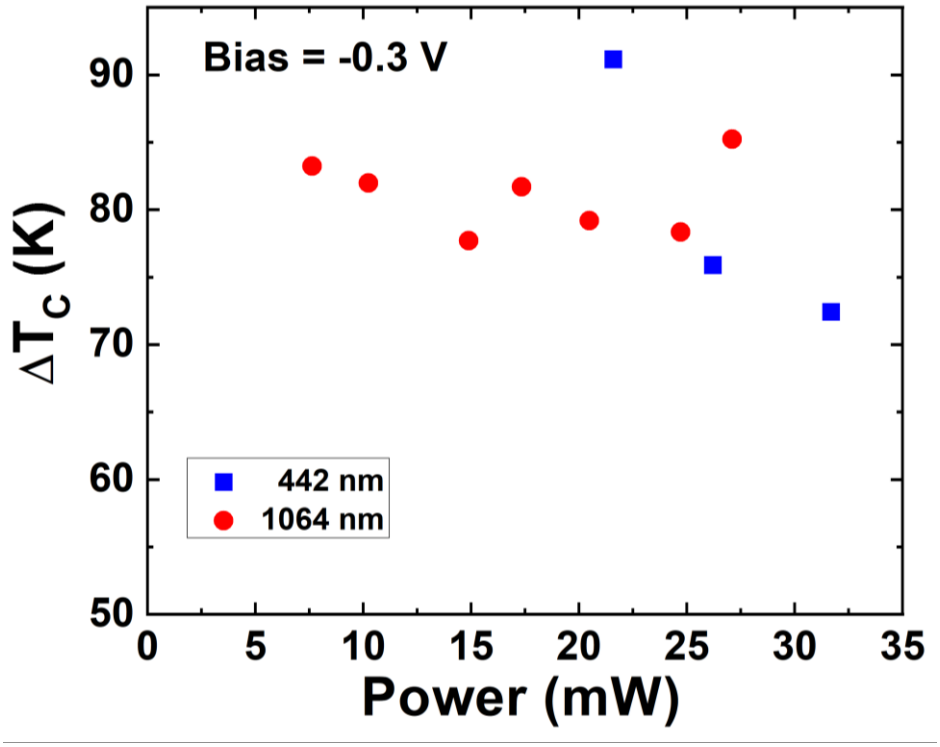

Figure 4. 13. Power dependent carrier temperatures as difference from lattice temperature ΔT at fixed - 0.3 V applied bias, from photoluminescence spectra taken at 300 K, comparing at matched power between 442 nm (blue squares) and 1064 nm (red circles) laser wavelengths. [Reproduced from: Esmaielpour, Hamidreza, et al. "Exploiting Intervalley Scattering to Harness Hot Carriers in III–V Solar Cells." Nature Energy 5, no. 4 (2020): 336-43.] [8]

Once again, hot carrier behavior is observed, though the 442 nm wavelength laser is less able to demonstrate the power independence of its infrared counterpart due to a weaker photoluminescence intensity (due to the lower power of this laser). That the 1064 nm wavelength illumination data indicates strong hot carrier behavior when under applied bias that enhances the electric field strength is consistent with the predictions of the valley photovoltaic model. Indeed, it is worthwhile to observe that across all measurements presented in this chapter, the carrier temperatures under both lasers remain similar to each other, and to a relatively fixed ~70 K temperature [8]. Given the variation of the external factors in these measurements, the preposition that the hot carrier behavior is supported by a stable material property of the absorber (the L valley energy) appears to be a well-supported interpretation at this stage.

To further inform this part of the study, a wider set of biases were applied to gain a better grasp of carrier temperature dependencies on the electric field strength within the likely operational voltage range of this device. The results presented in Figure 4.14 below are bias dependent photoluminescence measurements at room temperature and matched illumination power between the 442 nm and 1064 nm lasers. The difference from lattice temperature for each case is plotted alongside 1 Sun AM 1.5G room temperature current density-voltage data to make clear how the applied biases relate to the electronic behavior of the sample.

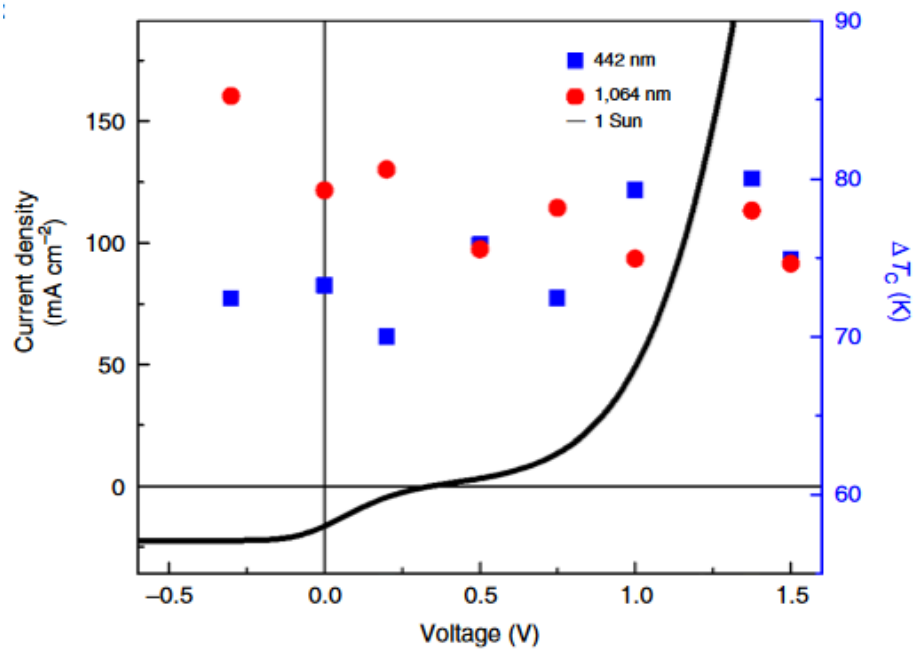

Figure 4. 14. The 1 Sun AM 1.5G current density-voltage data is shown in the black curve, while bias dependent carrier temperatures extracted from the photoluminescence spectra (at 300 K, comparing at matched absorbed power) for 442 nm (blue squares) and 1064 nm (red circles) are presented at the applied biases. [Reproduced from: Esmaielpour, Hamidreza, et al. "Exploiting Intervalley Scattering to Harness Hot Carriers in III–V Solar Cells." Nature Energy 5, no. 4 (2020): 336-43.] [8]

It might be suggested that the 1064 nm wavelength excitation data is at slightly enhanced temperature as the bias steps towards the reverse and the electric fields strengthen, which would be consistent with results from subsequent studies, discussed in later chapters of this thesis. However, the overall conclusion to be drawn from this data is there is not a *strong* trend across the range of applied biases, especially for the 442 nm wavelength excitation data.

Certainly, and most relevantly, this reiterates what is also demonstrated in Figure 4.11: the hot carrier behavior *is evident* even at large forward bias for the 1064 nm wavelength excitation case, where the electric field in the bulk absorber is negligible. As Figure 4.10 demonstrates, at high forward bias the electric field across the width of the InGaAs absorber layer rapidly approaches zero, leaving only the strong but highly localized fields at the interfaces with the absorber to be responsible for acceleration to higher valleys. That the hot carrier behavior is present under 1064 nm wavelength light and + 1.5 V applied bias was not a given from the relative valley population as a function of field strength calculations in Figure 4.3(a), as that presumed an acceleration could continue over the 250 nm absorber thickness. The ~20 kV/cm across the bulk of 0 V bias InGaAs sufficed, but the applicability of that simulation to a very large (>100 kV/cm) field over a very small (< 5 nm) region [8] could not be relied upon. This result indicates that the high field region suffices for acceleration to the upper valleys, and furthermore that the excellent transport properties of high quality InGaAs are enabling carrier diffusion across the absorber thickness so that the carriers reach the high field region, subsequently accelerate to the upper valley, and consequently produce the observed hot carrier behavior.

This result exceeded any expectations, although it would have arguably been more useful for proof-of-principle purposes if a reasonably sized forward bias could fully deactivate the Gunn Effect and provide photoluminescence data that ceased hot carrier behavior under 1064 nm wavelength laser light. As it stands, there is very good reason to believe that the long-established Gunn Effect is responsible, and it is well matched to simulations present in the literature. The data is consistent with the proposed

mechanisms. Yet, for applied external field to have a more dramatic effect on the hot carrier behavior than minor modulation of the carrier temperature would be truly explicit confirmation. But the doping density-driven interface fields, due to the very precision that Molecular Beam Epitaxy provides, cannot reasonably be driven to sufficiently low values of applied forward bias, and such a valuable study must be left to future structures better fit for the experiment.

4.6. Conclusions

In this chapter, a proposed set of mechanisms for the creation of a hot carrier device were tested in a bulk InGaAs heterostructure. This valley photovoltaic concept is rooted in long established physical principles of intervalley phonon scattering towards upper valleys from high in the conduction band and electric field driven scattering to the same upper valleys from the conduction band edge. These are combined to novel results in a device that has repeatedly demonstrated genuinely robust hot carrier maintenance at room temperature and under weak illumination intensities, notable weak points in prior demonstrations of hot carrier behavior.

The original concept of the hot carrier solar cell was simply a solar cell that mitigated thermalization, that aimed to exceed the bandgap in photovoltage but fundamentally was still rooted in that primary semiconductor property. The efforts of the scientific community have certainly resulted in promising steps towards that end. Yet, to surpass the single gap limit, the proposal put forward here is that the bandgap is not inherently required to drive the electronic properties of a solar cell. The valley photovoltaic proposal is, succinctly, that the device may operate *optically* based upon the bandgap of the

absorber, but *electronically* an upper valley of the broader band structure might serve to be the limit of the photovoltage. That what determines the transmission losses and what determines thermalization losses need not be the single gap, that it is possible to decouple them and thereby challenge long understood limits of solar cell efficiency.

While the results of this study have not achieved the long-sought goal of surpassing the single gap efficiency limit, this study provides proof of principle operation of the valley photovoltaic protocol and a starting point for future work. The proof-of-concept device accomplishes hot carrier maintenance at the first foray into the novel design space of intervalley photovoltaics, but the carrier extraction remains a critical issue to be resolved. The current device is half of the hot carrier solar cell puzzle, and the success of it is not finalized without enhanced photovoltage. Future designs must iterate, master the question of an effective energy selective contact for a device operating on intervalley mechanisms, and then begin the work of optimization. And the rewards for doing so, given the well-established materials and simple structures that have accomplished this first step, could not only be theoretically immense, but also practical to implement with already extant industrial capacity.

References

[1] Ross, Robert T., and Arthur J. Nozik. "Efficiency of Hot-carrier Solar Energy Converters." *Journal of Applied Physics* 53, no. 5 (1982): 3813-818.

[2] Shockley, William, and Hans J. Queisser. "Detailed Balance Limit of Efficiency of p-n Junction Solar Cells." *Journal of Applied Physics* 32, no. 3 (1961): 510-19.

[3] Conibeer, G., N. Ekins-Daukes, J-F. Guillemoles, D. König, E. C. Chou, C-W. Jiang, S. Shrestha and M. A. Green. "Progress on hot carrier solar cells." *Solar Energy Materials & Solar Cells* 93, (2009): 713-719.

[4] Hirst, L. C., R. J. Walters, M. F. Führer, and N. J. Ekins-Daukes. "Experimental Demonstration of Hot-Carrier Photo-Current in an InGaAs Quantum Well Solar Cell." *Applied Physics Letters* 104, no. 23 (2014): 231115.

[5] Nguyen, D.-T., L. Lombez, F. Gibelli, S. Boyer-Richard, A. Le Corre, O. Durant, and J-F. Guillemoles. "Quantitative Experimental Assessment of Hot Carrier-Enhanced Solar Cells at Room Temperature," *Nature Energy* 3, (2018): 236–242.

[6] Rodière, Jean, Laurent Lombez, Alain Le Corre, Olivier Durand, and Jean-François Guillemoles. "Experimental Evidence of Hot Carriers Solar Cell Operation in Multi-Quantum Wells Heterostructures." *Applied Physics Letters* 106, no. 18 (2015): 183901.

[7] Ferry, D. K. "In Search of a True Hot Carrier Solar Cell." *Semiconductor Science and Technology* 34, no. 4 (2019): 44001.

[8] Esmaielpour, Hamidreza, Kyle R. Dorman, David K. Ferry, Tetsuya D. Mishima, Michael B. Santos, Vincent R. Whiteside, and Ian R. Sellers. "Exploiting Intervalley Scattering to Harness Hot Carriers in III–V Solar Cells." *Nature Energy* 5, no. 4 (2020): 336-43.

[9] Guillemoles, Jean-Francois, Thomas Kirchartz, David Cahen, and Uwe Rau. "Guide for the Perplexed to the Shockley–Queisser Model for Solar Cells." *Nature Photonics* 13, no. 8 (2019): 501-05.

[10] Klemens, P. G. "Anharmonic Decay of Optical Phonons." *Physical Review* 148, no. 2 (1966): 845-48.

[11] Esmaielpour, H., V. R. Whiteside, H. P. Piyathilaka, S. Vijeyaragunathan, B. Wang, E. Adcock-Smith, K. P. Roberts, T. D. Mishima, M. B. Santos, A. D. Bristow, and I. R. Sellers. “Enhanced Hot Electron Lifetimes in Quantum Wells with Inhibited Phonon Coupling.” *Scientific Reports* 8, no. 1 (2018): 12473-9.

[12] Murdin, B. N., W. Heiss, C. J. G. M. Langerak, S.-C. Lee, I. Galbraith, G. Strasser, E. Gornik, M. Helm, and C. R. Pidgeon. "Direct Observation of the LO Phonon Bottleneck in Wide GaAs/$Al_XGa_{1-X}As$ Quantum Wells." *Physical Review B: Condensed Matter* 55, no. 8 (1997): 5171-176.

[13] Ferry, D. K., S. M. Goodnick, V. R. Whiteside, and I. R. Sellers. "Challenges, Myths, and Opportunities in Hot Carrier Solar Cells." *Journal of Applied Physics* 128, no. 22 (2020): 220903.

[14] Ferry, David K., Vincent R. Whiteside, and Ian R. Sellers. "Pathways to Hot Carrier Solar Cells." *Journal of Photonics for Energy* 12, no. 2 (2022): 022204.

[15] Gunn, J. B. "Microwave Oscillations of Current in III-V Semiconductors." *Solid State Communications* 88, no. 11 (1993): 883-86.

[16] Gibelli, François, Laurent Lombez, and Jean-François Guillemoles. "Accurate Radiation Temperature and Chemical Potential from Quantitative Photoluminescence Analysis of Hot Carrier Populations." *Journal of Physics. Condensed Matter* 29, no. 6 (2016): 06LT02.

[17] Afshari, Hadi, Brandon K. Durant, Ahmad R. Kirmani, Sergio A. Chacon, John Mahoney, Vincent R. Whiteside, Rebecca A. Scheidt, Matthew C. Beard, Joseph M. Luther, and Ian R. Sellers. "Temperature-Dependent Carrier Extraction and the Effects of Excitons on Emission and Photovoltaic Performance in $Cs_{0.05}FA_{0.79}MA_{0.16}Pb(I_{0.83}Br_{0.17})_3$ Solar Cells." *ACS Applied Materials & Interfaces* 14, no. 39 (2022): 44358-4366.

Chapter 5

Comparative Analysis of InGaAs Valley Photovoltaic Heterostructures with Altered Top Barrier Layers

5.1. Introduction

In recent years, interest in overcoming the single gap limit for solar cells [1] via hot carrier devices that mitigate thermalization losses [2] has transformed from a hypothetical into a burgeoning area of study. While the hot carrier solar cell, as of the writing of this thesis, is yet to exist in a practical form, a substantial and growing body of scientific work has accumulated that provides examples of hot carrier behavior in a variety of devices. While the efforts at our own institution have begun based on the now well-established phonon bottleneck behavior that limits thermalization at the LO to LA phonon interactions [3, 4], unexpected hot carrier temperatures within InAs quantum well structures [5] have led to greater understanding of the possibilities inherent in looking beyond the bandgap for hot carrier maintenance in III-V materials. It is these recent efforts in novel intervalley scattering-based hot carrier devices [6] to which this thesis speaks.

The means to maintain carriers in a robust manner at higher energy using upper satellite valleys in the bandstructure of the absorber are provided by the material properties of III-V systems [7], of which InGaAs absorber structures have to this point been the primary subject of this methodology, both in the prior chapter [6] and in the study presented here

[8]. This is enhanced by the means to accelerate carriers from the conduction band edge to the same upper valleys, for which internal electric fields well serve the purpose [9].

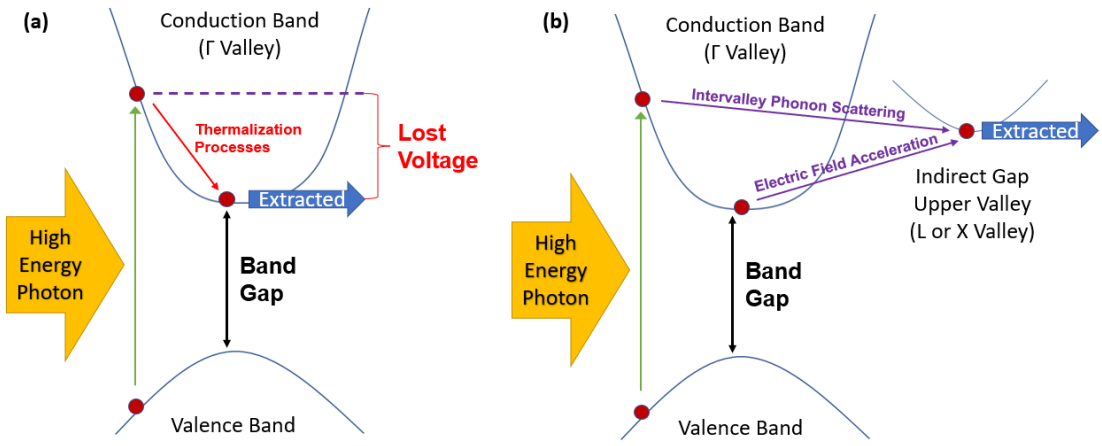

Figure 5. 1. (a) Standard operation of a direct band gap solar cell. The photovoltage is limited by the band gap of the absorber – while above-band gap energy photons are absorbed, the additional energy is lost. (b) Operation of a valley photovoltaic solar cell. Intervalley mechanisms support a stable population of carriers at greater than band gap energy. Extracting from the upper valley enables enhanced photovoltage. [Reproduced from *Dorman, K. R., et al., "Toward Hot Carrier Extraction in Intervalley Photovoltaic Devices." ACS Applied Energy Materials 5, no. 9 (2022): 11159–1166.*] [8]

To reiterate the concept as developed thus far, the valley photovoltaic solar cell would rely upon transfer mechanisms towards valleys (non-bandgap local minima) of the broader band structure of the absorber material. In certain materials, such as III-V crystals like InGaAs, the phonon scattering rates that provide the momentum for these transitions are highly competitive if the carriers have sufficient energy from absorbed

photons. Coupled with sufficient electric field for enhancement of carriers near the bandgap in energy, and this becomes a reliable vehicle for operating a device outside the bandgap electronically, without altering the optical properties of the absorber. The standard operation of a single gap solar cell, suffering from thermalization losses, is illustrated in Figure 5.1(a), while the prospective valley photovoltaic solar cell is presented in Figure 5.1(b).

In the regular operation of a single gap device, a choice of bandgap is a selection between higher thermalization losses or higher transmission losses, as governed by the solar spectrum. The valley photovoltaic solar cell would decouple this relationship, and thus far it has been demonstrated that thermalization mitigation is present in a set of bulk InGaAs heterostructures studied [6,10]. The resultant hot carrier populations therein are present without requiring the high excitation powers that activate a phonon bottleneck, and viable at room temperature. Yet, this does not immediately translate into a fully operational hot carrier solar cell. The proof-of-concept structure does not provide the key outcome illustrated in Figure 5.1: enhancement to photovoltage due to extracting from an upper valley, with loss of photocurrent mitigated by internal electric fields that prevent lower energy carriers remaining trapped at the conduction band edge. The hot carriers must be extracted, or the valley photovoltaic solar cell will remain a proof-of-concept, and to that end the extraction – and of more relevance, the problems as associated with the extraction that must be resolved – are in need of study.

5.2. Device Structures

As presented thus far [6,10], this is the construction for these InGaAs heterostructures: InP substrate, then a back layer of p^+-$In_{0.52}Al_{0.48}As$, the n-$In_{0.53}Ga_{0.47}As$ absorber layer, and finally the top n^+ layer, chosen as $In_{0.52}Al_{0.48}As$ previously. This structure is shown in Figure 5.2(f). InP is as a zincblende substrate of appropriate lattice constant for the InGaAs absorber, and $In_{0.52}Al_{0.48}As$ is also lattice matched and serves appropriately for the most part save for providing a minor barrier to hole extraction when serving as the p^+ region of the device, shown in Figure 5.2(e). InGaAs has the desired phononic properties, favoring intervalley scattering over thermalization as the valley photovoltaic schema requires [7]. Its bandgap is also direct, small enough to match the solar spectrum in absorption (and hence, absorb above bandgap energy photons that can generate hot carriers capable of transfer to upper valleys by phonon processes) rather than face transmission losses, and can be grown with high quality, both by the molecular beam epitaxy techniques available to the University of Oklahoma and by larger scale industrial epitaxy methods such as MOVPE. The doping differential between the layers of the device are the key to provide the strong internal electric fields necessary to finalize the design, enabling acceleration of carriers to upper valleys as well as the regular concerns of facilitating carrier transport in the desired direction.

It is to the top layer of the device that this study turns the majority of the attention. It must serve two purposes: first, as a means of extraction from the upper valley of the absorber, and second as a barrier to extraction via the Γ valley, which in these structures is equivalent to the direct bandgap of the absorber. If the top layer only provides a barrier, then the device will not provide the enhanced photovoltage of the upper valley, and the

current density will be negatively impacted by the potential barrier without gaining any benefit in recompense. Also, if the top layer facilitates extraction from the upper valley, yet fails to provide a barrier, then it would be expected that the device be dominated by standard extraction from the Γ valley, the gains in photovoltage negatively impacted by the lower energy extraction pathway. This second scenario is simple to avoid in principle, easily satisfied by selection of a materials whose bandgap will serve to provide a potential offset in the conduction band that will serve as a barrier between InGaAs and the transition to the barrier material. The construction of a viable extraction pathway from the upper valley is the central focus of this study.

To that end, in this chapter and the associated manuscript [8], four different top n^+ barrier layers are examined and compared to expand understanding of the previously identified extraction limitations, explore the possibilities presented by different upper valley alignments between the top barrier and the absorber, and elucidate the requirements future hot carrier solar cells must adhere to in order to realize above bandgap photovoltage and, ultimately, beyond single gap limit efficiency.

The n-$In_{0.53}Ga_{0.47}As$/p^+-$In_{0.52}Al_{0.48}As$/p-InP layers are maintained to sharpen the relation between the differences in the devices to the top interface. One of these devices, with n^+-$In_{0.52}Al_{0.48}As$ as the top layer, has previously been examined in some length in the previous chapter and the literature [6,10]. The results of NRL Bands ® simulations of the bandgap and upper valley energies are shown below in Figure 5.2 to demonstrate the valley alignments generated by the structural changes to the top of the device.

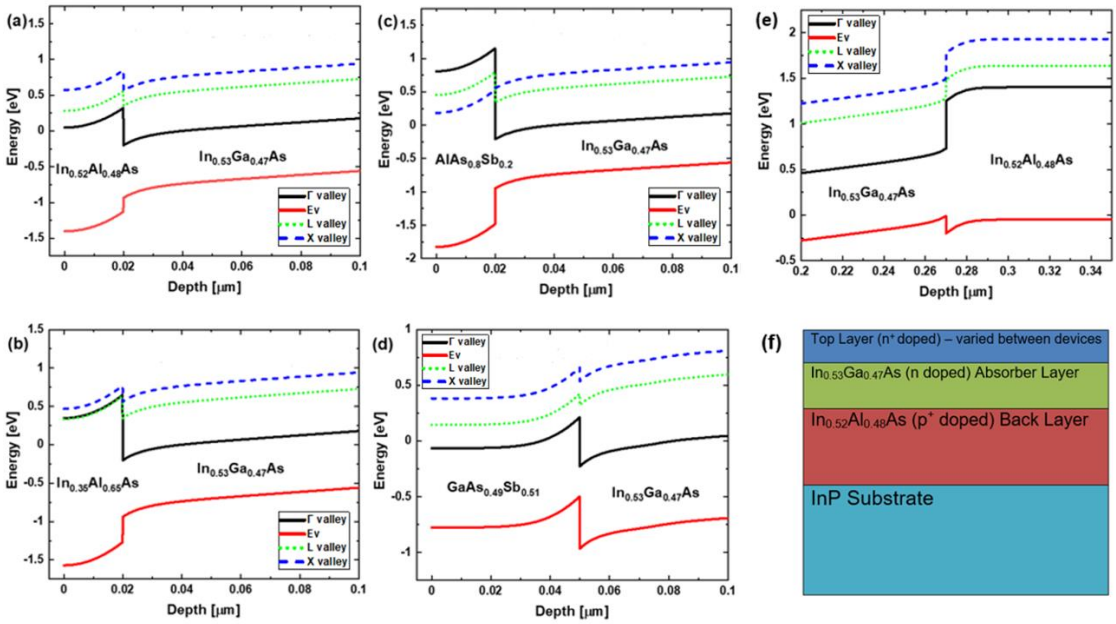

Figure 5. 2. Band calculations for each device, including the energy level of each upper valley, performed in NRL Bands ®. The InGaAs absorber heterostructures feature altered top layers: (a) $In_{0.52}Al_{0.48}As$, (b) $In_{0.35}Al_{0.65}As$, (c) $AlAs_{0.8}Sb_{0.2}$, and (d) $GaAs_{0.49}Sb_{0.51}$. The structural similarities of the devices result in the same back band alignment of n-$In_{0.53}Ga_{0.47}As$/p^+-$In_{-.52}Al_{0.48}As$ in all cases. This alignment is illustrated in (e). (f) A simple structural illustration for the full devices. [Reproduced from *Dorman, K. R., et al., "Toward Hot Carrier Extraction in Intervalley Photovoltaic Devices." ACS Applied Energy Materials 5, no. 9 (2022): 11159–1166.*] [8]

The first device, the top interface shown in Figure 5.2(a) and the back interface (unchanged between devices) shown in Figure 5.2(e), features a lattice matched 20 nm of n^+-$In_{0.52}Al_{0.48}As$ as the top barrier layer, atop 250 nm of n-$In_{0.53}Ga_{0.47}As$ absorber and 1000 nm of p^+-$In_{0.52}Al_{0.48}As$. This aligns the L valley of the absorber with the Γ valleys of the top barrier. A L-to-L or X-to-X pathway faces a potential offset, while the more

energetically aligned L-to-Γ transition would be presented with an unfavorable density of states mismatch. A similar density of states mismatch between the L and Γ of the absorber served a central function in carriers not merely transferring to L, but being stored there long enough to maintain a hot carrier population [6]. As such there is good reason to believe that the real space transfer to the top n^+ layer is limited by the mismatch despite energy levels aligning.

Alteration of the top layer's alloy fraction to $In_{0.35}Al_{0.65}As$ results in the band alignment presented in Figure 5.2(b). For clarity, it should be emphasized that the p^+ layer was maintained as the $In_{0.52}Al_{0.48}As$ composition; only the topmost layer was altered. The primary goal in this change was to adjust the L valley of the top barrier to be very slightly lower in energy than the barrier's Γ valley. This rearrangement occurred primarily due to the increase degeneracy of the bandgap (Γ valley), which thereby also produced a larger potential barrier for extraction at the conduction band edge of the InGaAs absorber. This alteration, while proposed to render L-to-L transfer a more favorable extraction pathway than the L-to-Γ of the first generation device structure, the altered energy levels do not serve to mitigate the potential offset for the L-to-L alignment. Furthermore, less desired consequences of the alloy alteration mean that the top layer's lattice constant no longer matches that of the InP substrate, producing strain and inevitably defect formation that could reduce the carrier mobility and hence limit the current density.

Maintaining the consistency of the rest of the device, an $AlAs_{0.8}Sb_{0.2}$ top layer featured in the third device, shown in Figure 5.2(c). The result is a X-to-X alignment of admirable precision, a useful benefit of AlAsSb having an indirect bandgap. AlAsSb additionally

is a better barrier, producing a hefty potential offset to the conduction band edge of InGaAs (~ 1.135 eV). The predicted limitation of this design is in the lattice mismatch, which is expected to result in substantial strain, and defect limited current density much as for the previous device. While the reliance on the X valleys does imply more stringent requirements for excitation to the upper valleys, this is not expected to be prohibitive based upon the internal electric field strength in the InGaAs providing access to the upper valleys for a large proportion of the carriers [6,7]. Based on that understanding, the device was not altered to enhance the field, favoring a better comparison to the earlier devices by remaining structurally unchanged.

Based on early measurements of the AlAsSb top layer device and other investigations into the influence of electric field strength and absorber thickness using the proof-of-concept device stack [10], a number of small adjustments were made to the final device in this study. The InGaAs layer was thickened to 425 nm, with 25 nm delta doped terminal layer in the InGaAs prior to the barrier so as to enhance and extend the electric field farther into the absorber, with the top (barrier) layer exchanged for 50 nm of $GaAs_{0.49}Sb_{0.51}$ extraction layer [8]. The change to the band structure is demonstrated in Figure 5.2(d). While there is a slight potential offset, the overall result is hoped to favor L-to-L extraction, with lower energy requirements than the X-to-X featured in the previous device. The strain is substantially lessened as well. The barrier to the conduction band in this case is less the result of a larger bandgap material, and instead relies upon the potential offset to produce the barrier to extraction for carriers at the conduction band edge. Out of the barriers presented here, the GaAsSb is the smallest, and the Γ valley is lower in energy than the upper valleys. Were carriers to make the L-to-Γ real space

transfer from InGaAs, this would result in lower photovoltage. Although density of states mismatch between L and Γ is expected to limit the scattering rates for such a transition, as was the case for the $In_{0.52}Al_{0.48}As$ top layer device previously [6].

This study benefited in device production from the conventional III-V nature of the materials, and given the characteristic benefits of molecular beam epitaxy this provides assurances as to the quality of the crystals. However, as discussed previously, this is not the same as the devices being entirely free of defects. Indeed, the strain encompassed in the second ($In_{0.35}Al_{0.65}As$ top layer) and third ($AlAs_{0.8}Sb_{0.2}$) devices in particular is not insignificant, and while the topmost epilayers are thin, by comparison of the lattice spacing and elastic constants of the materials, the critical thickness beyond which defects are expected to form to relieve the strain is smaller still. In addition to the $In_{0.35}Al_{0.65}As$ epilayer, which has a critical thickness on InP of ~7.6 nm (less than the epilayer thickness of 20 nm – hence, defects are certain in the upper layer of this structure), the $AlAs_{0.8}Sb_{0.2}$ top layer has a critical thickness of ~3.8 nm (again, less than the 20 nm epilayer) which suggests defects may similarly form. In terms of the electronic properties, this might be expected to result, specifically, in lower currents densities than an unstrained version of the device.

These defects are not believed to be a dominant effect to the extent that all issues with the *J-V* curves may be attributed to them – X-ray diffraction of the crystal structures is a standard step in the calibration of the growth techniques, and we can thereby speak with relative confidence in the overall quality of the material growth. But where the strengths of molecular beam epitaxy for minimizing defects and assuring alloy and doping percentages are on full display in the $In_{0.47}Al_{0.53}As$ and GaAsSb top layers, the strain is

an important note in the other two devices and is anticipated to introduce defects that lower the maximum extracted current densities. In the larger topic of the *J-V* characteristics to be presented later in this chapter, and the voltage-dependent inflections already presented in Chapter 4 that limit the solar cell behavior, there is little justification for attributing the effects to the strain as the defect density is not a factor sensitive to the applied bias in the manner of the barriers to be discussed going forward.

5.3. Results and Discussion

The experimentation and analysis performed on the previous $In_{0.52}Al_{0.48}As$ top layer structure was repeated for the strained $In_{0.35}Al_{0.65}As$ top layer, to verify and study the hot carrier properties the proof-of-concept cell revealed. As Figure 5.3 illustrates, 442 nm and 1064 nm wavelength lasers were again employed to excite above and below the upper L valley of the InGaAs absorber. The result was a non-zero carrier temperature, indicative of hot carrier behavior, and the insensitivity with regards to power suggests that this behavior is dependent on the proposed intervalley mechanisms, rather than the power dependent phonon bottleneck mechanisms that have provided earlier examples of hot carrier behavior in the literature.

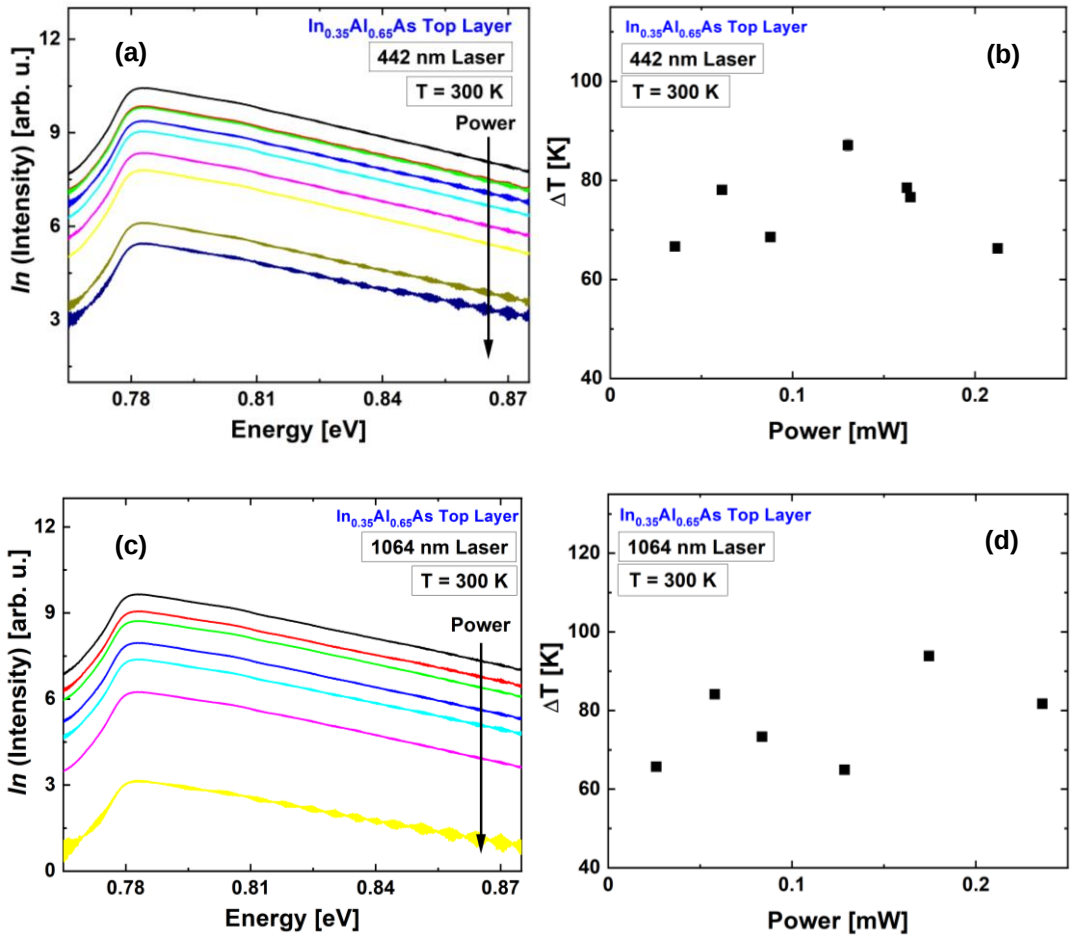

Figure 5. 3. Photoluminescence spectra (a),(c) and analyzed carrier temperature from the high energy tail of the spectrum (b),(d) as a function of applied power for the $In_{0.35}Al_{0.65}As$ top layer device at room temperature for 442 nm (a),(b) and 1064 nm (c),(d) wavelength lasers.

To reiterate the key implications of the hot carrier behavior functioning at both laser wavelengths, the 442 nm wavelength provides sufficient energy for carriers to enter the regime where intervalley phonon scattering is dominant over phonon-mediated thermalization processes in InGaAs. The 1064 nm laser wavelength is insufficient to this task, but provides a supply of carriers to the conduction band, which are then subject to

the influence of the electric field inside the device. This field is not a reference to applied bias, but rather to the internal field generated by the doping profiles present in the structure. This is capable of accelerating and scattering carriers to higher order valleys in the band structure, a long-identified factor in high mobility transistors – the Gunn Effect. The ability of internal fields to provide this up-scattering effect in this set of InGaAs devices is supported by calculations presented for InGaAs in Chapter 4, both of the electric field strength and the valley occupation percentages.

The electronic properties of the device are also similar to that of the unstrained $In_{0.52}Al0_{.48}As$ top layer device; however, this is not as beneficial in the current case. The diode functionality is strong, yet the solar cell behavior, represented by the extension into the fourth quadrant under illumination, is minimized rather than enhanced. For a hot carrier solar cell, a functional device should feature current densities matched to the absorbed photon densities and a beyond bandgap open circuit voltage, and levels associated with the satellite valleys within which the carriers reside. Ideally, this would couple with substantial fill factor, and the device would therefore exceed the single gap efficiency limit. From examination of Figure 5.4, this is not how the device currently operates. The current density in reverse bias suggests full extraction, but as voltage increases towards forward bias an inflection occurs, the current density faltering due to a barrier to extraction, and the solar cell regime is reduced accordingly. The final issue is that the device does not succeed at enhancing photovoltage either. This is not a case of exchanging high current for high operating voltage – rather, there is a larger issue with extraction.

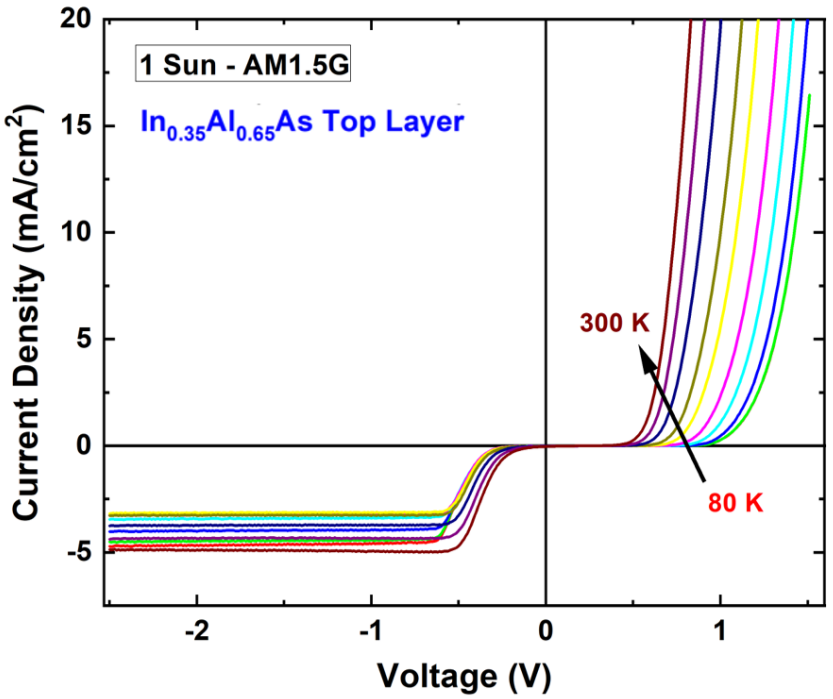

Figure 5. 4. Temperature dependent current density-voltage measurements of the $In_{0.35}Al_{0.65}As$ top layer device under 1 Sun AM1.5G illumination.

The initial proposition, when this behavior was first identified in the proof-of-concept device, was that density-of-states differences between different materials – and indeed, different valleys in different materials – could have a substantial influence on the efficacy with which real space transfer might occur from the upper valley of the absorber to the top n^+ device layer [6]. This altered alloy composition was a test of one possible solution, that by arranging for the top layer's L valley to be the lowest energy among possible valley destinations, extraction might be enhanced. With the *J-V* data presented in the Figure 5.4, this appears to have been insufficient to the task. Given Figure 5.2(b) reveals that this alloy percentage only produced this valley arrangement at the cost of providing a notable potential barrier between the L valleys in question, a reasonable next step would

be to choose a top layer that would favor upper valley extraction over the conduction band edge, yet present as minimal a potential barrier to the upper valley extraction as could be arranged. The AlAsSb top layer sample was crafted to that criterion, albeit via X-valley energy alignment rather than L-valley.

Temperature dependent photoluminescence, presented in Figure 5.5 (a), reveals both a reasonably standard temperature driven redshift for the main peak, a common occurrence in III-V materials. It also, at low temperatures, presents a feature at slightly lower energy. Given the lattice mismatch discussed for the AlAsSb layer, and that the layer exceeds the consequently calculated critical thickness, this may be expected to be related to defects in the crystal structure that formed to relieve the strain. Moreover, alloy fluctuations and non-idealities at the interfaces and known to cause localized centers in these materials [11]. The photon energy emitted by carriers aided in recombination by such defects and localized states would be lower than the bandgap, as befits the nature of a defect that forms to permit the strained crystal to resolve strain to lower energy, and naturally a defect that does not have a favorably lower energy would not well serve as a trap in this sense (though the impact on overall mobility would still exist). A defect 'band' just below the bandgap, as the PL peaks indicate is the case here, will be rendered invisible at higher temperatures, as the carriers will possess more kinetic energy and more high energy states will be occupied.

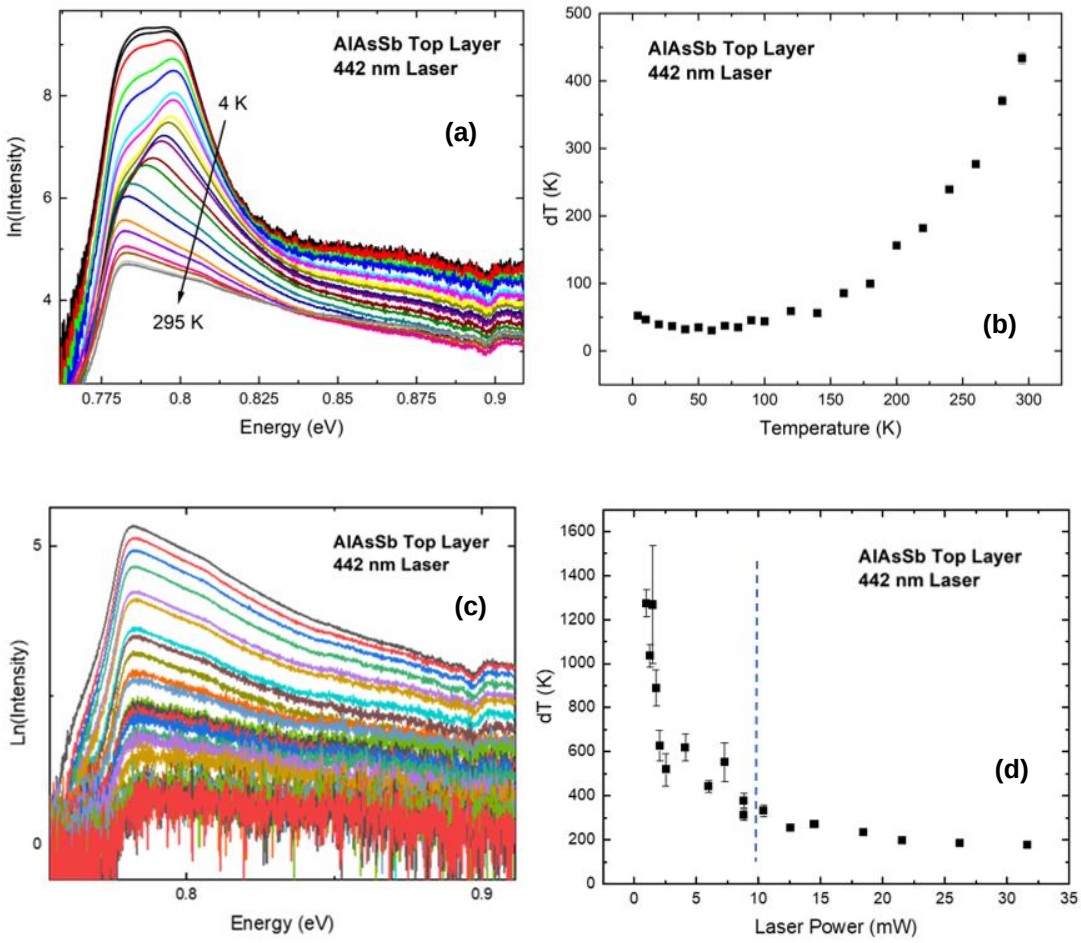

Figure 5. 5. Temperature (a),(b) and power (c),(d) dependent (at 225 K) photoluminescence spectra (a),(c) and carrier temperature analysis (b),(d) of the $AlAs_{0.8}Sb_{0.2}$ top layer device. Due to thermal noise, once signal drops too low the temperature calculation becomes unreliable. This threshold is marked with a dashed line.

The peak itself is small in both peak intensity and full width at half maximum, and on the low energy side of the PL spectrum, hence no obstacle to the established carrier temperature analysis technique based on the high energy tail of the distribution. And at

higher temperatures, the defect levels are of no concern and the analysis is quite standard. The main factor to contend with is the influence of thermal broadening and the signal to noise of the PL signal, both for the temperature dependent study at fixed excitation power, and the lower power intensities employed in power dependent studies at fixed temperature, an example of which is shown in Figure 5.5(c). At lower photoluminescence intensities the precision with which the carrier temperature is determined decreases due to thermal noise.

With these caveats and considerations stated, the conclusion to be drawn from the data still remains relatively consistent: hot carrier behavior exists inside the device. Indeed, while thermal noise is clearly a concern at low illumination power, and it would be quite unlikely for hot carrier temperature to drastically increase, the more reliable data at 'higher' laser powers demonstrates the same insensitivity to power. This result is, perhaps, the anticipated one insofar as the hot carrier behavior depends in our proposed paradigm upon the qualities of the absorber material and the strength of the electric field.

The $AlAs_{0.8}Sb_{0.2}$ device's power dependent current density-voltage data is presented in Figure 5.6. Contrary to the hypothesized outcome, the *J-V* curves primarily demonstrate a lack of solar cell behavior, despite the excellent energy alignment presented in Figure 5.2(c). This was intended to serve as an extraction pathway from the upper X valley [8]. The unusual behavior of this AlAsSb structure is further evident in the power dependence of the *J-V* in Figure 5.6, which is smaller than expected and moreover reversed (positive rather than negative in polarity as expected in photovoltaic (PV) behavior) from the expected enhancement with laser power, reducing rather than increasing current density as the laser intensity increases (seen in the inset to Figure 5.6).

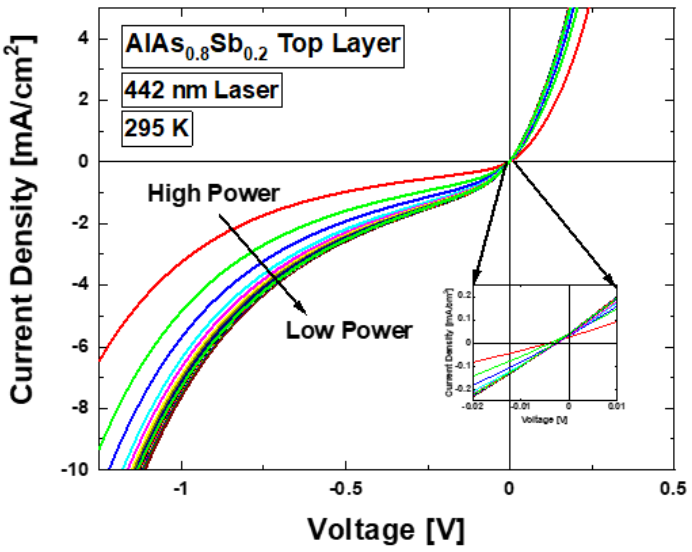

Figure 5. 6. Power dependent J-V measurements of the AlAsSb top layer structure under monochromatic (442 nm) excitation at room temperature. [Reproduced from *Dorman, K. R., et al., "Toward Hot Carrier Extraction in Intervalley Photovoltaic Devices." ACS Applied Energy Materials 5, no. 9 (2022): 11159–1166.*] [8]

While a valid question would be whether this is due to relying on the X valley rather than the L valley, which requires additional energy in InGaAs as seen in the band diagrams of Figure 5.2, this is not supported by calculations of the required energy. For 442 nm wavelength photons, the energy provided ought to more than suffice to enable intervalley scattering to the X valley, and the barrier to Γ valley extraction is that even were the carrier quantity lower in X, the X valley extraction pathway ought to dominate the *J-V* characteristic. In essence, the hypothesized most likely 'failure' condition compared to the ideal hot carrier solar cell would be enhanced photovoltage but minimized current. This was considered, and accounted for. Calculations for the influence of electric field acceleration [6] gave support to an expectation that the field

could serve to mitigate current density loss by accelerating low energy carriers to the extraction pathway via the X valley. The measured results presented in Figure 5.6, with increasing illumination power not enhancing solar cell PV behavior, were not anticipated.

Moreover, in addition to the energy degeneracy between the X valleys of the two materials proving insufficient for efficient real space transfer, the inset of Figure 5.6 once again illustrates that rather than solar cell PV behavior, the device actually moves into a positive photoconductor type photovoltage regime when illuminated. Given that majority carrier extraction rather than minority carrier extraction is enhanced, it appears that in the face of the large potential barrier at the AlAsSb/InGaAs interface, the device functionally operates in reverse rather than overcoming the top barrier. This would involve the n-InGaAs/p^{+}-InAlAs layers operating as a parasitic device, due to the potential barriers to this interface being considerably smaller than the top barrier, dominating in the absence of a functioning minority carrier extraction pathway [8]. Figure 5.2(c) and (e) illustrate the potential barriers in question, and it will be shown this hypothesis is support by differential *J-V* measurements discussed below.

While the heterointerfaces are proposed as responsible for the parasitic effects in the structures described, a reasonable question might be asked if this was, in some way, precipitated by poor electrical contact. Indeed, after early measurements did not feature solar cell behavior and had poor diode performance. More specifically, as seen in Figure 5.7 below, the parasitic InGaAs/InAlAs layer ‘device’ was alarmingly competitive in reverse bias (double diode behavior) with the mediocre performance of the intended diode, decreasing current densities and activating in reverse bias.

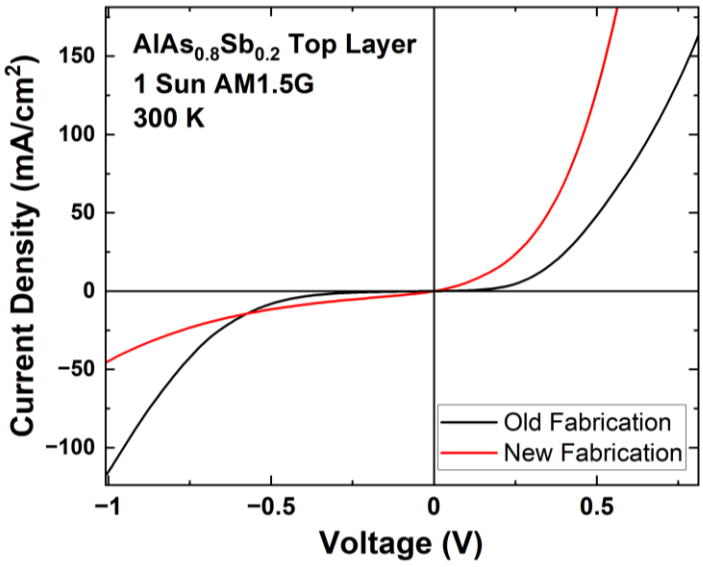

Figure 5. 7. Room temperature *J-V* measurements under the solar simulator for the original and finalized devices differentiated by updates to the metal contacts.

To improve performance and assess the role of the ohmic contacts, investigation of a number of alterative contact metals was performed. Initial samples featured the same contacts as employed for the InAlAs top layer samples: In, then Au for the top n-contact, and Ni followed by AuGe alloy for the bottom p-contact, finalized by rapid thermal annealing at 300 ℃ for 60 seconds. This protocol was improved with the development of a back p-contact of Au/Zn/Au, and a top contact of n-Au/In/Au, and the annealing step was removed after testing. Ultimately, this substantially improved the diode characteristics of the fabricated device, and the *J-V* data in Figure 5.7 above is taken from such a sample. While further room for optimization of the contacts exists, this sufficed to confirm that the quenched solar cell behavior was not solely a result of the metal contacts.

Despite the exacerbated extraction difficulties, the photoluminescence provided some helpful guidance for the design of the final device. The PL spectrum indicated that an alteration to the top layer of the device, with the n^+ doping density maintained, would be expected to have minimal impact if our conjectures are correct, and this guided the previously discussed minor structural alterations in the GaAsSb device. While the electronic behavior of the device does not meet our goals for a hot carrier solar cell, and the reasons for this will be addressed further below, it is promising that the PL proves to be consistent with the larger framework proposed for the workings of an intervalley behavior-based hot carrier device.

For the GaAsSb top layer device, the top contact was altered to Ni/AuGe/Ni/Au, while the back contact was maintained from the AlAsSb top layer device. Rapid thermal annealing of 300 ℃ for 60 seconds was performed to finalize the contacts. This device set aside the X valley alignment, guided by the higher energies required potentially being a problem, and favored an L-to-L real space transfer schema, illustrated in Figure 5.2(d). This would require overcoming a small but extant potential barrier, but alignment between comparatively similar L valleys was preferred to resolve the density of states problems. Initial measurements were, as indicated in Figure 5.8, promising in regards to a stable non-zero power-insensitive hot carrier temperature, and the attendant *J-V* curves feature comparatively substantial solar cell behavior (and further evident in Figure 5.11).

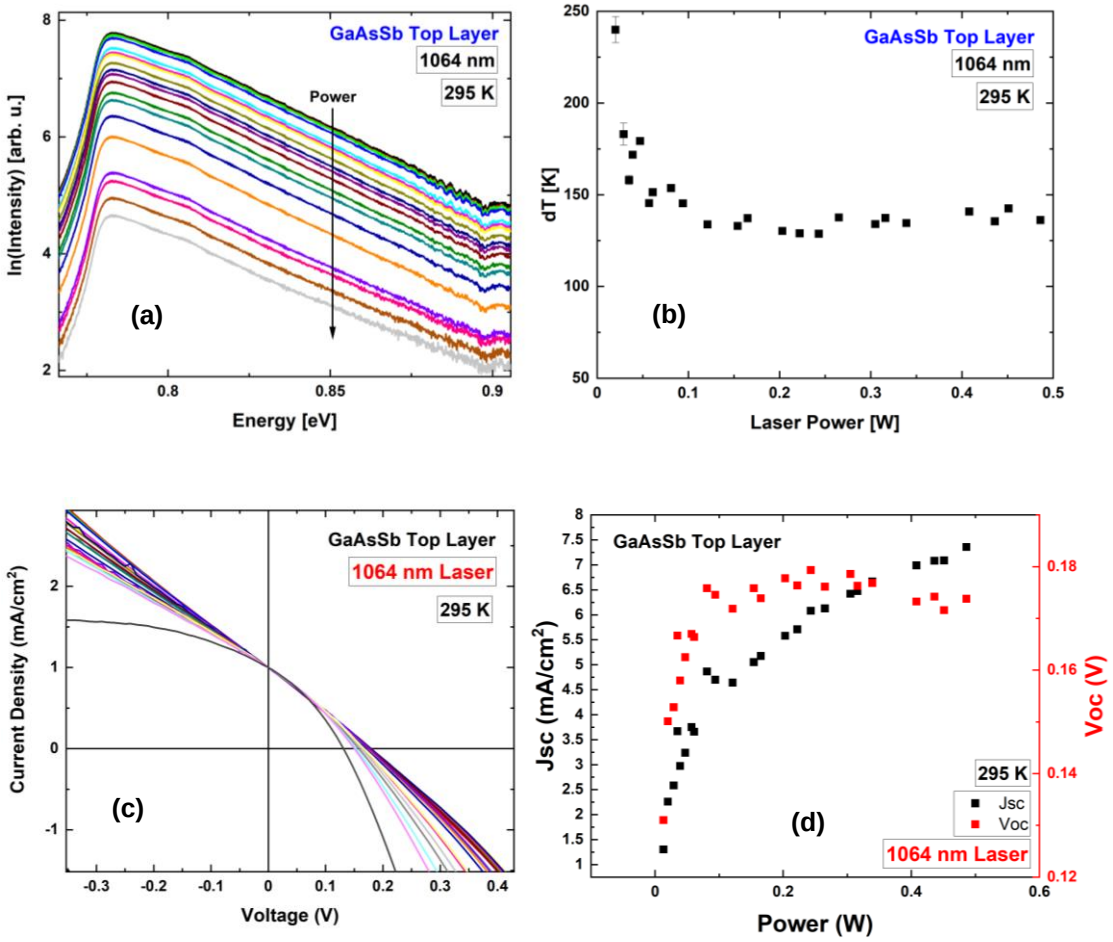

Figure 5. 8. Power dependent photoluminescence spectra (a), carrier temperature analysis (b), normalized to *Jsc J-V* curves (c), and *Jsc* and *Voc* data (d) for the GaAsSb top layer device under the 1064 nm wavelength laser at room temperature.

Both above and below valley laser wavelengths demonstrate this respectable PV behavior, but given the structural devices in this sample, highlighted early – namely, extension of the absorber layer, and delta doping near the top interface – the 1064 nm wavelength laser that excites below the L-valley provides a more pertinent discussion, since it supports the continued aspect of the electric field scattering of carriers to the higher valleys of the band structure despite the changes in device architecture. As the *J-*

V curve is normalized to *Jsc* to better demonstrate, the inflection that so characterized the other devices is also mitigated, though this alone is not equivalent with the final goal of enhancing the photovoltage beyond the absorber bandgap.

In regards to the photoluminescence, a question that must be addressed is the influence the top layer of the device might have upon the spectrum, given the similar bandgaps of GaAsSb and InGaAs. Indeed, as Figure 5.9 below demonstrates, at cryogenic temperatures, there is evidence of multiple peaks.

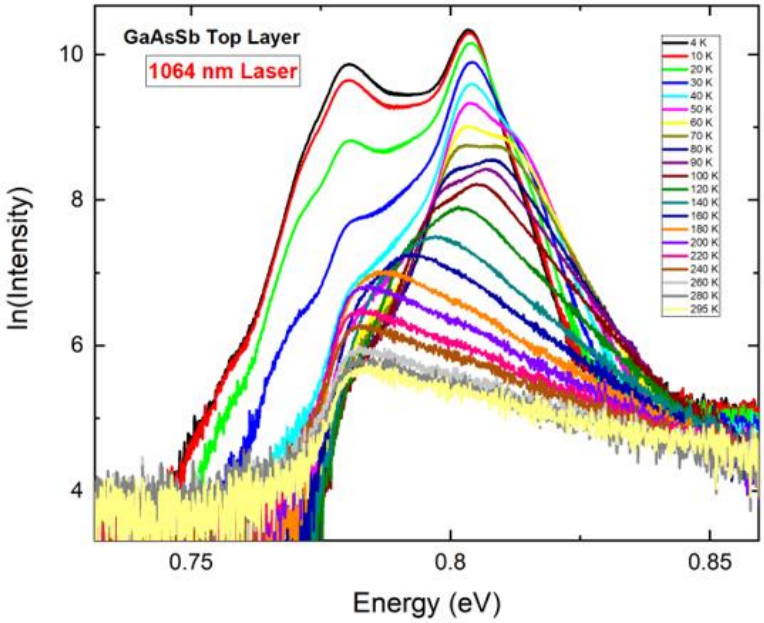

Figure 5. 9. Temperature dependent photoluminescence spectra for the InGaAs/GaAsSb device under the 1064 nm wavelength laser at fixed power.

To better deconvolve the influence of the layers, and to determine whether this has a negative impact on our ability to accurately determine the carrier temperature, a section of the grown wafer was, through photolithography and etching, reduced from a 50 nm GaAsSb top layer to a 20 nm top layer on one half of the wafer. This could then be

mounted into a cryostat, and direction of the laser onto each section of the device could be performed without altering the experimental setup further than lateral adjustment of the cryostat. In this way, as clean a comparison as possible could be obtained to examine the influence the top layer has on the PL spectrum.

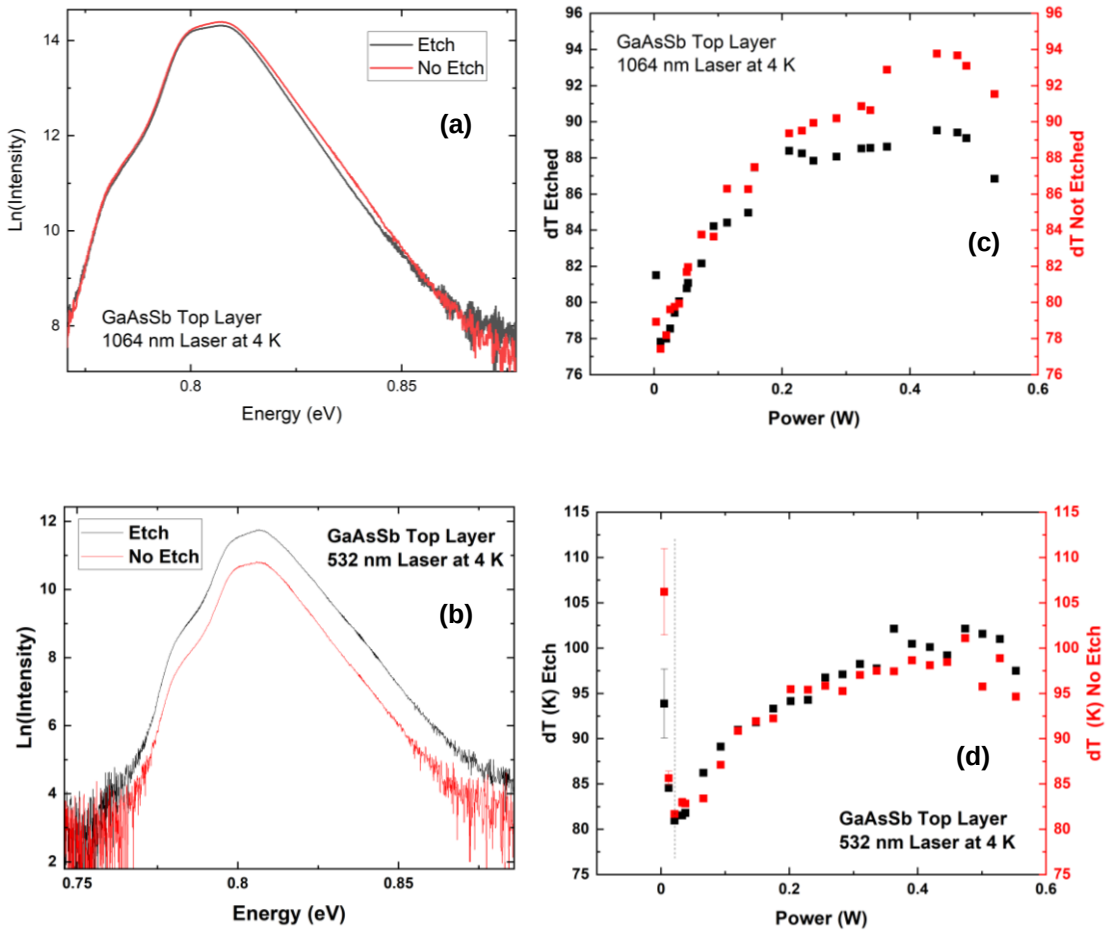

Figure 5. 10. Natural logarithm of the photoluminescence spectra (a),(b) and power dependent carrier temperature analysis (c),(d) of an etched (black) vs unetched (red) GaAsSb top layer structure under monochromatic above (532 nm) (a),(c) and below (1064 nm) (b),(d) valley laser energies at 4 K. The dashed line indicates the regime of low signal compared to thermal noise.

The implication, particularly for the 1064 nm wavelength illumination, is that the top layer's impact is not a substantial concern. Given that a longer wavelength penetrates further into a surface, this might be as expected for the infrared light, as compared to 532 nm wavelength employed for above-valley-energy testing with this sample. The carrier temperature analysis is also consistent between the laser wavelengths across the same range of powers examined for other samples. As this is simply a wafer and not a device, not current density-voltage measurements could be taken to accompany this comparison, but by the same token this further demonstrates that the hot carrier properties are a result of the material, and not the fabrication specifics. It is the extraction, and not the hot carrier maintenance, that relies upon further research. And to examine this central topic, we must aggregate the lessons learned from these four devices.

5.4. Comparative Analysis of Current Density-Voltage Measurements

Given the structural similarities between the devices, and their similar hot carrier maintenance, comparison between their electronic properties is a viable avenue for determining the influence of the top barrier layer. In Figure 5.11 below, 1 Sun AM 1.5G and monochromatic power-matched measurements (using above valley photon energies) are presented for comparison.

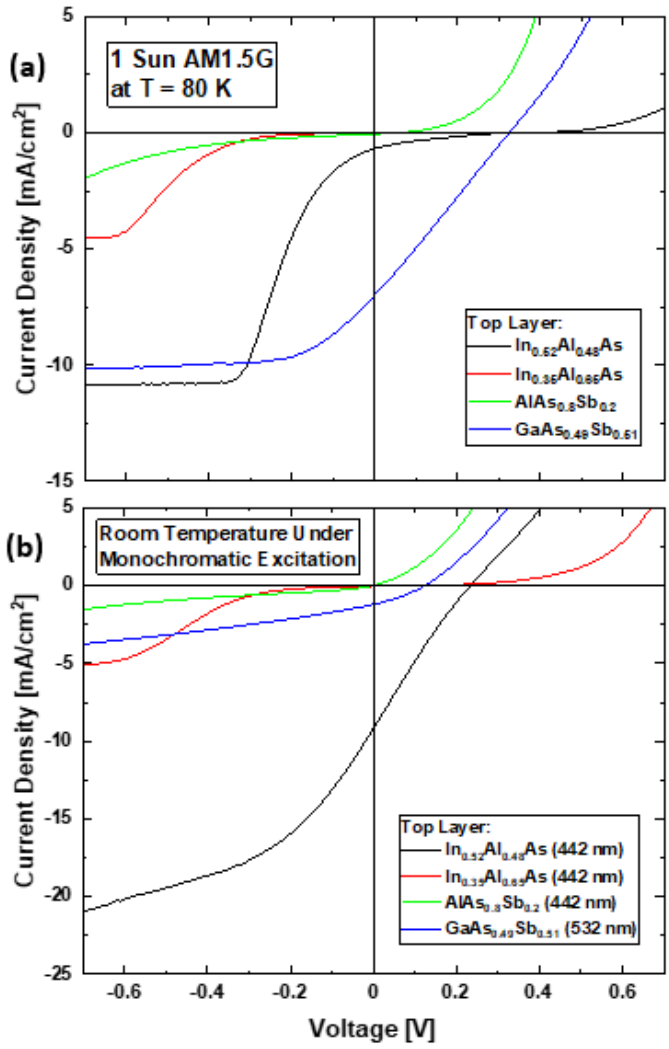

Figure 5. 11. (a) Current density-voltage [*J-V*] measurements under solar simulator at 1 Sun AM1.5G illumination of the four InGaAs heterostructures at a temperature of 80 K. (b) *J-V* measurements at monochromatic excitation with photon energy sufficient to excite above the upper valley each device is designed to operate from (L valley for $In_{0.52}Al_{0.48}As$, $In_{0.35}Al_{0.65}As$, and $GaAs_{0.49}S_{0.51}$, X valley for $AlAs_{0.8}Sb_{0.2}$). The 532 nm laser is power matched to the 442 nm laser via optical density filters. [Reproduced from *Dorman, K. R., et al., "Toward Hot Carrier Extraction in Intervalley Photovoltaic Devices." ACS Applied Energy Materials 5, no. 9 (2022): 11159–1166.*] [8]

While the data under the solar simulator is taken at cryogenic temperatures, the monochromatic current density-voltage data is presented at room temperature. Setting aside practical demonstrations under standard operating conditions, for the fundamental analysis discussed here low temperature measurements for both illumination conditions would have been preferred due to minimizing potential thermal complications. This is the most useful full set of equivalent data recorded for the monochromatic case due to equipment availability over the course of this lengthy study. Furthermore, comparison between Figure 5.11 (a) and (b) emphasizes that despite the temperature differences there is no significant alteration to the limited extraction.

As discussed above, and illustrated in the Figure 5.11, the *J-V* curve representing the proof-of-concept $In_{0.52}Al_{0.48}As$ top layer device (black) suffers a large inflection characteristic of inhibited extraction which limits the fill factor in the solar cell, despite promising reverse bias saturation current density and an indication in the form of projected turn on voltage that the device displays evidence of greater-than-bandgap photovoltage – hot carrier operation [6]. The subsequent study [8] prompted by this, and elaborated in this chapter, revealed the limited extraction to be more endemic to the device structure than anticipated despite a range of alterations to the top layer.

When considering the larger issue of the loss of photovoltage, which is present at high photon energies, as seen in the fourth quadrant behavior in Figure 5.11(b) a reasonable starting assumption is that this is the result of the potential offset at the heterointerface that inhibits carrier extraction – as has been seen in several systems with parasitic barriers [12]. Certainly, a potential barrier might inhibit the extraction of a portion of the carrier distribution in the conduction band – even functionally block extraction entirely if of

sufficient size. Yet the similarity between the behavior of the various samples when excited with 442 nm *and* 1064 nm light – as shown for the $In_{0.52}Al_{0.48}As$ top layer sample in Figure 5.12 – and specifically considering the considerable density of high energy photons generated in this system via laser excitation at 442 nm suggests the origin of the inflection observed in the *J-V* is more subtle than simply carrier localization at the interface.

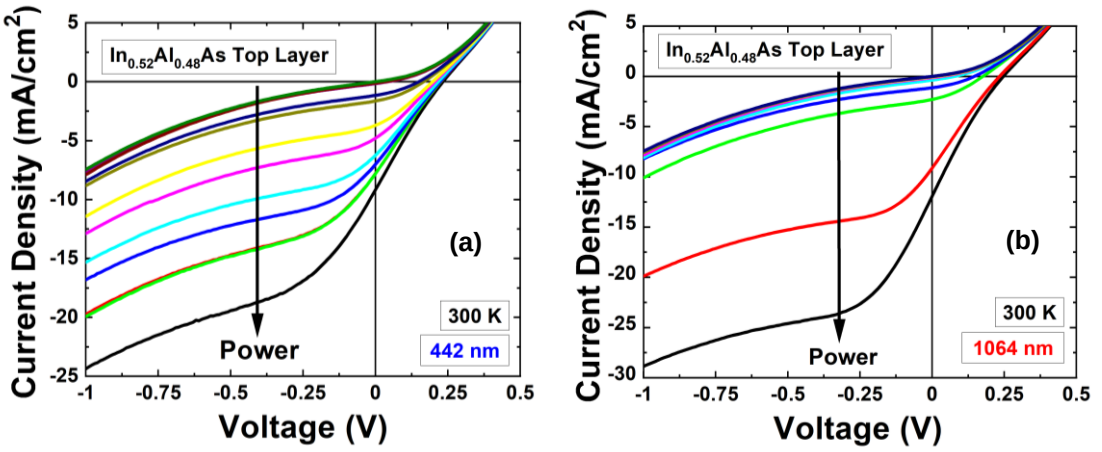

Figure 5. 12. Power dependent *J-V* measurements (with matched maximum power) of the $In_{0.52}Al_{0.48}As$ top layer device at room temperature under 442 nm (a) and 1064 nm (b) wavelength laser light.

In contrast to altering the photon energies, the top barrier layer's impact is rather more substantial– indeed, the 1 Sun AM 1.5G measurements in the Figure 5.11(a) reveal that only the GaAsSb top layer, in blue, is improved according to the typical solar cell metrics of fill factor, *Jsc* and *Voc*. The other devices are further degraded in terms of solar cell performance due to the limited carrier extraction in these devices and as seen in Figure 5.11(b). Therefore, the modifications to the devices were not 'successful' in the context

of a functional hot carrier solar cell, but they are nevertheless useful for understanding the extraction problem and the physics therein if examined in closer detail and with comparison to one another.

The $In_{0.35}Al_{0.65}As$ top layer device (red) in Figure 5.11, features depreciated current density compared to the $In_{0.52}Al_{0.48}As$ top layer device (black) in Figure 5.11, and while a similar inflection occurs in both *J-V* curves, the strained $In_{0.35}Al_{0.65}As$ top layer device faces the inflection at a greater reverse bias [8]. If the assumption is made that the devices are suffering qualitatively from the same barrier, the overall lower current densities are an expected result of the altered alloy percentages due to the strain and the layer thickness exceeding the critical value for defect formation. While this is not a bias dependent effect however, the influence of defects manifesting instead in the material's carrier transport properties. For the bias at which the inflection occurs to alter, implies that the alteration to the energy levels due to the alloy modification has had an impact, and a negative one despite the PL indirectly indicating the high energy carriers scatter to the upper valleys (Figure 5.3) and the band calculation (Figure 5.2(b) indicates that more viable transitions (in regards to density of states conditions) between upper valleys of the absorber and top barrier are better competitive in energy with the now less energetically favorable Γ valley of $In_{0.35}Al_{0.65}As$.

The hypothesis that this was an improvement in providing an extraction pathway had a number of assumptions, now called into question. First, since the energy levels of the L valley of InGaAs are energetically aligned to the Γ valley of the top InAlAs it was considered this may provide a pathway for high energy carriers in the L-valley of the InGaAs absorber into the InAlAs barrier, which proved to be limited by the unfavorable

difference in density of states, or more explicitly the mismatch in momentum across the barrier interface [6]. To circumvent this process, altering the top layer's energy levels via a combination of a different alloy composition ($In_{0.35}Al_{0.65}As$) and strain could improve the degeneracy of the L valley, the lowest energy state, even at the expense of forming a larger potential energy barrier between the valleys of the absorber and the valleys of the top barrier layer. The precise details that produce the inflection at greater reverse bias in the device with the $In_{0.35}Al_{0.65}As$ top layer are difficult to isolate, but it would be plausible to suggest that, given the altered bias of the inflection, the energy level mismatch in the alloy $In_{0.35}Al_{0.65}As$ became more relevant to the inhibiting carrier extraction in this system.

The device incorporating AlAsSb as the top layer in the heterostructures under study is shown in green in Figure 5.11, fails to extract as desired in rather dramatic contrast. Beyond what was expounded in the prior section, the important contribution that this device provides to this investigation is that the extraction unequivocally fails, and that simple valley degeneracy and density of states arguments between the valleys across the absorber/barrier interfaces are not enough to realize a valley photovoltaic hot carrier solar cell. The AlAsSb was chosen to provide a very high potential barrier to the Γ valley extraction pathway, and to provide an excellent match in energy between the X valleys of the two materials. However, there is little room to argue any conclusion except that minority carrier extraction is entirely stymied. The next step then, to proceed to a L-to-L alignment with lower energy requirements, must be taken with the knowledge that the AlAsSb only served, quite successfully, as a barrier but conversely prevents any parasitic

or non-valley transfer effects from inhibiting PV operation were extraction out of the upper valleys realized.

The current density-voltage measurements of the GaAsSb top layer structure, shown in blue in Figure 5.11, reveal a substantially enhanced fill factor, though the 442 nm monochromatic data in Figure 5.11(b) and indicates that this mitigation of the inflection is not equivalent with a strict improvement of all aspects of the solar cell behavior. Furthermore, it should be emphasized that while the solar cell region is improved under the solar simulator, the key characteristic of an operational hot carrier solar cell is the open circuit voltage, which as yet continues to remain less than the bandgap of InGaAs (~0.75 eV at room temperature). Indeed, the inflection is only mitigated in comparison to the other devices rather than removed entirely, and reflects a lower barrier to carrier extraction under conventional PV operation for this system/device.

As can be seen in Figure 5.13(a), if one constructs an 'ideal' *J-V* curve by moving the dark *J-V* to match the reverse saturation voltage, there is a noteworthy amount of improvement to be made by the standards of single gap solar cells, even before reaching into the realm of enhancing the photovoltage as intended for a hot carrier solar cell. Figure 5.13 also emphasizes that the temperature dependence of the GaAsSb top layer device has a photocurrent that is apparently independent of temperature in reverse bias, which is more evident when considering the comparative temperature dependent *J-V* for an InGaAs/AlInAs device shown in Figure 5.13(b), which displays a more typical temperature dependence.

The temperature dependence in the $In_{0.35}Al_{0.65}As$ based device, as demonstrated in Figure 5.4 in the previous section, does not have a particularly strong trend but is

certainly not as independent as the GaAsSb, while the lack of solar cell behavior obscures such concerns in the AlAsSb top layer device. In contrast, behavior shown in Figure 5.13(b) for the $In_{0.52}Al_{0.48}As$ top layer structure is what might be anticipated, with enhancement of the lattice temperature producing a higher energy carrier distribution and hence a larger proportion of carriers overcoming any relevant potential barrier that might exist inside the device.

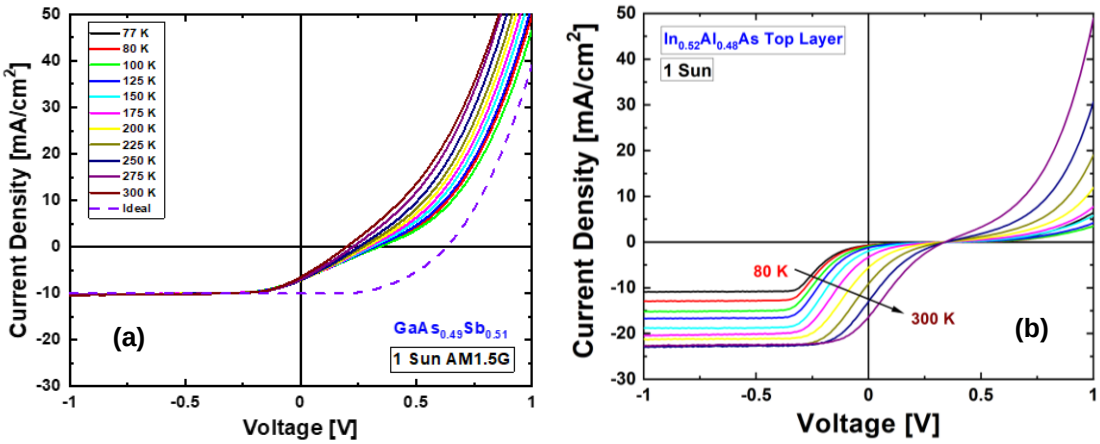

Figure 5. 13. (a) Temperature dependent current density-voltage (J-V) measurements of the GaAsSb top layer structure, performed under solar simulator at 1 Sun illumination and an AM1.5G filter. The 'ideal' curve is the dark J-V shifted down to match the reverse bias saturation current, and serves to illustrate visually the depreciation of the fill factor. [Reproduced from *Dorman, K. R., et al., "Toward Hot Carrier Extraction in Intervalley Photovoltaic Devices." ACS Applied Energy Materials 5, no. 9 (2022): 11159–1166.*] [8] (b) Temperature dependent *J-V* of the $In_{0.52}Al_{0.48}As$ top layer structure, also under 1 Sun AM1.5G conditions.

One possible consideration is that of the devices, the only one fully lattice matched and free of potential strain complications is the $In_{0.48}Al_{0.52}As$ case, and the GaAsSb is not free of that concern. Another is that the GaAsSb may, for better or worse, be functionally circumventing any potential barriers by one means or another once it reaches past ~-0.3 V bias, and hence there is no room for additional current to be extracted. A higher temperature, after all, is not going to excite more carriers from the valence band to the conduction band.

A final distinction between this device and the other heterostructures examined is this study is that the GaAsSb functions as a barrier in a different manner than the other top barriers, given the bandgaps $GaAs_{0.8}Sb_{0.2}$ and $In_{0.53}Ga_{0.47}As$ are quite similar. The offset that serves as a modest barrier to the conduction band edge also results in a barrier to hole transport at the top interface, as Figure 5.2(d) illustrates. This raises the possibility for enhanced recombination loss at the top barrier, especially for photons absorbed in the top layer of the device stack, of which the high energy photons from the 442 nm laser would be more likely to be included. This would be consistent with the poorer performance of the GaAsSb under the monochromatic than under the solar simulator, as seen in Figure 5.11. The similarity of the two bandgaps, based on the tests in the prior session, is not considered to be a substantial problem, but it is nevertheless an inhibition of the optical effectiveness of the device. And what photons are absorbed by the top layer are indeed a loss for the hot carrier properties of the device, as it should be noted that GaAsSb has limitations in terms of hot carrier behavior even under high field conditions [13].

The ultimate conclusion to be drawn for the GaAsSb top layer device is that the improvements to the solar cell behavior are not unilateral, and not the improvements that were aimed for during the design process. In certain respects, the AlAsSb device is, for all the problems with the electrical properties, superior in both optical design and the function of AlAsSb as an extremely successful barrier, for all it failed to provide the X-to-X real space transfer. In contrast, it is entirely conceivable, and rather likely for the GaAsSb device in particular given the temperature dependent J-V curves, that the barriers in the other devices simply provided an unhelpful modulation of standard extraction from the Γ valley. It is a point of fact that despite evidence of hot carrier behavior existing in all devices, none of the devices feature the photovoltage characteristic of a functional hot carrier solar cell [8].

It is a standard assumption that the energy levels of the semiconductor materials as calculated in the band diagrams of Figure 5.2 will guide the motion of carriers through a device. Yet from that assumption, the limited extraction becomes a factor of confusion. While there are a number of non-ideal alignments, based on that assumption it would appear the devices should be at least somewhat functional as hot carrier solar cells. Instead, they are merely devices featuring hot carrier behavior, with effective carrier extraction. We ought to be able to associate barriers to extraction with misalignments, bring in the realities of imperfect growth and fabrication techniques, and draw useful conclusions.

Naturally, there are considerations even the k·p will not include if the mathematical effort is focused on the bandgap rather than potentialities of intervalley transfer. There is a reasonable argument that the different symmetry points possess different density of

states, and thus between Γ or L or X valleys real space transfer requires both energy and momentum conservation to extracted carriers in the upper valleys of the absorber. There is, as the nature of a crystal lattice demands, equivalent symmetry points in the next layer of the zinc blende lattice, even if it be of a different material, and by following this to the intuition that this would benefit the real space transfer, the design of the later devices aligned L-to-L and X-to-X, albeit to little success.

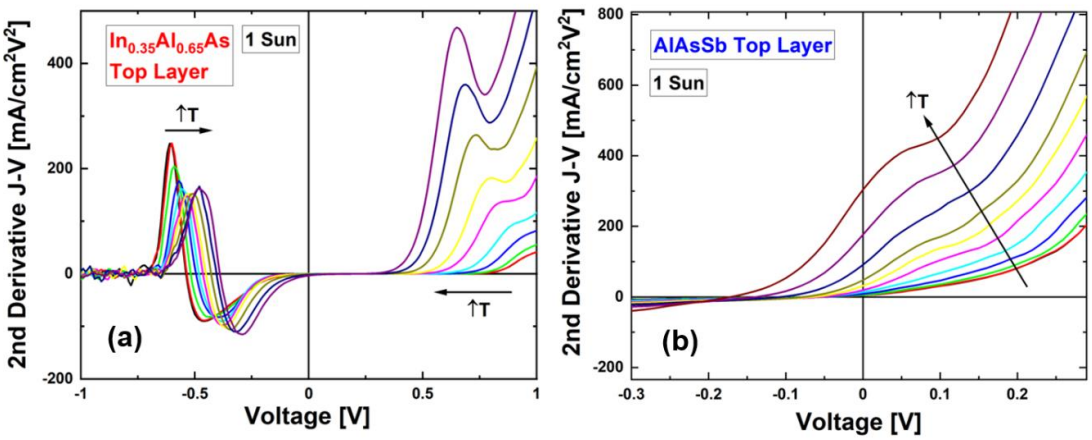

Figure 5. 14. Temperature dependent 2nd derivatives with respect to voltage 1 Sun AM1.5G J-V measurements, (a) the $In_{0.35}Al_{0.65}As$ top layer device featuring two peaks, and (b) the $AlAs_{0.8}Sb_{0.2}$ top layer device featuring only a peak in forward bias. The temperature varies from 77 to 300 K. [Reproduced from *Dorman, K. R., et al., "Toward Hot Carrier Extraction in Intervalley Photovoltaic Devices." ACS Applied Energy Materials 5, no. 9 (2022): 11159–1166.*] [8]

To better view carrier transport *J-V* data is assessed, but rather than the usual more practical extracted current density, the second derivative of the *J-V* with respect to voltage can be plotted to highlight parasitic charge build up in the structure, as shown in

Figure 5.14. This highlights the relationship between the any potential barriers and the voltage, and perhaps more importantly for the difficult to visually parse inflections present in the *J-V* curves of these devices, makes even subtle barriers much easier to locate. Performing this on temperature dependent data taken with solar simulator has the capacity to provide considerable physical information.

The $In_{0.35}Al_{0.65}As$ and AlAsSb top layer data is particularly helpful, illustrating the overall conclusion that the AlAsSb sample only has a single peak and charge accumulation region (and hence, barrier) in forward bias. The other structures, however, feature two peaks, though depending on the top layer and/or the temperature, the reverse bias can be a concealing factor for the forward bias peak. The peak in forward bias can be seen more clearly in dark J-V measurements in those cases, with illumination bringing the peak that dominates in reverse bias to the forefront. The GaAsSb 1 Sun AM 1.5G data is an example of such, as seen in Figure 5.15.

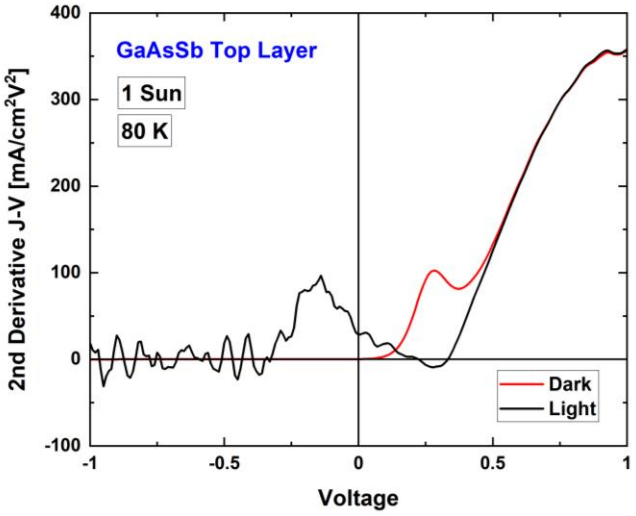

Figure 5. 15. 2nd derivative J-V as a function of voltage for the GaAsSb top layer sample at 80 K, with dark data in red and light (1 Sun AM1.5G) data in black.

Given the consistency with which the forward bias inflection appears, both in the dark current measurements of all devices and as the only evident barrier present in the AlAsSb-based heterostructure, this feature appears to be associated with the potential barrier illustrated in Figure 5.2(e), at the n-InGaAs/p^+-InAlAs interface *in all cases*. When illuminated, the barrier created by the AlAsSb is not surmounted, and instead the device behavior is influenced by back interface acting as a parasitic device - enhancing majority current extraction rather than minority current extraction that would be expected under normal operation [8]. This barrier to hole extraction is consistently present in each device, and has a consistent presence in the dark current. The association between the peak and barrier is a reliable touchstone to then address the origin of the second peak in the J^2I/JV^2 data.

The obvious potential barrier that exists in these devices, setting aside potential offsets between upper valleys, is the upper heterointerface that is intentionally constructed in the device to mitigate the influence of low energy carriers in the Γ valley on the extraction. The light *J-V* curves for the devices other than the AlAsSb top layer sample feature a reverse bias peak in the second derivative that is, by process of elimination, associated with this potential offset, featured in Figures 5.2 (a), (b) and (d). The temperature dependence of the location of these peaks in bias, as presented in Figure 5.14, appear to be associated with increasing thermal energy that becomes available to the carriers, rather than bandgap alterations [8], which is consistent with the relation between a carrier distribution and a potential barrier. In this regard, if the assumption is made that the upper valleys are irrelevant, then extraction via thermionic emission or tunneling is a reasonable assumption, if the bias of the peaks matched the bias necessary to allow

carriers to begin bypassing the potential barrier. A calculation for the bands at various biases can be performed using NRL Multibands ®, and the relevant biased band calculations are presented from this analysis below in Figure 5.16.

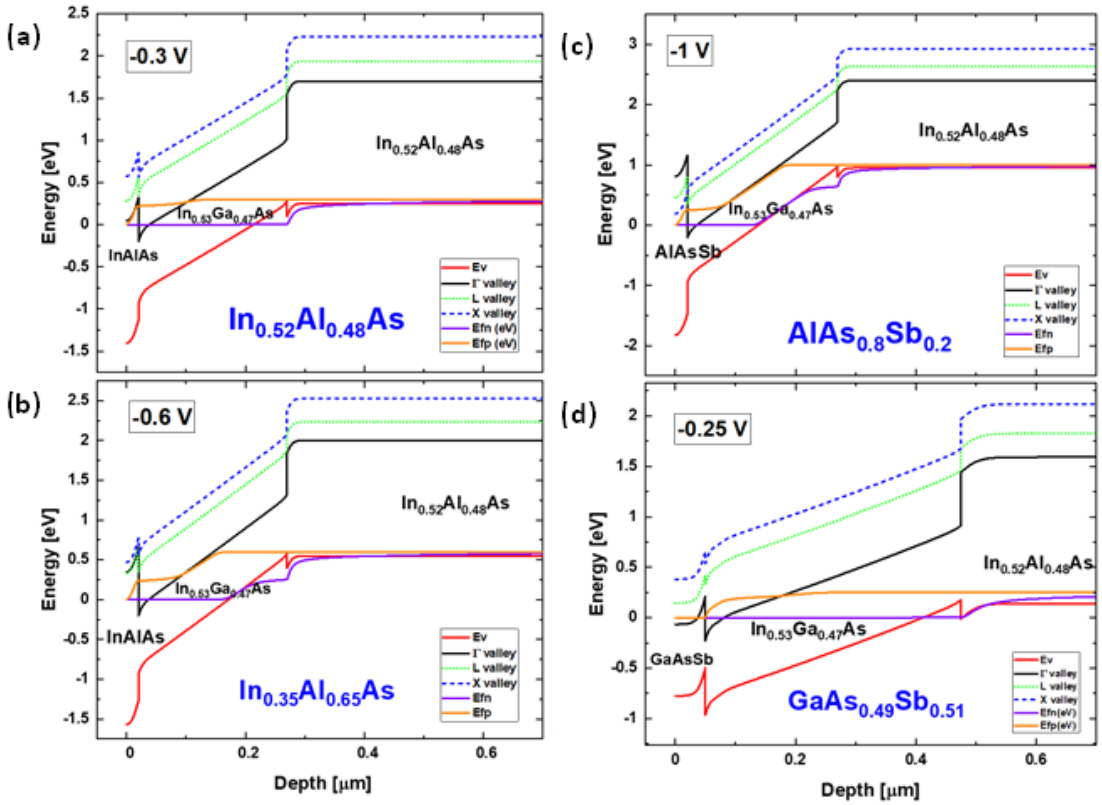

Figure 5. 16. (a) Calculations for the energy level of each upper valley performed in NRL Bands ® at biases matched to the inflections present in the J-V measurements of Figure 5.11. (a) $In_{0.52}Al_{0.48}As$ top layer device. (b) $In_{0.35}Al_{0.65}As$ top layer device. (c) $AlAs_{0.8}Sb_{0.2}$ top layer device. (d) $GaAs_{0.49}Sb_{0.51}$ top layer device. The calculation for the $AlAs_{0.8}Sb_{0.2}$ top layer is given at -1 V bias to highlight its comparative effectiveness as a barrier. [Reproduced from *Dorman, K. R., et al., "Toward Hot Carrier Extraction in Intervalley Photovoltaic Devices." ACS Applied Energy Materials 5, no. 9 (2022): 11159–1166.*] [8]

The alignments in Figure 5.16 that demonstrate (save for the AlAsSb and the enormous associated barrier) bias necessary to enable reasonable extraction from the Γ valley are a strong match to the peaks of the second derivative *J-V* curves, and to the inflections of the *J-V* in reverse bias, where the reverse bias saturation begins to depreciate [8]. The conclusion – that this is the true nature of the barrier presented in the *J-V* curves – then raises the obvious subsequent question of why this is the dominant factor.

From the photoluminescence, there is evidence of hot carrier behavior. This is well explained by the scattering rates and electric field dependence of valley occupation [6,7], and remains consistent through all the devices examined in this chapter. What is lacking is evidence for extraction from that upper valley in any of these cases, even when a viable energy alignment involving upper valleys should be overwhelmingly favorable based on relative energy levels [8]. The conclusion then, to why there is no extraction is that the energy level of the upper valleys is not the correct guideline to follow for designing a device that would rely upon real space transfer between upper valleys. It is no doubt a necessary condition, but an entirely insufficient one for the purposes to which these devices are intended to be applied.

The disregarded condition most likely relates to the momentum of the upper valleys. The local minima are associated with symmetry points, and only the Γ valley is associated with zero momentum. The L and X valleys of zinc blende are at the edges of the Brouillon zone instead, and based on the preponderance of the evidence thus far, this must have implications for real space transfer between upper valleys that cannot be fully satisfied by an energy matching condition. It has been proposed that this involves a conservation of particle velocity across the interface [14]. If there is a momentum

associated with the upper valleys, then differing effective mass across the interface becomes a problem that is not present in the more robust real space transport at the Γ valley.

The boundary condition [15] thereby would be as follows:

$$\frac{1}{m_1^*}\frac{\partial \Psi_1}{\partial x} = \frac{1}{m_2^*}\frac{\partial \Psi_2}{\partial x} \tag{5.1}$$

where m^* is the effective mass.

If, as appears plausible, this is evidently nontrivial away from the Γ valley, by the difficulties presented for the various devices studied here. To solve this, and put it to work in the design of future devises, may require a proper understanding of the complete complex band structure of the materials, not just the real portion as is typically relevant for the energy levels of bands, the guiding condition when only extracting via the Γ valley [14]. This will require future work, but is within the realm of possibility, and provides a useful design principle to better construct the next generation of valley photovoltaic devices.

While the most obvious solution is to simply meet this condition, there is no guarantee that it will be simple or practical in terms of the required materials and associated growth and fabrication techniques. As the current design paradigm for valley photovoltaic devices already places numerous limitations on viable barrier materials, as expounded in Section 5.2, it is worthwhile to consider alternative means of handling this conservation condition rather than presuming a viable material system is guaranteed to exist.

While counterintuitive, there are techniques for disrupting the momentum dependence of the hot carriers across the interface, largely consisting of various ways to render the

interface non-ideal. Interface roughness can provide relief for otherwise strict momentum conditions in intervalley transitions [16]. Transport properties can also be modified via deep donor levels, delta doping, or alloy fluctuations [17], though this is more often a source of trouble than a purposeful choice. The likely consequences of a non-ideal interface do not typically *improve* the function of a semiconductor device, but given there is a great deal of potential benefits for aiming to exceed the single gap limit [1] there may well be room to spare for well-aimed disruption.

Tunneling is another avenue of approach, and intervalley real space transfer has previously been demonstrated in III-V zinc blende materials via resonant tunneling [18,19], and even employed for terahertz quantum cascade lasers [20]. Effectively, this would involve separating the top barrier layer and the energy selective contact into multiple layers, rather than the approach taken in the four devices presented here. In this regard, given how effective it turned out to be as a barrier in this study, for example a thin layer of $AlAs_{0.8}Sb_{0.2}$ might serve as an effective barrier without inhibiting minority carrier extraction were an energy selective contact fit to the top of the device to extract from the X valley instead of relying upon the AlAsSb to serve as both an extraction pathway and a barrier. This would doubtlessly increase production costs, but if the valley photovoltaic solar cell becomes fully operational then the benefits would be more than substantial in recompense.

5.5. Conclusions

To fulfill the potential benefits of valley photovoltaics in a functional solar cell will require alterations to the design principles under which the proof-of-concept InGaAs

heterostructures have been constructed. By comparison between a set of four devices with different top layers for barrier and extraction purposes, the need for a means of real space transfer is made evident, as are the requirements of this extraction [8]. While the hot carrier behavior in the InGaAs is made robust under standard operating conditions (1 sun, room temperature) by reliance on the upper valleys, those same valleys are not a trivial extraction pathway that can be connected to by energy degeneracy in the top n^+ layer alone. Beyond meeting the particle velocity boundary condition, other possible solutions include modification of the interface towards purposeful non-ideality, or creation of an energy selective contact via resonant tunneling.

References

[1] Shockley, William, and Hans J. Queisser. "Detailed Balance Limit of Efficiency of p-n Junction Solar Cells." *Journal of Applied Physics* 32, no. 3 (1961): 510-19.

[2] Ross, Robert T., and Arthur J. Nozik. "Efficiency of Hot-carrier Solar Energy Converters." *Journal of Applied Physics* 53, no. 5 (1982): 3813-818.

[3] Hirst, L. C., R. J. Walters, M. F. Führer, and N. J. Ekins-Daukes. "Experimental Demonstration of Hot-Carrier Photo-Current in an InGaAs Quantum Well Solar Cell." *Applied Physics Letters* 104, no. 23 (2014): 231115.

[4] Rodière, Jean, Laurent Lombez, Alain Le Corre, Olivier Durand, and Jean-François Guillemoles. "Experimental Evidence of Hot Carriers Solar Cell Operation in Multi-Quantum Wells Heterostructures." *Applied Physics Letters* 106, no. 18 (2015): 183901.

[5] Whiteside, V. R., H. Esmaielpour, T. D. Mishima, K. R. Dorman, M. B. Santos, D. K. Ferry, and I. R. Sellers. "The Role of Intervalley Phonons in Hot Carrier Transfer and Extraction in Type-II InAs/AlAsSb Quantum-Well Solar Cells." *Semiconductor Science and Technology* 34, no. 9 (2019): 94001.

[6] Esmaielpour, Hamidreza, Kyle R. Dorman, David K. Ferry, Tetsuya D. Mishima, Michael B. Santos, Vincent R. Whiteside, and Ian R. Sellers. "Exploiting Intervalley Scattering to Harness Hot Carriers in III–V Solar Cells." *Nature Energy* 5, no. 4 (2020): 336-43.

[7] Ferry, D. K. "In Search of a True Hot Carrier Solar Cell." *Semiconductor Science and Technology* 34, no. 4 (2019): 44001.

[8] Dorman, Kyle R., Vincent R. Whiteside, David K. Ferry, Israa G. Yusuf, Tanner J. Legvold, Tetsuya D. Mishima, Michael B. Santos, Stephen J. Polly, Seth M. Hubbard, and Ian R. Sellers. “Toward Hot Carrier Extraction in Intervalley Photovoltaic Devices.” *ACS Applied Energy Materials* 5, no. 9 (2022): 11159–1166.

[9] Gunn, J. B. "Microwave Oscillations of Current in III-V Semiconductors." *Solid State Communications* 88, no. 11 (1993): 883-86.

[10] Dorman, Kyle R., Vincent R. Whiteside, David K. Ferry, Tetsuya D. Mishima, Israa Yusuf, Hamidreza Esmaielpour, Michael B. Santos, and Ian R. Sellers. "Electric Field and Its Effect on Hot Carriers in InGaAs Valley Photovoltaic Devices." *IEEE Journal of Photovoltaics* 12, no. 5 (2022): 1175-183.

[11] Tang, J., V. R. Whiteside, H. Esmaielpour, S. Vijeyaragunathan, T. D. Mishima, M. B. Santos, and I. R. Sellers. "Effects of Localization on Hot Carriers in InAs/$AlAs_xSb_{1-x}$ Quantum Wells." *Applied Physics Letters* 106, no. 6 (2015): 061902.

[12] Saive, Rebecca. "S-Shaped Current-Voltage Characteristics in Solar Cells: A Review." *IEEE Journal of Photovoltaics* 9, no. 6 (2019): 1477-484.

[13] Ferry, David K. "High Electric Field Transport in $GaAs_{0.51}Sb_{0.49}$." *Semiconductor Science and Technology* 36, no. 4 (2021): 45024.

[14] Ferry, David K., Vincent R. Whiteside, and Ian R. Sellers. "Pathways to Hot Carrier Solar Cells." *Journal of Photonics for Energy* 12, no. 2 (2022): 022204.

[15] Bastard, G. "Superlattice Band Structure in the Envelope-function Approximation." *Physical Review B: Condensed Matter* 24, no. 10 (1981): 5693-697.

[16] Teissier, R., J. J. Finley, M. S. Skolnick, J. W. Cockburn, J. Pelouard, R. Grey, G. Hill, M. A. Pate, and R. Planel. "Experimental Determination of Γ-X Intervalley Transfer Mechanisms in GaAs/AlAs Heterostructures." *Physical Review B: Condensed Matter* 54, no. 12 (1996): R8329-8332.

[17] Fernández De Avila, S., J. L. Sánchez-Rojas, F. González-Sanz, E. Calleja, E. Muñoz, P. Hiesinger, K. Köhler, and W. Jantz. "Influence of Delta-doping Profile and Interface Roughness on the Transport Properties of Pseudomorphic Heterostructures." *Applied Physics Letters* 64, no. 7 (1994): 907-09.

[18] Mendez, E. E, W. I Wang, E. Calleja, and C. E. T Goncalves Da Silva. "Resonant Tunneling via X-point States in AlAs-GaAs-AlAs Heterostructures." *Applied Physics Letters* 50, no. 18 (1987): 1263-265.

[19] Liu, H. C. "Resonant Tunneling through Single Layer Heterostructures." *Applied Physics Letters* 51, no. 13 (1987): 1019-021.

[20] Roy, M., and M. A. Talukder. "Terahertz Quantum Cascade Laser with an X-valley-based Injector." *Journal of Applied Physics* 121, no. 13 (2017): 133104.

Chapter **6**

Electric Field and its Influence on Hot Carriers in InGaAs Heterostructure Devices

6.1. Introduction

In order to overcome the single gap limit [1] for solar cell efficiency through minimizing thermalization loss with hot carrier methodologies [2], much focus has been directed to the phononic behavior of absorber materials [3, 4, 5]. This form of study has led naturally from the restriction of thermalization mechanisms to the formation of a phonon bottleneck, wherein given sufficient illumination power and mitigated phonon scattering rates for thermalization pathways it becomes possible to observe hot carrier behavior given the device is exposed to high illumination powers [5, 6, 7]. While a step forward not to be derided, this approach has not yet produced breakthroughs in practical application, and it was the creation of the intervalley scattering-based device featured in Chapter 4 that first demonstrated hot carrier behavior under more generally realistic conditions [8, 9]. These hot carrier devices are hoped to become generational improvements on the single bandgap III-V devices, and operating at room temperature and illumination intensities consistent with the solar spectrum are key advances. Nevertheless, there is more work to be done to develop the valley photovoltaic concept.

The proposed intervalley phonon scattering mechanism for transfer of high energy ‘hot’ carriers into the upper valleys of the absorber are well established, if applied to a

novel solar cell concept. Simulations for the idealized crystal structure of the absorber are sufficient for grasping an understanding of the relevant phonon scattering rates, and typical variances that the device might be subjected to such as illumination intensity and applied voltage are not expected to cause noteworthy divergence of this mechanism from the theorized predictions [9]. However, while the electric field-driven scattering of electrons in bulk III-V semiconductor layers is long established [10], the application of external bias, alteration of doping profiles and the associated internal electric fields, or even the alteration in field strength due to carrier accumulation at interfaces can plausibly interact with this mechanism. Both mechanisms are required for the valley photovoltaic device [11], and hence further experimentation in regards to the realities of the electric field mechanism for exciting low energy carriers to the upper valleys is a necessity.

6.2. Experimental Methodology and Device Structure

To gain a better understanding of the electric field-driven intervalley scattering in specific, and the valley photovoltaic mechanisms as a whole, devices with altered electric field strengths across the absorber region yet maintaining the same intervalley phonon scattering properties are a potential avenue of study. Thus, in this work the proof-of-concept bulk InGaAs absorber design [8] has been modified by changing the absorber thickness. Once again grown by molecular beam epitaxy, the previous 250 nm InGaAs absorber layer was thinned, and three additional variants with 25 nm, 50 nm and 100 nm thicknesses were processed into devices through standard III-V techniques of photolithography, and thermal evaporation of Zn/Au top n-contacts and AuGe alloy bottom p-contacts. The resulting 20 nm n^+-$In_{0.52}Al_{0.48}As$ /(25 or 50 or 100) nm n-$In_{0.53}Ga_{0.47}As$ /1000 nm p^+-$In_{0.52}Al_{0.48}As$ /p-InP substrate structure features substantially

altered electric field strength across the absorber, as shown in Figure 1(b). Including prior data from the 250 nm absorber structure, this provides a comparative cohort of four samples across a broad range of field strengths.

(a)

n+: $In_{0.52}Al_{0.48}As$, 20 nm, 1e18 cm-3
n : $In_{0.53}Ga_{0.47}As$, 25 or 50 or 100nm, 1e15 cm-3
p+: $In_{0.52}Al_{0.48}As$, 1000nm, 1e18 cm-3
p: InP substrate (1/2 of a 2" substrate)

(b)

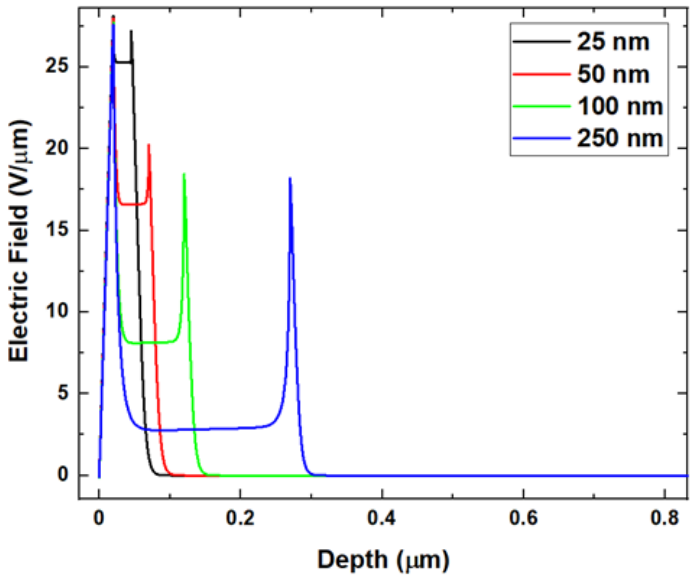

Figure 6. 1. (a) Device layers as grown for this study by molecular beam epitaxy and (b) electric field strength calculated in NRL MultiBands ® for the InGaAs absorber heterostructure.

The field strength is simulated with NRL MultiBands ®, an integrated 8 band k·p solver and Poisson solver that includes the influence of strain, doping and temperature in its calculation of device characteristics, and demonstrates enhanced field at the

interfaces due to changes in the doping density across the structure. The electric field across the bulk of the absorber is perhaps more useful for determining the influence of the field on carrier extraction. It is necessary to caution that prior calculations of the influence of electric field on relative valley population for InGaAs are not rigorously applicable [9], as the 250 nm thickness of the proof-of-concept sample [8] is incorporated into the calculation of how much energy the field can provide to the carriers. The field strengths involved are substantially in excess of the amount required for accelerating a substantial quantity of carriers to upper valleys, and this is thus not anticipated to result in negative consequences for the hot carrier behavior in the new devices, but it is a point of subtlety to keep in mind rather than presume the previous calculations [9] (shown in Figure 6.13 and discussed further in Section 6.4) are fully accurate.

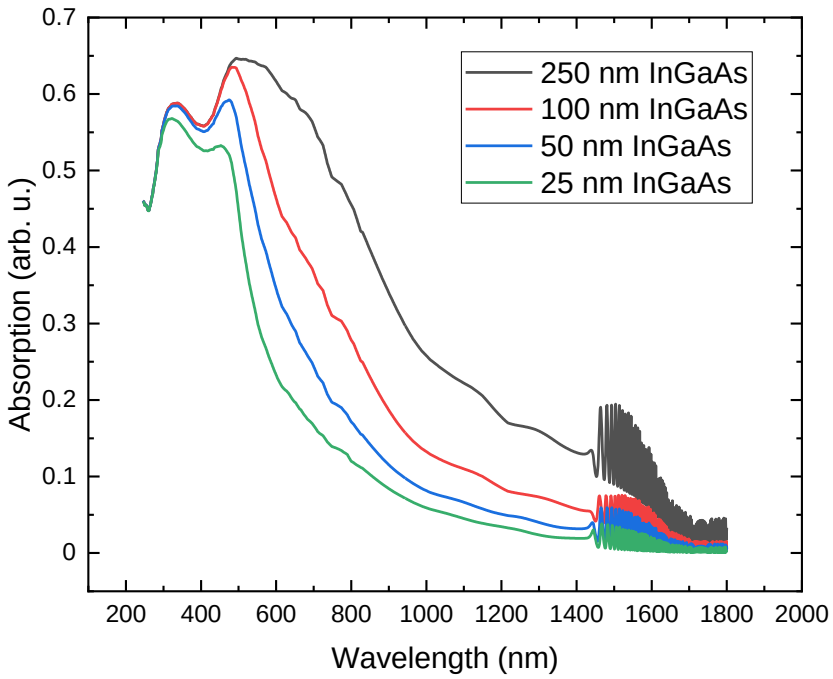

Figure 6. 2. Absorptivity of each device as a function of wavelength, calculated in Mathematica from refractive index data [12].

In addition to electric field, the thickness of the absorber also affects the absorptivity of the sample. Transfer matrix calculations performed in Mathematica for the structure provide a useful reference for the impact under different illumination in Figure 6.2.

The thinned absorber samples are calculated to perform similarly to the proof of concept 250 nm InGaAs structure under 442 nm laser light, but under monochromatic illumination with the 1064 nm wavelength infrared beam there is substantial loss of absorptivity. This is particularly important for this study, as within the framework of valley photovoltaic mechanisms [9], the influence of the electric field is most decoupled from intervalley scattering effects when the photon energy is insufficient to excite to the upper valleys of InGaAs. As in the previous chapters, the 1064 nm wavelength laser serves that purpose in this set of experiments.

6.3. Low Intensity Experimentation and Results

Before further examining the electronic behavior, it is important to the context of the discussion to establish the results of the photoluminescence measurements performed on the three devices. As previously, monochromatic excitation was performed with 1064 nm wavelength (below the upper valley and top barrier) and 442 nm wavelength (above the upper valley and top barrier) laser light. This enables probing of the electric field aided acceleration and the intervalley scattering mechanisms, respectively. The excitation powers were varied, but kept low in power, incident illumination power matched between both lasers, and the measurements were performed at room temperature.

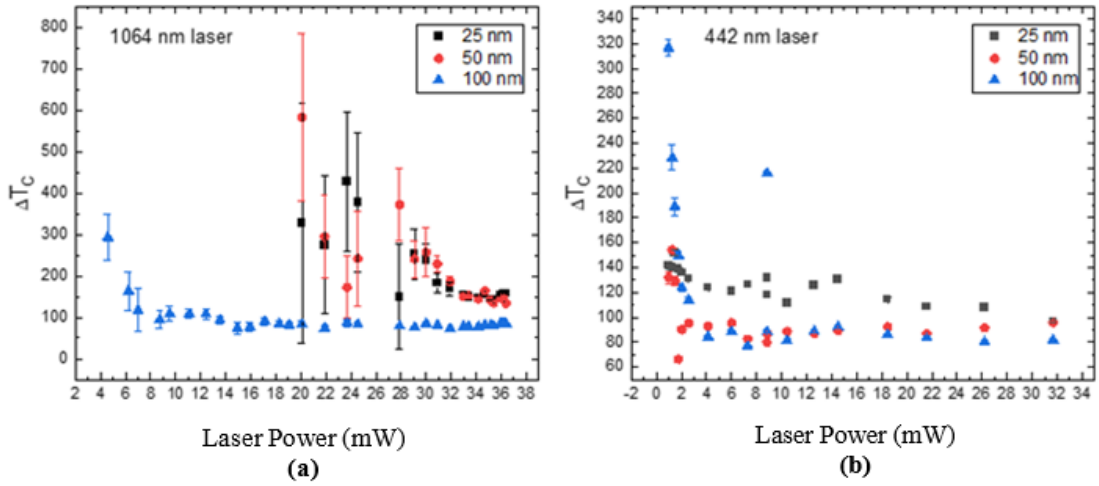

Figure 6. 3. Hot carrier temperature in each device, expressed as the difference from the lattice temperature ΔT_c, as a function of incident laser power for (a) a 1064 nm wavelength laser source and (b) a 442 nm wavelength laser source.

The first and most important result of analysis of the photoluminescence may clearly be seen in Figure 6.3: upon applying the generalized Planck relation to characterize the carrier distribution, a substantial difference from the lattice temperature arises, approximately 100 K for the 100 nm absorber sample (blue triangles). The carrier temperature is higher in the thinner absorber samples which feature enhanced electric field strength: Figure 6.3(a) reveals higher carrier temperature estimates under the 1064 nm wavelength laser for the 25 nm (black squares) and 50 nm (red circles) absorber devices, in comparison to the 442 nm wavelength laser data presented in Figure 6.3(b). It is not a sufficiently substantial difference to make confident assertions of a trend given the imprecision of the analysis. The cause of this is the low absorption (Figure 6.2) of the infrared photons resulted in substantially weaker signal for the 1064 nm data in

Figure 6.3(a) in the thinner samples, resulting in the swiftly expanding error of the fitting and the lack of very low power data points.

What may be more confidently asserted is that the hot carrier temperature does not deactivate at low power (and the entire suite of applied powers is in the low power regime in this context) as in the typical case of a phonon bottleneck. The intervalley phonon scattering is probed by the 442 nm laser and the electric field acceleration is probed by the 1064 nm laser, but nevertheless for a given absorber thickness both lasers provide comparable carrier temperatures despite the large difference in photon energies. This is consistent with the valley photovoltaic proposal – the temperatures being similar because the intervalley mechanisms store the carriers in the same upper valleys [8].

As much as the reliable maintenance of a hot carrier population is valuable, the question of carrier extraction inevitably requires discussion for solar cell applications. To that end, current density-voltage measurements were taken under 1 Sun AM1.5G solar simulation (Figure 6.4(a)), and under both the 442 nm (Figure 6.5, Figure 6.6 and Figure 6.7) and 1064 nm laser excitation (Figure 6.8 and Figure 6.9), to examine anticipated evidence of the same properties of inhibited carrier extraction in these systems. All of the following measurements occurred at room temperature, with the monochromatic data taken in the same measurement sessions as the associated photoluminescence.

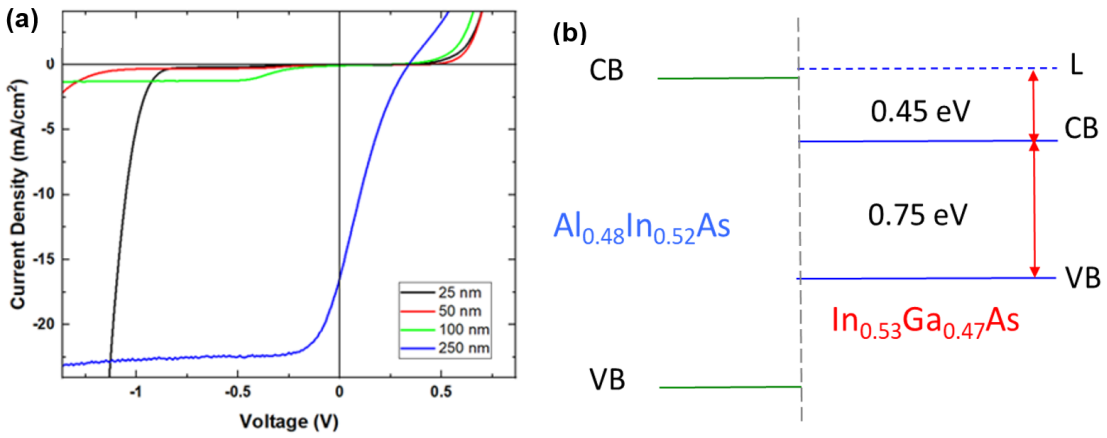

Figure 6. 4. (a) Current density-voltage measurements for 25 nm, 50 nm, 100 nm, and 250 nm InGaAs absorber layer devices under 1 Sun AM1.5G room temperature conditions. (b) A schematic for the top interface of the devices, showing the relevant valley energies and band edges.

Figure 6.4(a) compares current density-voltage measurements for the different absorber thicknesses under the solar simulator, revealing that inflection of the J-V and the associated loss of fill factor are present in all samples. The location of the inflection – and presumably the voltage needed to overcome the associated potential barrier – differs. Figure 6.4(b) illustrates the band and valley alignments at the top interface and the associated potential offset at the conduction band edge schematically. Given the absence of enhanced photovoltage in the J-Vs (while the potential is present the reality of the depreciated fill factor, short circuit current and open circuit voltage must be addressed) the function of the top heterojunction is as a barrier to all extraction *rather than* an effective energy selective contact via an L to Γ valley extraction pathway.

Also on display is an expected, yet exaggerated, influence of the absorber thickness upon the total current density. The thinner samples feature far lower current density than may be explained by changes in absorptivity alone.

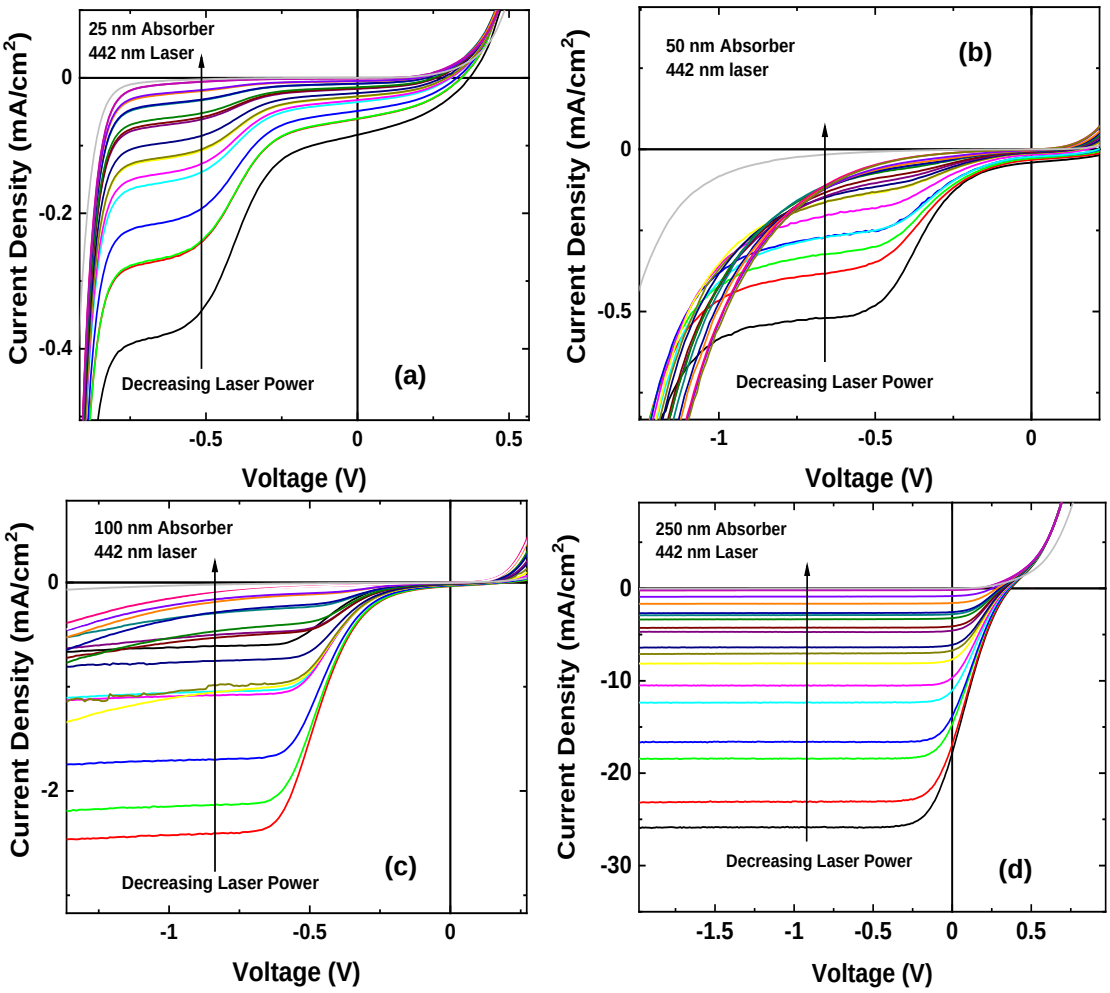

Figure 6. 5. Power dependent current density voltage measurements under 442 nm wavelength illumination for the (a) 25 nm, (b) 50 nm, (c) 100 nm, and (d) 250 nm absorber thickness devices.

Under 442 nm wavelength illumination, the carriers are excited high into the conduction band of InGaAs, above the potential barrier of InAlAs and the L valley of

InGaAs. Consequently, intervalley scattering is the dominant mechanism, though the electric field is a present factor. Zener breakdown can be seen in the two thinner samples (see Figure 6.5(a) and (b)), occurring at larger negative bias as the thickness increases, while the thicker samples feature the reverse bias saturation usually associated with a more standard Schottky *J-V* characteristic. The higher electric fields of the thinner absorbers result in a more sloped *J-V* shape. As seen in the 1 Sun data (Figure 6.5(a)), the total current density is drastically decreased with absorber thickness beyond the influence of lowered absorptivity. The J-V as presented above in Figure 6.5 does not provide a useful visualization for the full power dependence. In Figure 6.6, the same data is normalized past the inflection in the *J-V* response. This places the solar cell quadrant in the top right of the new figures.

With the normalization, a steady shift from the shape of the 25 nm absorber (Figure 6.6(a)) towards that of the 250 nm absorber (Figure 6.6(b)) is more evident, although complicated by the avalanche effect at lower absorber thicknesses. Additionally, aside from the 250 nm thickness case, the knee of the inflection clearly moves towards smaller reverse bias values as the power decreases, until the s-shape vanishes. This may be explained by tunneling through the top InAlAs barrier, a pathway that at low excitation powers may successfully account for the entirety of the extracted current density, removing the inflection associated with the potential offset (illustrated in Figure 6.4(b)).

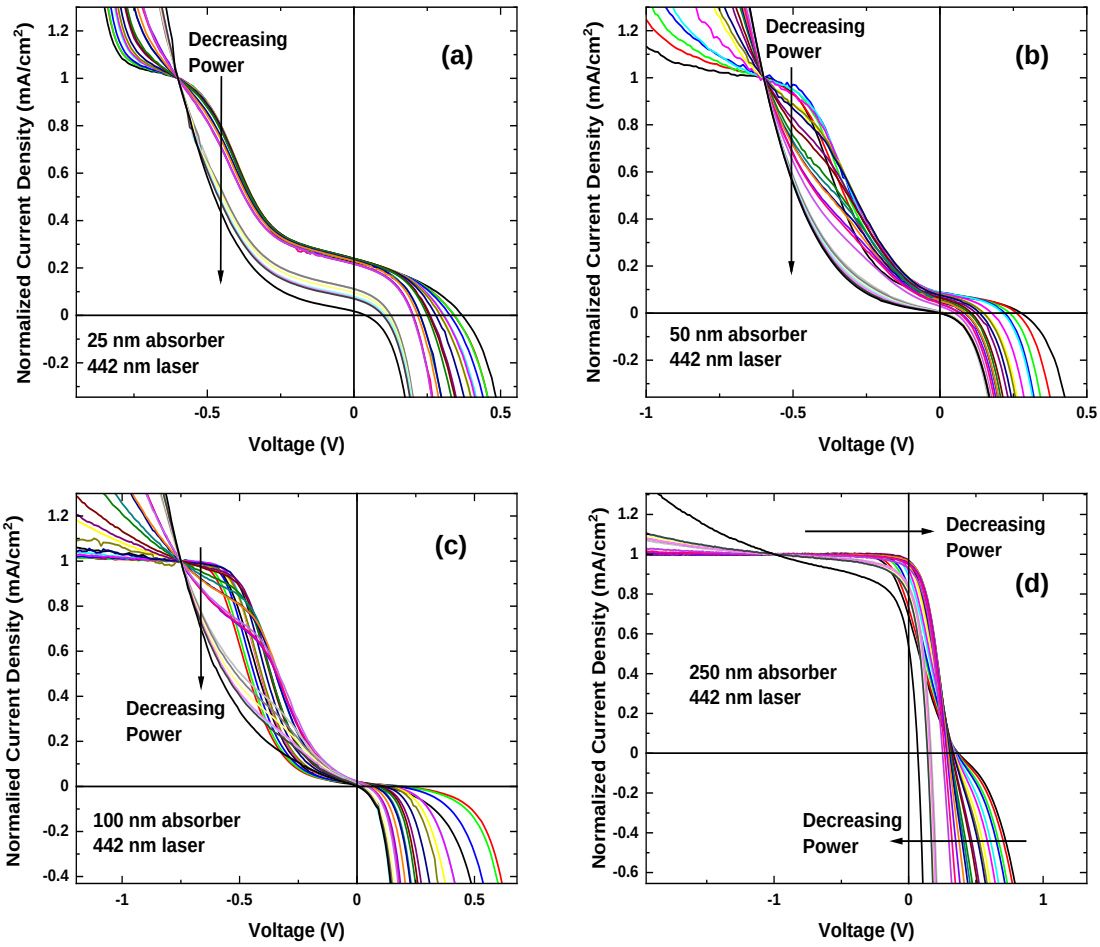

Figure 6. 6. Normalized current density voltage measurements under 1064 nm wavelength illumination for the (a) 25 nm, (b) 50 nm, (c) 100 nm, and (d) 250 nm absorber thickness devices.

Figure 6.7 demonstrates this progression with more clarity. A closer examination of the 250 nm absorber case clarifies the movement of the knee away from negative bias, and the removal of the s-shape at low power in Figure 6.7(b). As it is the absorber thickness, not the barrier thickness, that differs between the devices, tunneling across the top barrier is an effect present in all cases. For the 250 nm absorber device, this ultimately results in a visually improved fill factor at lower powers, though this can be seen to be

simultaneous with decreased open circuit voltage and, although this is only visible in Figure 6.6 and not Figure 6.7 due to the normalized current density, drastically lowered short circuit current density. Furthermore, a fully operation hot carrier solar cell based on these principles would ideally operate at the energy of the L valley, and feature a V_{oc} in excess of 1 V.

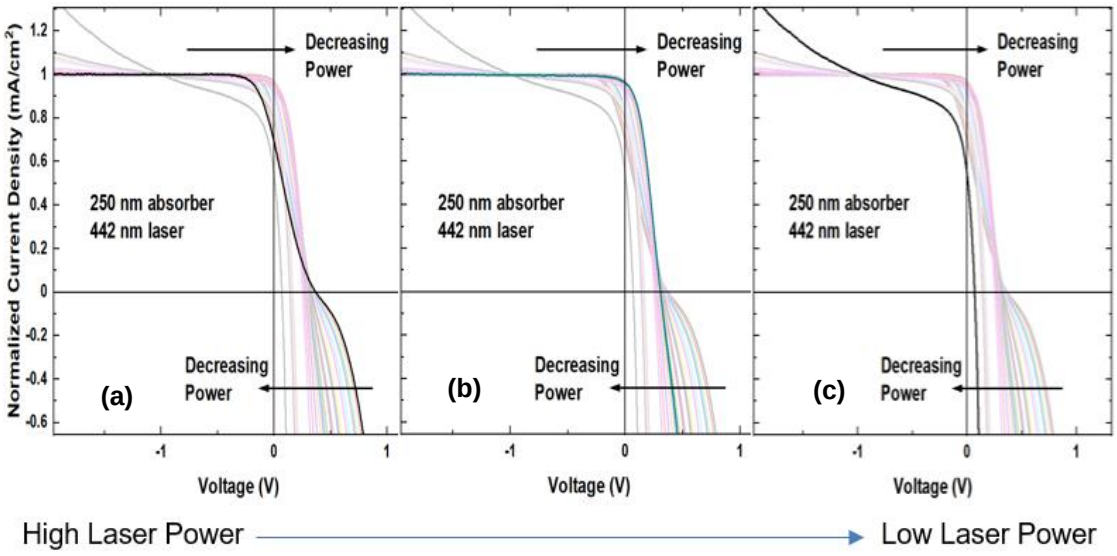

Figure 6. 7. Normalized current density-voltage measurements of the 250 nm InGaAs absorber device under a 442 nm wavelength laser. Three different laser powers are emphasized to clarify the power dependence. (a) Maximum laser power, (b) Removal of the s-shape at low power, (c) Minimum power, depreciation of J_{sc} as V_{oc} drops too low to facilitate a large solar cell quadrant.

Monochromatic excitation with the 1064 nm laser results in similar *J-V* characteristics, despite relying on electric field acceleration rather than phonon-mediated intervalley scattering to stimulate transfer of carrier between the Γ and L valleys. This indicates that regardless of the specific mechanism, the carriers are facing the same barrier to extraction

when placed in the upper valley of the absorber. For comparison purposes, the 25 nm and 250 nm data for each laser is presented in Figure 6.8.

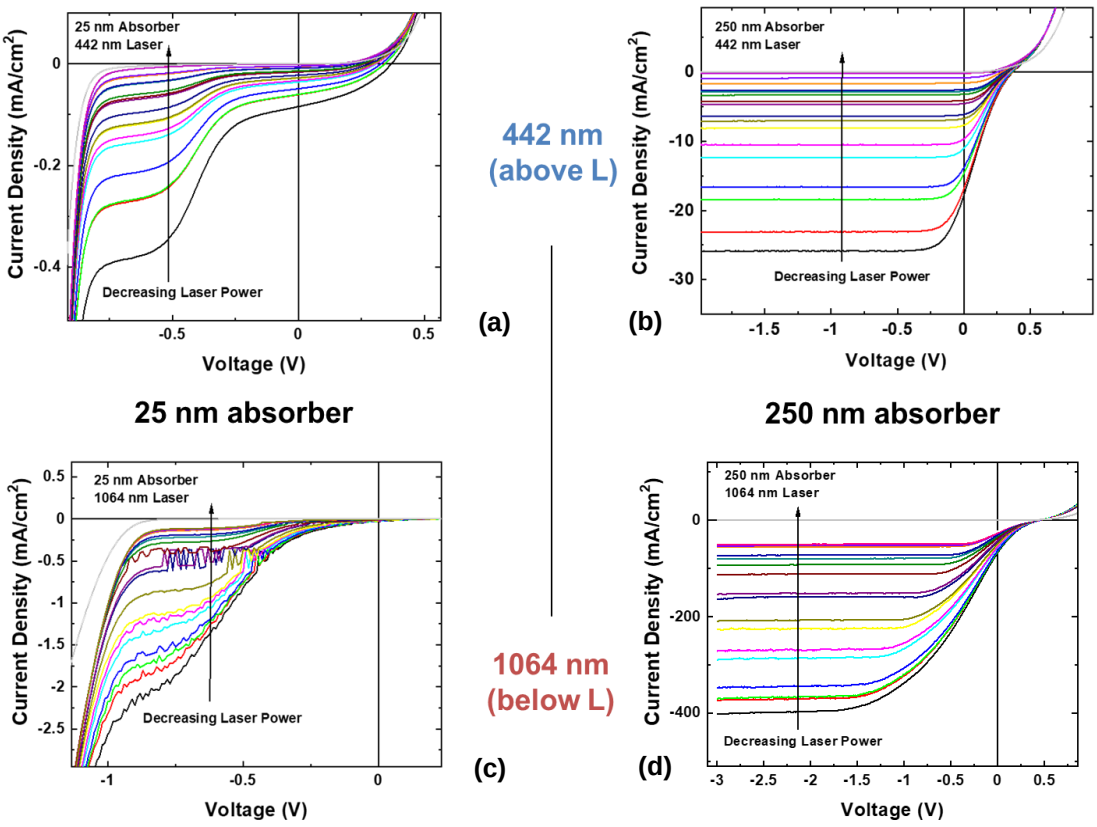

Figure 6. 8. Current density-voltage measurements presented in comparison for the thinnest (25 nm) (a) (c) and thickest (250 nm) (b) (d) absorbers examined under both 442 nm (a) (b) and 1064 nm (c) (d) wavelength lasers.

The primary distinction between the lasers is the higher maximum power of the 1064 nm wavelength laser, which is responsible for the disparity in current density values between the 250 nm absorber figures for each laser. Upon performing the same normalization technique as before, the 250 nm absorber, 1064 nm wavelength case

(Figure 6.9, below) becomes very similar to the 442 nm wavelength case shown in Figure 6.7.

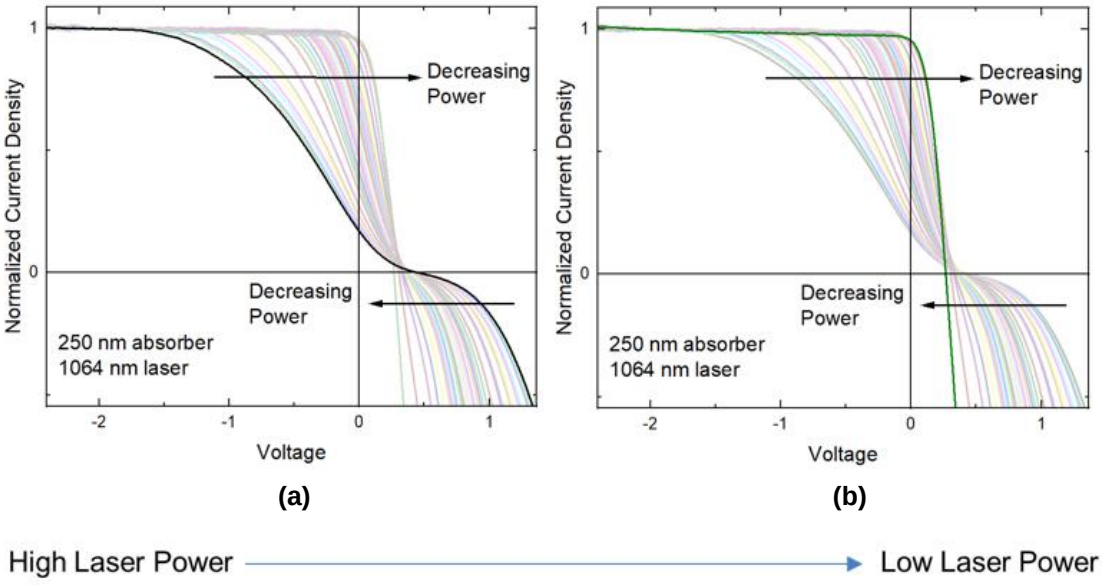

Figure 6. 9. Normalized current density-voltage measurements of the 250 nm InGaAs absorber device under a 1064 nm wavelength laser. Two different laser powers are emphasized to clarify the power dependence, with (a) featuring maximum illumination power and a strong s-shape and (b) featuring a minimum laser power and a more rectangular fill factor.

The evolution of the knee and the open circuit voltage follows the same trend as presented in the 442 nm laser wavelength data (Figure 6.7) despite the different excitation energy. At high power (Figure 6.9(a)), large bias is needed to offset charge accumulation at the interface. But as the power decreases (towards Figure 6.9(b)) the number of generated carriers decreases, and the enhancement of the barrier due to charge accumulation is also reduced. The necessary bias to enable carrier extraction therefore

also decreases as a result. Once again, while the normalization might present the illusion that this results in a useful improvement to fill factor at very low excitation power, the true current density is very low, and this is only compounded by the depreciated open circuit voltage.

6.4. Device Design for a High Illumination Power Study of Electric Field Influence on Hot Carrier Behavior

While the electric field is enhanced in the three thinner absorber devices, this alone does not provide a solution to the extraction difficulties faced by the 250 nm absorber device since despite the field aided scattering of carriers to the satellite valleys is likely enhanced by electric field, these carriers still experience a barrier to extraction between the L-absorber and Γ-extraction barrier; though their *J-V* characteristics shed useful light upon the details of the problem. Indeed, in terms of electronic properties, the severe depreciation of current density in the thinner samples is far from an improvement. Yet, the consistency with which this set of samples engages the twin mechanisms of electric field acceleration and intervalley scattering provides substantial opportunities to probe the details of the electric field acceleration in a way not previously possible.

Therefore, to follow this initial examination, a subsequent round of measurements was conducted [13]. Samples with the 25 nm and 100 nm absorber thickness were processed into devices with a top layer of ITO sputtered on prior to the deposition of the top contact. As a transparent conductive oxide, the ITO serves both as an anti-reflective coating and improve electrical contact with the top of the device. The final structure was 150 nm ITO /20 nm n^+-$In_{0.52}Al_{0.48}As$ /(25 or 100) nm n-$In_{0.53}Ga_{0.47}As$ /1000 nm p^+-$In_{0.52}Al_{0.48}As$ /p-

InP substrate. This enhances the electric field strength not only at the interfaces but across the absorber region also (particularly for the 25 nm device) to examine the effect on the temperature of the carrier distribution. This structure is presented below in Figure 6. 10.

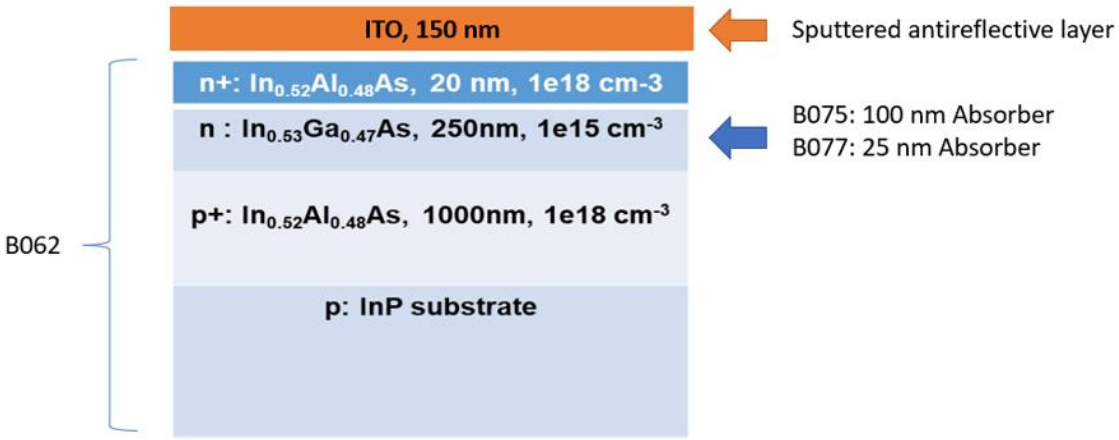

Figure 6. 10. Alterations from the early 250 nm InGaAs device (B062) are illustrated. As before, the device is grown by molecular beam epitaxy and processed into a measurable device. Now a sputtering step is added to deposit the ITO layer, and the absorber thickness is adjusted during epitaxy.

Figure 6.11 (a) below shows NRL Multibands ® simulations of the electric field as a function of depth for both the 25 nm (dashed lines) and 100 nm (full lines) absorber thickness samples, then demonstrates the modification to the electric field caused by an external applied bias. When in reverse bias, the field across the absorber is enhanced. In contrast, applying a sufficiently large forward bias can cause the field to substantially decrease across the absorber region. The interfacial spikes, stemming from the precision of molecular beam epitaxy in both the quality of the interface and the calibration of the doping densities specified in Figure 6.10, are limited in spatial extension, but that

localized field is very large and cannot be eliminated within the range of voltages where these devices operate as solar cells. Figure 6.4(a) indicates under 1 Sun illumination greater than +0.5 V external bias is beyond the solar cell regime for all absorber thicknesses discussed in this chapter, and Figure 6.11(a) demonstrates that +1.25 V is insufficient to fully eliminate the field produced by the doping profile.

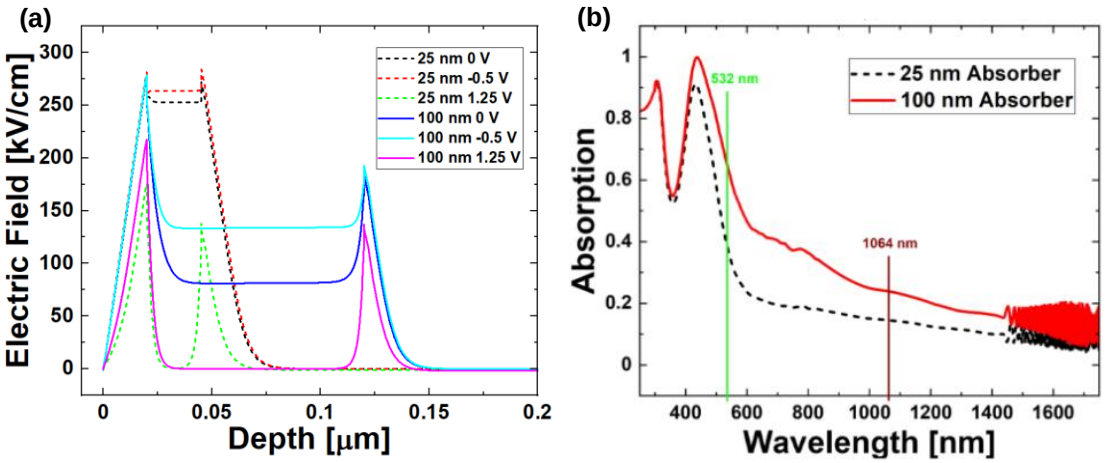

Figure 6. 11. (a) Electric field calculations as a function of depth, performed in NRL Multibands ® at a representative selection of biases for a n+-InAlAs/n-InGaAs/p+-InAlAs/p-InP structure. (b) Transfer matrix calculations for the ITO/n+-InAlAs/n-InGaAs layers for the two absorber thicknesses, presenting the absorption as a function of the wavelength. [12,14] [Reproduced from: *Dorman, Kyle R., et al. "Electric Field and Its Effect on Hot Carriers in InGaAs Valley Photovoltaic Devices." IEEE Journal of Photovoltaics 12, no. 5 (2022): 1175-183.*] [13]

Of central importance to this study is that altering the absorber thickness maintains the material properties and has minimal influence on the interface energy alignments, but decreasing the absorber thickness to a quarter of the size results in more than double the

electric field strength. This enables specific probing of the electric field's role as one of the mechanisms supporting hot carrier behavior. The other major alteration is the absorptivity of the structure, which may be determined and accounted for via transfer matrix calculations. This resulted in Figure 6.11(b), which demonstrates the absorption at each wavelength for the 25 and 100 nm absorber layers, with specific focus on the laser wavelengths that will be employed in this study. Under 532 nm excitation, absorption is much higher than with the 1064 nm wavelength illumination. And the 25 nm absorber thickness device has lower absorption than the 100 nm absorber thickness device under both laser energies. While accounting for this difference after measurement resulted in differing absorbed power ranges in the analyzed data to be presented in this chapter, the benefit of fully accounting for the absorption changes in the presented data is that the only systematic difference unaccounted for between the two devices is the electric field strength, allowing examination of the precise influence of the electric field in detail [13].

The lasers were selected based upon power range and which parts of the conduction band the associated photon energies could excite carriers to. The 532 nm wavelength laser provides excitation above both the L and X valley energies, replacing the 442 nm wavelength laser in that role, and features a greatly expanded range of illumination powers compared to what the 442 nm wavelength laser can provide. The 1064 nm wavelength laser reprises the role of below upper valley excitation, probing the electric field acceleration and not the intervalley phonon scattering. In contrast, the 532 nm wavelength illumination case provides sufficient energy to carriers to reach upper valleys

by intervalley phonon scattering, but the electrical and optical behavior of the sample is not necessarily unaffected by the strength of the electric field.

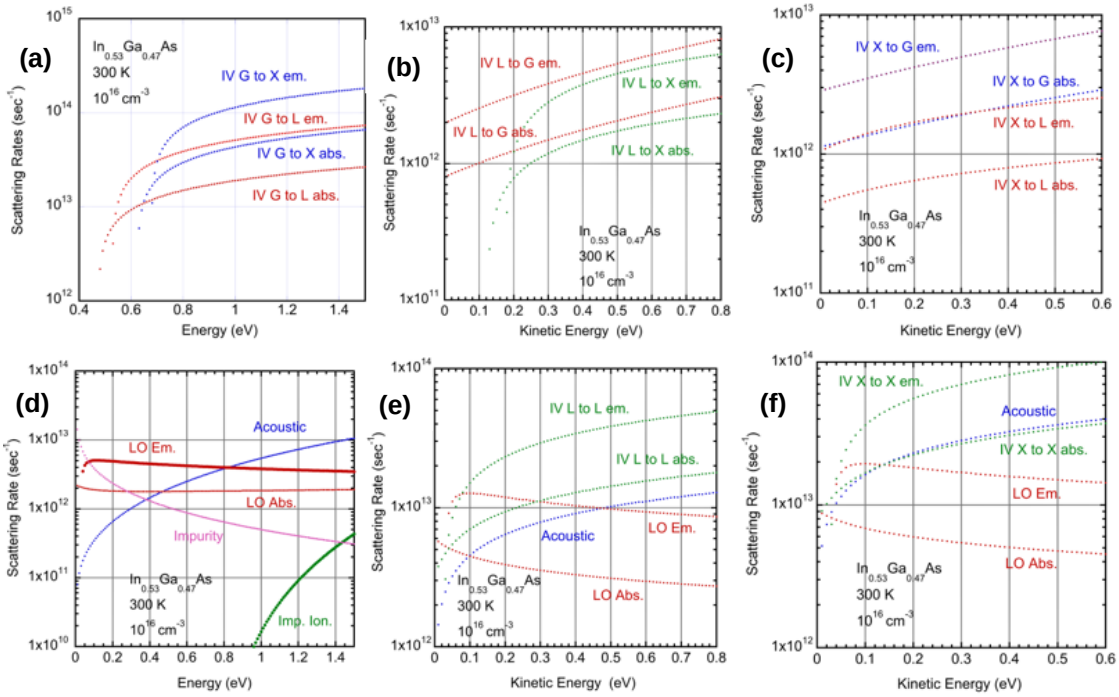

Figure 6. 12. Scattering rate calculations from Prof. Ferry at Arizona State University for $In_{0.53}Ga_{0.47}As$ at room temperature, regarding (a) intervalley transitions from the Γ valley, (b) intervalley transitions from the L valley, (c) intervalley transitions from the X valley, (d) other major scattering rates in the material, and lastly (e) L to L and (f) X to X transitions between symmetrical upper valleys with the same energy but different momentum orientations.

At this time, a better numerical grasp of the scattering rates is beneficial for this study into the intervalley mechanisms. As Figure 6.12 below illustrates through ensemble Monte Carlo simulations for room temperature $In_{0.53}Ga_{0.47}As$, provided by Professor D. K. Ferry at Arizona State University, the intervalley scattering rates depend on the energy

the carriers possess, here presented as energy above the conduction band edge (Γ valley). Figure 6.12(a), (b), and (c) examine the intervalley scattering rates between the three accessible metastable valleys of the conduction band of InGaAs, examining transitions away from Γ, L and X respectively, and in order of energy level. For a hot electron, either emission or absorption of an intervalley phonon may provide the momentum for intervalley transfer, with absorption facilitating slightly lower energy carriers in the transition, but consistently occurring at a slower rate. Figure 6.12 (a) also demonstrates that the scattering rates away from Γ are on average an order of magnitude greater than the corresponding return from the upper valley to the Γ valley (as shown in Figure 6.12(b) and Figure 6.12(c)), and those rates outpace transitions between L and X in InGaAs.

Figure 6.12(d) demonstrates the thermalization inducing scattering rates, which remain below the rates of intervalley scattering from the Γ valley. Of these, the most concerning are the longitudinal optical (LO) phonon scattering rates, which are involved in the Frohlich interaction and subsequent Klemens or Ridley interaction pathway that dominates thermalization processes in high quality III-V semiconductor materials. [15]. Figure 6.12(e) and Figure 6.12(f) place these thermalization rates against the final category of scattering rates – zone edge LA phonon mediated transitions between energetically equivalent but differently oriented in momentum upper valleys (L-to-L or X-to-X) [11, 16]. Unlike the Γ-valley at the center of the Brouillon zone, the upper L and X valleys have multiple momentum orientations according to the crystal symmetry, making these interactions viable. Emission of such phonons is the dominant scattering rate for carriers in the L- or X-valleys, more favorable than return to the Γ valley by an order of magnitude, and exceeding the competing thermalization given the carriers in

question possess a minimum amount of kinetic energy, as Figure 6.12(e) and Figure 6.12(f) demonstrate.

In summary, Figure 6.12 explains why intervalley scattering is so dominant in this material, and what preferentially happens to carriers instead of the thermalization interactions. For the case of 532 nm wavelength illumination, the resultant high energy carriers would be overwhelmingly likely to not immediately thermalize. Including both Γ-to-L and Γ-to-X transitions and comparing to LO phonon emission, a population of such high energy carriers would result in transfer of ~75% of carriers to the X valley, ~24% to the L valley, and <1% to the conduction band edge as a result of undergoing a single scattering processes. Preference then falls to L-to-L and X-to-X phonon emission, thermalizing in the upper valleys towards the bottom of the valley in question. This is a far slower thermalization process than return to the band edge, amounting to ~24 meV loss per L-to-L zone edge emission [11] rather than ~450 meV for descending from L to Γ (as shown in Figure 6.4(b)). Given that even for the 250 nm absorber thickness it should take less than 3 ps for carriers to exit the absorber material, this altered thermalization pathway has potential to facilitate creation of a hot carrier device [11].

Consideration of the behavior of carriers excited by 1064 nm wavelength laser light requires understanding of the influence of the electric field strength on the valley occupancy, which is provided in Figure 6.13 as a calculation for a 250 nm InGaAs layer. The available data is more limited than the well studied scattering rate properties, and the applicability does not fully translate to thinner absorber layers, but an approximation may be made.

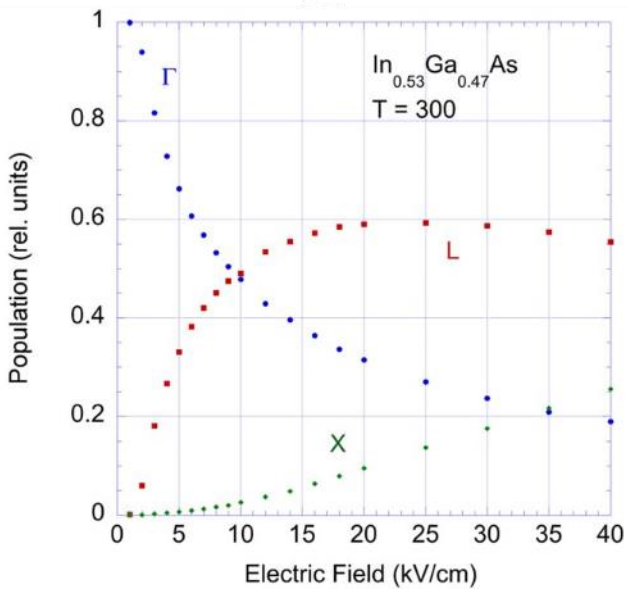

Figure 6. 13. Relative population of the three valleys of the conduction band of InGaAs as a function of electric field. [Reproduced from: *Ferry, D. K. "In Search of a True Hot Carrier Solar Cell." Semiconductor Science and Technology 34, no. 4 (2019): 44001.*] [9]

The unbiased field across the absorber for the 100 nm device is ~70 kV/cm, as seen in Figure 6.11(a), and based on simplistic projection of Figure 6.13 this suggests a plausible 10% Γ valley occupancy due to the influence of the field, with the rest of the carriers evenly split amongst the L and X valleys. The substantially stronger field in the 25 nm absorber device (~250 kV/cm) can be expected to push this farther towards the high energy valleys. While this proportionality is unlikely to be fully accurate for the real 100 nm and 25 nm absorber thickness devices, it indicates that the majority of the carrier population is transfered from the conduction band edge to the upper valleys by the electric field.

A final point to note, in consideration of the practical operation of a hot carrier solar cell, is that such a device would operate in forward bias at the maximum power point. As a hot carrier solar cell under the present design paradigm features enhanced photovoltage, desired to be in excess of the bandgap, this forward bias is unlikely to be negligible in future devices. The design of the dopant profile and the resultant internal field thus must account for a large depreciation of the field across the absorber region as demonstrated in Figure 6.11(a).

The importance of the electric field-aided scattering stems from the potential offset at the top of the device structure, featured in Figure 6.4(b). The electric field acceleration provides a means to retain a large portion of the photocurrent that would otherwise be trapped at the interface. While studies of alternative extraction pathways were a focus in Chapter 5, and this study instead chooses to focus upon the increasingly well understood proof-of-concept structure with only the small modifications indicated in Figure 6.10 so as to better explore the intervalley mechanisms, the central issue for future hot carrier solar cells must be kept in mind. The primary importance of the electric field-induced intervalley transfer as identified to this point is averting major photocurrent losses due to the higher photovoltage through energy selective contacts focused on the upper valleys. Without this mechanism, many carriers excited by the solar spectrum would remain trapped at the conduction band edge in the absence of an extraction pathway. This is a necessity for decoupling the electronic and optical behavior sufficiently to overcome the single gap limit [1, 2, 9].

Selection of which upper valley from which to extract from is therefore of paramount importance for design of intervalley-based hot carrier devices [8, 17]. The practical

relevance of the solar spectrum fixes much of the intervalley phonon scattering concerns into the realm of material selection due to the dependence on carrier energies seen throughout Figure 6.12. But given the slow transitions between L and X valleys, as Figure 6.12(b) and Figure 6.12(c) illustrate, placing carriers into the desired valley preferentially is efficient. As Figure 6.13 demonstrates, electric field acceleration's shifting of valley occupancy therefore becomes an important means of control, thanks to having a substantial impact which can be modified through the dopant profile during the growth process.

A better understanding of this mechanism is likely to yield substantial benefits for future devices. And if momentum conditions across the interface [18] are relaxed due to interfacial design, then a semi-infinite energy filter courtesy of a wide bandgap top layer or Schottky barrier may raise the possibility of extracting carriers from both upper valleys at once [19, 20]. This would involve setting the photovoltage to the lower energy of the L or X valleys, but the increase in photocurrent could be a net benefit.

6.5. Power Dependent Current Density-Voltage Measurements

To determine the influence of the electric field strength on the electronic properties of the devices, as well as to discern the most informative external voltages for investigation in bias-influenced photoluminescence measurements, a set of current density-voltage *(J-V)* measurements were performed. All measurements were performed at room temperature, and may be discussed with according relevance to the room temperature simulations presented in Section 6.4. Both the 25 nm absorber and 100 nm absorber devices were examined with this technique under both the 532 nm and 1064 nm

wavelength lasers. The results of these illumination power-dependent measurements are presented in Figure 6.14.

As previously discussed in Chapter 4, the 250 nm absorber thickness device featured limited solar cell properties due to poor extraction [8]. And as discussed in Chapter 5, the extraction issues are associated with the potential offset at the top barrier, schematically illustrated in Figure 6.4(b). Aside from the absorber thickness and the ITO coating on the top (n^+) side of the device, as Figure 6.10 demonstrates, the device is unchanged at the top n^+-InAlAs/InGaAs interface, which results in familiar depreciation of the fourth (solar cell) quadrant of the current density-voltage characteristic, presented in Figure 6.14.

Figure 6.14 (b) and (d) show the 100 nm absorber thickness device data, and as anticipated by the absorptivity curves in Figure 6.11(b), the current densities exceed the corresponding J-V curves for the two laser wavelengths illuminating the 25 nm absorber thickness device (Figure 6.14 (a) and (c)). For both devices, the poor fill factor and small size of the solar cell regime is associated with the curve inflecting due to the aforementioned top interface barrier. The voltage dependence of the inflection notably changes with power density, with higher incident powers producing more carriers that accumulate at the potential offset at the top interface, enhancing the barrier height due to accumulation of electrons in the region. Such enhancement of this potential barrier will be overcome at larger negative bias, which matches the trend visible in Figure 6.14.

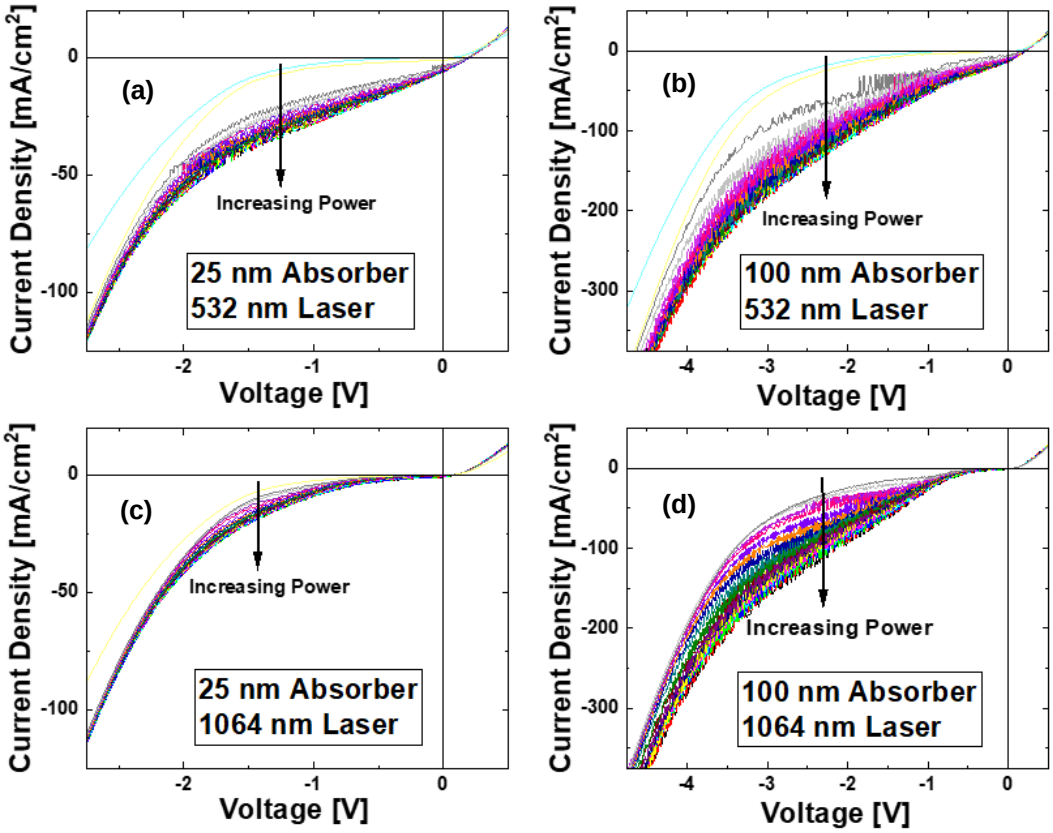

Figure 6. 14. Power dependent current density-voltage measurements of 25 nm (a, c) and 100 nm (b, d) InGaAs absorber devices under 1064 nm (c, d) and 532 nm (a, b) laser excitation. [Reproduced from: *Dorman, Kyle R., et al. "Electric Field and Its Effect on Hot Carriers in InGaAs Valley Photovoltaic Devices." IEEE Journal of Photovoltaics 12, no. 5 (2022): 1175-183.*] [13]

The inflection cannot be tracked indefinitely towards farther reverse bias, as -2.5 V for the 25 nm absorber thickness or -4.5 V for the 100 nm absorber thickness will result in breakdown conditions. This is Zener breakdown, with enormous current density enhancement occurring due to the high electric field and the thin size of the layers facilitating direct tunneling that naturally obviates the influence of the barrier and thus,

the inflection. Given the internal electric field for the 25 nm device begins at ~250 kV/cm, application of a reverse bias that enhances the field further is indeed expected to cause breakdown conditions at a smaller external bias than the 100 nm device, which begins with less than half the electric field strength (see Figure 6.11(a)).

Due to differences in absorptivity for each laser wavelength and absorber thickness combination, while the lasers provided the same incident illumination power, the transfer matrix calculations shown in Figure 6.11(b) must be utilized to determine the more usefully comparative *absorbed* power. Also accounting for the spot size of the lasers, power dependent data from here onwards will be presented in terms of the absorbed power density. Performing this calculation, and then extracting the open circuit voltage (V_{oc}) and short circuit current density (J_{sc}) from each of the current density-voltage curves in Figure 6.13, results in Figure 6.14 for the 1064 nm wavelength laser cases and Figure 6.15 for the 532 nm wavelength laser. The range of absorbed power densities that the 1064 nm wavelength laser provided in this study was more limited than the 532 nm wavelength laser, and the different absorber thicknesses also resulted in different maximum absorbed power densities for each device. The data is presented in its entirety, rather than limiting only to the small range that is fully comparable. Therefore, as a visual guide, a magenta shaded region in the 532 nm wavelength laser data (Figure 6.16) highlights the absorbed power densities that are presented in the 1064 nm wavelength laser data (Figure 6.15) as a visual guide, a convention that will be continued throughout the photoluminescence analysis later in this chapter.

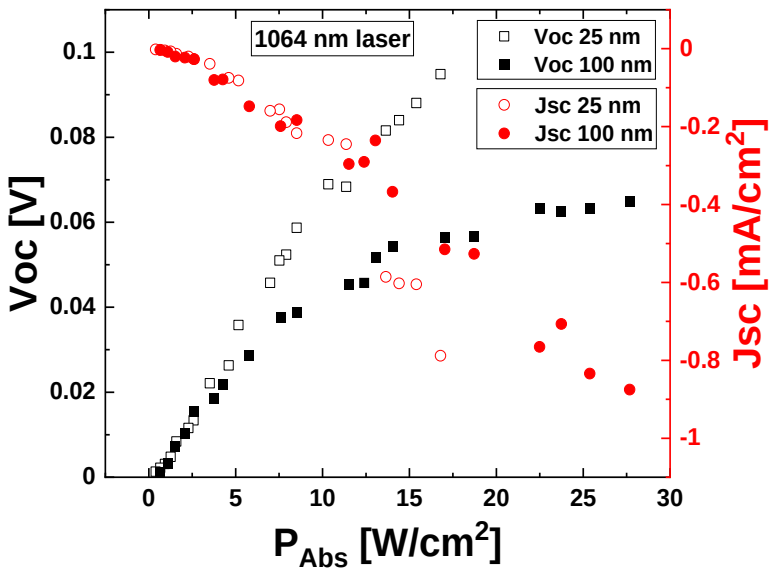

Figure 6. 15. V_{oc} (black) and J_{sc} (red) as a function of absorbed illumination power density, for the 25 nm (open) and 100 nm (filled) absorber structures, under 1064 nm laser illumination. [Reproduced from: *Dorman, Kyle R., et al. "Electric Field and Its Effect on Hot Carriers in InGaAs Valley Photovoltaic Devices." IEEE Journal of Photovoltaics 12, no. 5 (2022): 1175-183.*] [13]

From the 1064 nm laser data in Figure 6.15, an immediate difference is visible between the two absorber thicknesses in the V_{oc}. Where the ideal diode equation would predict logarithmic dependence on power for the V_{oc}, and this is borne out in the 100 nm absorber thickness case, the 25 nm absorber thickness device remains in an approximately linear regime throughout the span of absorbed power densities measured. The 25 nm absorber, 1064 nm laser wavelength is the most abbreviated in that regard, and the curvature suggests that this is indeed the beginning of a logarithmic curve. The J_{sc} is more linear for both devices, as expected for a diode despite the limited extraction seen in the full curves of Figure 6.14 (a) and (c). The V_{oc} and J_{sc} set out the maximum limits of the solar

cell behavior, and those limits are well below the current densities swiftly achieved in reverse bias, while the V_{oc} is far below the desired goal of exceeding the bandgap of InGaAs (~0.75 eV). Of most note here however is that while J_{sc} is comparable for both thicknesses, V_{oc} is larger for the 25 nm absorber thickness device than for the 100 nm variant. As the absorption is normalized out of the x-axis of Figure 6.15, and this is high quality InGaAs and not subject to any substantial carrier transport issues, this means there is an improvement that may be attributed to the substantial increase in electric field strength.

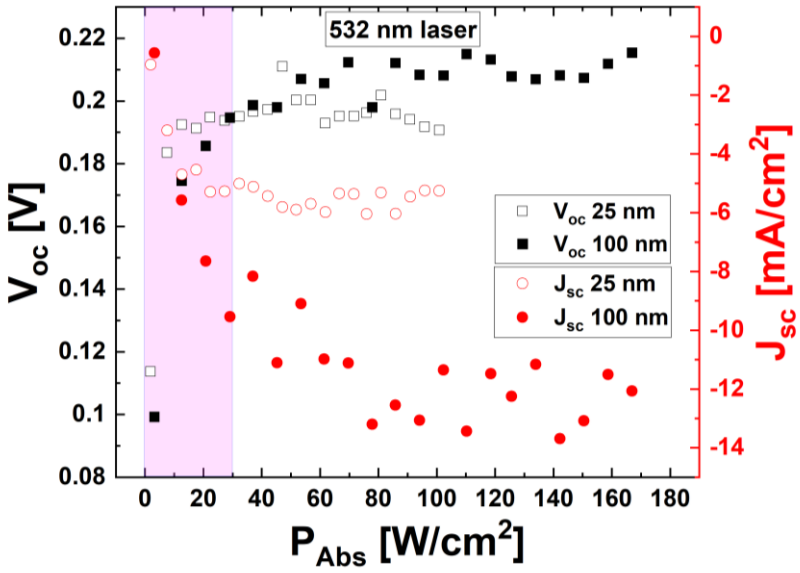

Figure 6. 16. *Voc* (black) and *Jsc* (red) as a function of absorbed illumination power density, for the 25 nm (open) and 100 nm (filled) absorber structures, under 532 nm laser illumination [13]. For comparison purposes, the magenta shaded region highlights the absorbed power density range featured in Figure 6.15.

The 532 nm laser data is presented in Figure 6.16, and reveals that while in the lower power regime (magenta) to which the 1064 nm laser data is matched the similarities are quite strong (note the V_{oc} for the 25 nm data is briefly larger than the 100 nm and the J_{sc} values are initially very close), this changes as higher absorbed power densities are reached. Both V_{oc} and J_{sc} plateau, and upon doing so both V_{oc} and J_{sc} for the 100 nm absorber thickness device exceeds the 25 nm case. The V_{oc} difference is small, and may simply be linked to improved access to the solar cell quadrant via heightened *Jsc* in the 25 nm case, but the question of the J_{sc} is slightly more complex.

First, that the J_{sc} plateaus with increasing power indicates nonidealities in the extraction mechanism, in the sense that there appears to be a maximum current density when no external bias is applied. This is indicative of a process that does not scale with increasing carrier density, in contrast to the behavior Figure 6.14(b) reveals in reverse bias past the inflection, which is the expected behavior for surpassing a potential offset. Examining the power dependence, it appears that the electric field begins to have a substantial impact outside of the magenta-shaded power regime. This is the opposite of the anticipated trend, as the field may be expected to improve the extraction rather than diminish it. However, the field accelerates carriers across the absorber thickness, and the quadrupled absorber thickness has an average field strength only reduced by a factor of three as shown in Figure 6.11(a). There is much still to understand about efficient extraction from upper valleys [18], so while this cannot be confidently stated to result in the J_{sc} difference between the thicknesses, it is a plausible contributing factor for future study. It is also noteworthy that electric field strength differences will produce stronger band bending in the 25 nm absorber device at the top interface than will occur in the 100 nm absorber

device. Given the alignment shown in Figure 6.11(b), this will increase the potential offset, with mitigating effects on the extraction.

By comparison of Figure 6.15 and Figure 6.16, we examine the influence of the laser wavelength. In both cases, the V_{oc} remains below the enhanced photovoltage desired for a fully operational hot carrier solar cell with an InGaAs absorber, and the J_{sc} remains well below the values Figure 6.14 reveals the device is capable of in reverse bias past the inflection. Comparing equal absorbed power densities, the 1064 nm laser results in substantially less extraction than the 532 nm laser. The low overall value of both is tied to the known inefficiencies of upper valley extraction in this device [8, 14], while the stronger extraction caused by above valley energy laser light relates to the scattering rates shown in Figure 6.12 compared to the impact of the electric field (Figure 6.13). As was discussed in Section 6.4, current calculations of the electric field's influence (Figure 6.13) do not predict it favors upper valley occupation to the extent of the intervalley phonon scattering under the 532 nm laser light. And unlike the 1064 nm laser case which *does not* benefit from the high Γ-valley-to-upper-valley scattering rates, the 532 nm laser light *also* benefits from the presence of the electric field.

6.6. Photoluminescence Analysis

Power dependent photoluminescence measurements were performed at multiple applied biases, so as to further modify the electric field strength and probe the influence of the electric field as thoroughly as was viable with the available equipment. Based upon the 25 nm and 100 nm absorber thickness's current density-voltage curves in Figure 6.14, the applied biases were chosen to examine the regimes of extraction. The selected

external biases were: in forward bias past the photovoltaic operating regime (1 V), at V_{oc} as specified by the values extracted from the *J-V* curves (see Figure 6.15 and Figure 6.16), with a fixed 0 V applied bias, in reverse bias (-1 V and additionally -2 V bias for the 100 nm absorber, 532 nm laser case), and lastly in the Zener breakdown regime (-2.5 V for the 25 nm absorber, -4.5 V for the 100 nm absorber).

Analysis of the photoluminescence peak produced by the InGaAs absorber layer is presented in Figures 6.17 through 6.20, featuring the results for both the 1064 nm and 532 nm laser wavelengths upon both absorber thickness structures. The top of the Figures indicates the estimated 2-D carrier concentration, based upon the absorbed power density and a 6 μs timescale for recombination in lightly doped $In_{0.53}Ga_{0.47}As$ [21], to help guide the discussion with regards to the phonon bottleneck mechanism of hot carrier behavior, which is known to be power dependent as a result of carrier concentration [7, 22, 23]. As with the electronic measurements in Section 6.5 and the simulations discussed in Section 6.4, the optical measurements presented here were performed at room temperature.

Figure 6.17 shows the power dependence of the peak intensity. The initial point to emphasize is the bias dependence. The bias dependence is stronger for certain laser and device configurations than others, however the clear overall trend is that in reverse bias the peak intensity is smaller than in unbiased and forward bias conditions. While the 25 nm absorber thickness in both laser cases has a weaker dependence, and in the 1064 nm laser cases the biases are clustered more closely together, the same relation exists. This is in agreement with the *J-V* curves (Figure 6.14) and the calculated electric field dependence (Figure 6.11(a)). The photoluminescence spectrum is produced by photon-emitting recombination of carriers in the Γ valley, and hence a photoluminescence

intensity is inversely proportional to the extraction, and further mitigated by an electric field accelerating carriers to upper valleys. As such, as the external bias proceeds from forward to reverse bias, from mitigating to enhancing the internal field produced by the doping profile, the peak photoluminescence intensity shown in Figure 6.17 decreases accordingly. This is evidenced most strongly in the Zener effect regime bias for the 100 nm absorber thickness cases, where the drop in intensity is stark due to the rampant direct tunneling removing carriers from the absorber layer with haste.

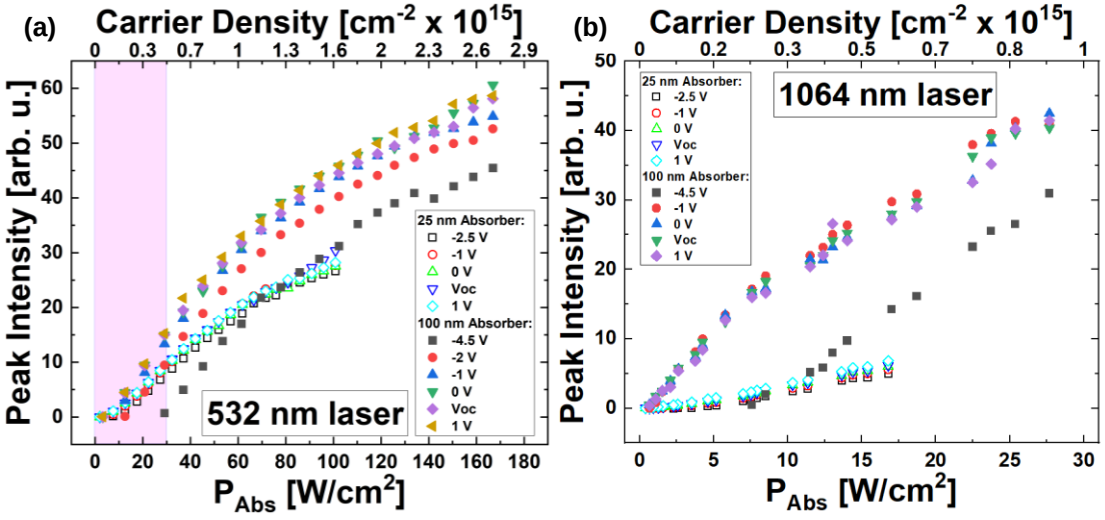

Figure 6. 17. The peak intensity of the photoluminescence spectrum as a function of absorbed illumination power density, for the 25 nm (open) and 100 nm (filled) absorber structures, under (a) 532 nm and (b) 1064 nm laser illumination. The magenta shaded region in (a) highlights the absorbed power density range in (b). [Reproduced from: *Dorman, Kyle R., et al. "Electric Field and Its Effect on Hot Carriers in InGaAs Valley Photovoltaic Devices." IEEE Journal of Photovoltaics 12, no. 5 (2022): 1175-183.*] [13]

Closer inspection of the 532 nm laser data (Figure 6.17(a)) with the 1064 nm laser data (Figure 6.17(b)) in the regime of comparable absorbed power densities (shaded magenta), the intensities are quite similar for the 25 nm absorber data. In contrast, the 1064 nm laser data's 100 nm absorber branch begins to overtake the 532 nm laser's equivalent data points. While the dependence on the external bias is more substantial for the 100 nm devices, with the impact of the -4.5 V bias for Zener breakdown clearly visible, for the other applied biases there is a much clearer separation under 532 nm laser light. The -4.5 V bias excepted, the 25 nm absorber device features weaker photoluminescence than the 100 nm device under both lasers, across all other applied biases. In the context of Figure 6.16 this cannot be fully explained by extraction from the junction decreasing the intensity, as the 100 nm absorber device exceeds the electronic behavior of the 25 nm device at high absorbed power densities.

As the power dependence shown in Figure 6.17 diverges from linearity at higher absorbed powers densities, it is worthwhile to determine what recombination mechanisms are dominant. Interface-aided and Auger recombination are candidates to become more significant at higher illumination power densities as the carrier density rises, as opposed to radiative recombination which relates linearly to power. Trap-assisted recombination is a one carrier process (n), radiative recombination requires two carriers (n^2), and auger requires three (n^3). The integrated intensity of the photoluminescence stems from the radiative recombination rate, and rewriting the recombination relation in terms of the n^2 term results in Equation 6.1:

$$P_{Abs} = A\,(Int_{PL})^{1/2} + B\,Int_{PL} + C\,(Int_{PL})^{3/2} \tag{6.1}$$

Where A, B and C are constants, and Int_{PL} is the integrated intensity of the photoluminescence peak. Inverted so as to plot the integrated intensity as a function of power, results in a simple power law of the form $y = m\,x^k$ where k is then the slope of the log-log plot in Figure 6.18. The value of k indicates which recombination process is dominant, hence $k = 2$ indicates trap-assisted, $k = 1$ indicates radiative recombination, and $k = 2/3$ indicates Auger recombination [24].

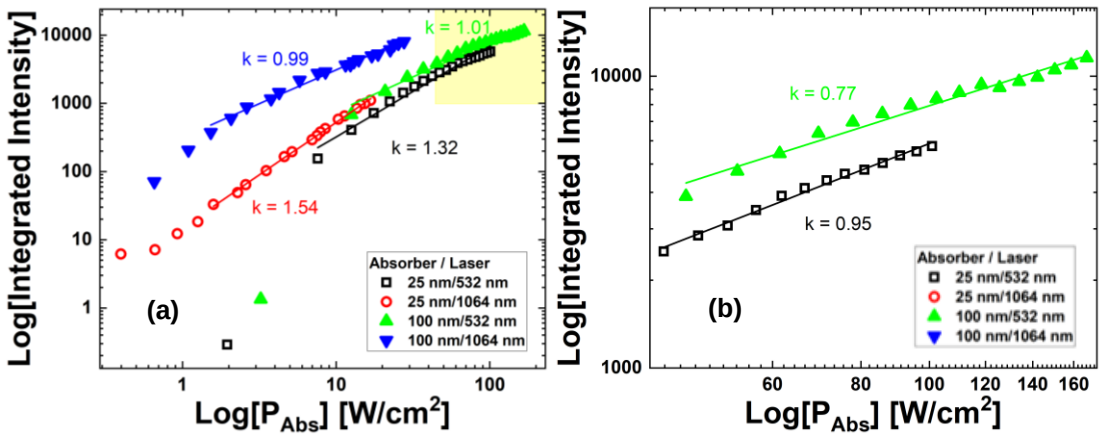

Figure 6. 18. The logarithm of the integrated intensity (at 0 V applied bias) as a function of the logarithm of the absorbed power density for all absorber thickness and laser wavelength combinations. The slope of each plot is given as k, whose inverse relates to exponent of Equation 6.1. The yellow shaded region of (a) highlights the region plotted with better visibility as (b), which is a region where curvature of the slope results in a different k at high power.

Figure 6.18 (a) indicates that across the lower power densities absorbed from the 1064 nm laser (highlighted in magenta in Figure 6.17 (a)) the major influence is radiative recombination, with more trapping of carriers occurring for the 25 nm absorber thickness

device ($1 < k < 2$). Analysis of the higher power regime is strongly indicative of enhanced Auger recombination ($k < 1$) as the carrier concentration continues to increase, especially in the 100 nm absorber, 532 nm laser case. As Auger becomes significant and the power dependence becomes nonlinear, the differences in intensity should less be associated with the potential influence of the electric field, and more with non-radiative recombination.

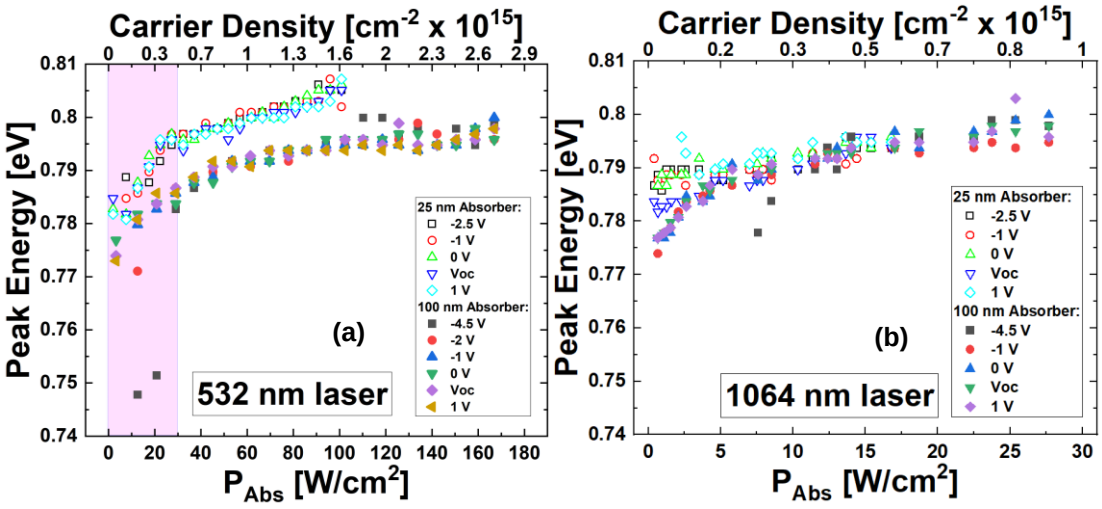

Figure 6. 19. The peak energy of the photoluminescence spectrum as a function of absorbed illumination power density, for the 25 nm (open) and 100 nm (filled) absorber samples, under (a) 532 nm and (b) 1064 nm laser illumination. The magenta shaded region in (a) highlights the absorbed power density range in (b). [Reproduced from: *Dorman, Kyle R., et al. "Electric Field and Its Effect on Hot Carriers in InGaAs Valley Photovoltaic Devices." IEEE Journal of Photovoltaics 12, no. 5 (2022): 1175-183.*] [13]

The energy of the photoluminescence peak is analyzed in Figure 6.19, and the bias dependence seen in the intensity (Figure 6.17) is not observed here. A shift in the peak

energy can be seen in the 532 nm laser data in Figure 6.19 (a), and comparing the energies from Figure 6.19 (b) at matched absorbed power densities (shaded magenta) reveals that both 1064 nm laser wavelength cases undergo a similar shift to that of the 25 nm absorber, 532 nm laser combination. As the shift occurs with increasing power, there is the possibility of lattice heating. However, in III-V crystals increased temperature is associated with a decreased bandgap, and consequently a redshift in the peak of the photoluminescence. A blueshift is more plausibly the result of carrier accumulation at the interface and the resultant electric field, although this does not provide an explanation for the greater peak energy of the 25 nm absorber sample under the 532 nm laser.

Hot carrier behavior should also be considered a potential cause, given the intervalley mechanisms present in these samples discussed in Section 6.4 and the evidence of hot carrier behavior in very similar devices examined in Section 6.3 and Chapter 4. The peak energy of a carrier distribution will increase if the temperature that describes the distribution increases. Should the hot carrier temperature extracted from the photoluminescence be hotter for the 25 nm than the 100 nm absorber device, then this would be a more complete explanation for the blueshift in Figure 6.19.

As this is a simple bulk device structure (Figure 6.10) and examination of the peak for the InGaAs absorber layer with photoluminescence techniques is not complicated by additional overlapping spectral features, the temperature of the carrier distribution in the Γ valley of the absorber can be determined from the slope of the natural logarithm of the high energy tail of the photoluminescence spectrum [8]. This result is given as given as the difference from the lattice temperature, ΔT, in Figure 6.20. The temperature of the upper valleys cannot be directly determined via photoluminescence, though calculations

[9, 11] indicate that a hot carrier distribution seen in the Γ valley in such a valley photovoltaic device is the result of a much higher temperature in the upper valleys.

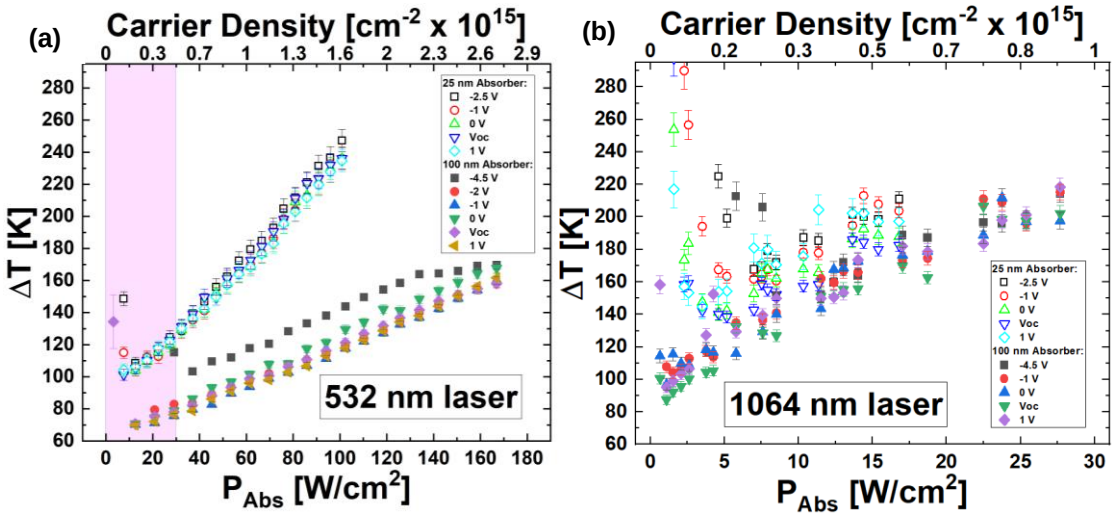

Figure 6. 20. The difference from room temperature (ΔT) of the carrier distribution in the 25 nm (open) or 100 nm (filled) InGaAs absorber heterostructures, as a function of absorbed illumination power density for (a) 532 nm and (b) 1064 nm laser illumination, taken under a set of applied biases. The magenta shaded region in (a) highlights the absorbed power density range in (b). [Reproduced from: *Dorman, Kyle R., et al. "Electric Field and Its Effect on Hot Carriers in InGaAs Valley Photovoltaic Devices." IEEE Journal of Photovoltaics 12, no. 5 (2022): 1175-183.*] [13]

As Figure 6.20 demonstrates a hot carrier temperature ($\Delta T > 0$ K) for each device at both laser wavelengths, it is clear that there is strong hot carrier behavior present. Furthermore, as discussed with regards to Figure 6.19, the hot carrier temperature of the 25 nm absorber device substantially exceeds that of the 100 nm device when illuminated

by the 532 nm laser, and both further increase with power density. This strongly supports the conclusion that the blueshift in peak energy is the result of hot carrier behavior.

There is no apparent systematic result produced by the applied bias, indicating the modulation of the electric field strength through external means is insufficient to cause large divergences in the detectable hot carrier temperature in the Γ valley distribution. As this produces the useful result of hot carrier behavior continuing even at substantial forward bias, this is beneficial for the desired hot carrier solar cell application. However, the consequence is that design of a hot carrier device is very important, as the devices that have been studied at this time cannot be tuned through applied voltage to activate or deactivate hot carrier behavior as might be assumed from the relevance of electric field to the device's operation. There is room for future study on this issue.

The most notable aspect of the carrier temperatures in Figure 2.20 however, is that they demonstrate a power dependence similar but not identical to the phonon bottleneck effect [5, 7]. Low power measurements, both in Section 6.3 and in the study of the 250 nm absorber sample in Chapter 4, provided evidence that this material system did not deactivate the hot carrier temperature as incident illumination power approached zero (though this was not, of course, a claim that these effects could occur without incident light). This was described in terms of power indepence [8]. But with the absorber thickness decreased and the internal electric field from the doping profile enhanced in strength across the abbreviated absorber, there is now good evidence that it is possible for a hot carrier device based upon upper valleys of the band structure can have both the non-zero base hot carrier temperature of valley photovoltaics *and* a power dependence akin to the phonon bottleneck effect.

Linear projection of the power dependence indicates the 25 nm absorber device has a 20 K hotter carrier temperature than the 100 nm device under both lasers in all parts of the power regime save the most signal-to-noise ratio limited low power data for the 1064 nm laser, 25 nm absorber thickness case. This means the device with stronger electric fields features enhanced hot carrier behavior. And comparing the different laser data between Figure 6.20 (a) and (b), the 1064 nm laser results in higher temperatures for both devices within the P_{Abs} matched region, shaded in magenta in Figure 6.20 (a) for clarity. This is evidence that under the condition that all carriers only reach the upper valleys through electric field enhancement, the resulting hot carrier distribution reaches a higher temperature than is produced from the 532 nm laser illumination scenario where many carriers transfer via intervalley phonon scattering. This indicates that the influence of the electric field strength is very beneficial for future hot carrier devices.

An important question that the power dependence of ΔT raises is if this is perhaps a manifestation of the phonon bottleneck, now observed in the same system as the intervalley mechanisms. The phonon bottleneck effect is the result of incident illumination power exciting high energy carriers to the conduction band faster than the rate-limited phonon scattering rates can enable thermalization. The result is a build up of high energy carriers that form a hot carrier distribution, with the correlary that in the absence of an upper valley providing power-independent hot carrier maintenance, the hot carrier behavior requires a minimum photon flux [5, 6, 7].

The limitations of the data for the 25 nm absorber device under 1064 nm illumination prevent examining the power dependence between the two devices in Figure 6.20(b). In Figure 6.20(a) however, the 25 nm absorber results in not merely a warmer projected

minimum temperature, but a stronger power *dependence* than is observed in the 100 nm absorber device. Given the relevance of carrier density to the formation of a phonon bottleneck, the larger J_{sc} values seen for the 100 nm absorber device in Figure 6.16 would be consistent with the proposal that the power dependence functions similar to the phonon bottleneck. Indeed, the 532 nm laser, 100 nm absorber combination has the best extraction and also the lowest hot carrier temperatures and the weakest power dependence. The question of carrier density produced now becomes more relevant than the absorbed power density, so that we may determine whether or not the results shown in Figure 6.20 diverge from the known phonon bottleneck requirements.

A well matched comparison from the scientific literature comes from the work of Hirst *et al.* in the study of a 15 nm $In_{0.53}Ga_{0.47}As$ quantum well with n-type 10^{15} cm^{-3} background doping, and demonstrated bottleneck effects with $>10^{17}$ cm^{-3} carrier density [7]. This was an optical sample rather than a doped device and therefore featured no electric field (neither externally applied nor from a doping profile), excited with a 1064 nm wavelength laser, which ensured the carriers were too low energy for intervalley phonon scattering. Hirst *et al.* [7] did not demonstrate the non-zero low power hot carrier temperature observed in the InGaAs heterostructure devices discussed in this chapter, which is the anticipated result, fully consistent with the understanding of the intervalley mechanisms and hot carrier behavior presented in this dissertation. Transforming the 2-D carrier density shown on the top x-axis of Figure 6.20 into the 3-D carrier density using the respective absorber thicknesses indicates that minimum values of the volumetric carrier density supplied by the lasers in this study exceeded 10^{18} cm^{-3} [13]. Yet while this

is promising, it is not quite sufficient evidence that the power dependence operates via the bottleneck effect.

As discussed in Section 6.4, a major difference introduced by the intervalley mechanisms is moving carriers to other valleys of the conduction band, and this requires due consideration. It should be noted that the prediction of < 1% of carriers excited by 532 nm laser light thermalizing to the conduction band edge (which would suggest a 10^{16} cm^{-3} carrier density insufficient for bottleneck formation) is a simplistic analysis that does not provide an accounting for later return from the upper valley. The non-zero hot carrier temperatures observed in these InGaAs heterostructure devices are the result of such return processes, indicating it is not insubstantial in quantity, especially in a device with such limited extraction from the upper valleys (as seen in the J_{sc} values of Figure 6.15 and Figure 6.16). As such, phonon bottleneck formation is indeed plausible.

The electric field acceleration estimate for the 100 nm absorber case left ~10% of carriers in the Γ valley, without yet accounting for the limited acceleration distance compared the 250 nm absorber thickness used for the estimate, which is anticipated to increase the Γ valley occupancy. Applying this to the calculated volumetric carrier density indicates $>10^{17}$ cm^{-3} is the condition of the Γ valley, which is sufficient to meet phonon bottleneck requirements. With the caveat that the 1064 nm wavelength laser, 25 nm absorber case cannot be reliably estimated in the same fashion at this time in light of available computational and experimental assets and would benefit from future study, the power dependence being the result of formation of a phonon bottleneck is plausible given the available evidence.

6.7. Conclusions

By reducing the absorber thickness, accounting for the modified absorption, and studying the effects of the electric field strength in a set of InGaAs heterostructures, a better understanding of the role of electric field in hot carrier mechanisms was obtained. A stronger electric field was associated with higher hot carrier temperatures, both in the production of larger ΔT when fully responsible for accelerating carriers to the upper valleys in the absence of above valley energy photons, but also notably enhancing base hot carrier temperatures at low absorbed power density.

The course of this investigation also reveals the potential for both a phonon bottleneck to form and for intervalley scattering to support a hot carrier population, simultaneously. The phonon bottleneck effect is a limitation of thermalization at the LO modes to LA modes phonon interactions, and the intervalley mechanisms serve as a limitation through high efficiency of intervalley phonon scattering [15]. These mechanisms are not by necessity in competition, although depending on material properties not all semiconductors have the potential to utilize both means of hot carrier maintenance [22]. Figure 6.20 offers evidence that future hot carrier solar cells based upon both techniques may reap the benefits of both: enhancement of hot carrier behavior with increasing illumination power *and* a non-zero ΔT that does not deactivate when the illumination power is weak. And in a solar cell operating in the more varied conditions outside of a laboratory, as the hot carrier solar cell is intended to after the issues of hot carrier extraction limiting the devices are resolved, this may result in a highly valuable improvement to both performance and reliability.

References

[1] Shockley, William, and Hans J. Queisser. "Detailed Balance Limit of Efficiency of p-n Junction Solar Cells." *Journal of Applied Physics* 32, no. 3 (1961): 510-19.

[2] Ross, Robert T., and Arthur J. Nozik. "Efficiency of Hot-carrier Solar Energy Converters." *Journal of Applied Physics* 53, no. 5 (1982): 3813-818.

[3] Garg, Jivtesh, and Ian R Sellers. "Phonon Linewidths in InAs/AlSb Superlattices Derived from First-principles-application towards Quantum Well Hot Carrier Solar Cells." *Semiconductor Science and Technology* 35, no. 4 (2020): 44001.

[4] Lugli, P., and S. M Goodnick. "Nonequilibrium Longitudinal-optical Phonon Effects in GaAs-AlGaAs Quantum Wells." *Physical Review Letters* 59, no. 6 (1987): 716-19.

[5] Le Bris, A., L. Lombez, S. Laribi, G. Boissier, P. Christol, and J.-F. Guillemoles. "Thermalisation Rate Study of GaSb-based Heterostructures by Continuous Wave Photoluminescence and Their Potential as Hot Carrier Solar Cell Absorbers." *Energy & Environmental Science* 5, no. 3 (2012): 6225-232.

[6] Esmaielpour, Hamidreza, Brandon K. Durant, Kyle R. Dorman, Vincent R. Whiteside, Jivtesh Garg, Tetsuya D. Mishima, Michael B. Santos, Ian R. Sellers, Jean-François Guillemoles, and Daniel Suchet. "Hot Carrier Relaxation and Inhibited Thermalization in Superlattice Heterostructures: The Potential for Phonon Management." *Applied Physics Letters* 118, no. 21 (2021): 213902.

[7] Hirst, Louise C, Michael K Yakes, Christopher G Bailey, Joseph G Tischler, Matthew P Lumb, Maria Gonzalez, Markus F Fuhrer, N. J Ekins-Daukes, and Robert J Walters. "Enhanced Hot-Carrier Effects in InAlAs/InGaAs Quantum Wells." *IEEE Journal of Photovoltaics* 4, no. 6 (2014): 1526-531.

[8] Esmaielpour, Hamidreza, Kyle R. Dorman, David K. Ferry, Tetsuya D. Mishima, Michael B. Santos, Vincent R. Whiteside, and Ian R. Sellers. "Exploiting Intervalley Scattering to Harness Hot Carriers in III–V Solar Cells." *Nature Energy* 5, no. 4 (2020): 336-43.

[9] Ferry, D. K. "In Search of a True Hot Carrier Solar Cell." *Semiconductor Science and Technology* 34, no. 4 (2019): 44001.

[10] Gunn, J. B. "Microwave Oscillations of Current in III-V Semiconductors." *Solid State Communications* 88, no. 11 (1993): 883-86.

[11] Ferry, D. K., S. M. Goodnick, V. R. Whiteside, and I. R. Sellers. "Challenges, Myths, and Opportunities in Hot Carrier Solar Cells." *Journal of Applied Physics* 128, no. 22 (2020): 220903.

[12] Adachi, S. "Optical Dispersion Relations for GaP, GaAs, GaSb, InP, InAs, InSb, $Al_xGa_{1-x}As$, and $In_{1-x}Ga_xAs_yP_{1-y}$." *Journal of Applied Physics* 66, no. 12 (1989): 6030-040.

[13] Dorman, Kyle R., Vincent R. Whiteside, David K. Ferry, Tetsuya D. Mishima, Israa Yusuf, Hamidreza Esmaielpour, Michael B. Santos, and Ian R. Sellers. "Electric Field and Its Effect on Hot Carriers in InGaAs Valley Photovoltaic Devices." *IEEE Journal of Photovoltaics* 12, no. 5 (2022): 1175-183.

[14] Del Villar, I., C. R. Zamarreño, M. Hernaez, P. Sanchez, F. J. Arregui, and I. R. Matias. “Generation of Surface Plasmon Resonance and Lossy Mode Resonance by Thermal Treatment of ITO Thin-Films,” *Optics & Laser Technology* 69, (2015): 1-7.

[15] Ferry, D. K. “Non-Equilibrium Longitudinal Optical Phonons and their Lifetimes.” *Applied Physics Reviews* 8, no. 2 (2021): 021324.

[16] Ferry, David K. *Semiconductors: Bonds and Bands, 2nd ed*., Bristol: IOP Publishing, 2020.

[17] Whiteside, V. R., H. Esmaielpour, T. D. Mishima, K. R. Dorman, M. B. Santos, D. K. Ferry, and I. R. Sellers. "The Role of Intervalley Phonons in Hot Carrier Transfer and Extraction in Type-II InAs/AlAsSb Quantum-Well Solar Cells." *Semiconductor Science and Technology* 34, no. 9 (2019): 94001.

[18] Ferry, David K., Vincent R. Whiteside, and Ian R. Sellers. "Pathways to Hot Carrier Solar Cells." *Journal of Photonics for Energy* 12, no. 2 (2022): 022204.

[19] Konovalov, I., V. Emelianov, and R. Linke. "Hot Carrier Solar Cell with Semi Infinite Energy Filtering." *Solar Energy* 111 (2015): 1-9.

[20] Le Bris, A., and J.-F. Guillemoles. "Hot Carrier Solar Cells: Achievable Efficiency Accounting for Heat Losses in the Absorber and through Contacts." *Applied Physics Letters* 97, no. 11 (2010): 113506.

[21] Ahrenkiel, R. K., R. Ellingson, S. Johnston, and M. Wanlass. "Recombination Lifetime of $In_{0.53}Ga_{0.47}As$ as a Function of Doping Density." *Applied Physics Letters* 72, no. 26 (1998): 3470-472.

[22] Zhang, Yi, Xuguang Jia, Shuang Liu, Kefan Wu, Jiayu Zhang, and Gavin Conibeer. "Explore the Correlation between Intervalley Scattering and Phonon Bottleneck Effect on the Hot Carrier Relaxation in Bulk GaSb and InN for Hot Carrier Solar Cells." *Journal of Applied Physics* 130, no. 20 (2021): 205705.

[23] Rosenwaks, Y., M. C. Hanna, D. H. Levi, D. M. Szmyd, R. K. Ahrenkiel, and A. J. Nozik. "Hot-carrier Cooling in GaAs: Quantum Wells versus Bulk." *Physical Review B: Condensed Matter* 48, no. 19 (1993): 14675-4678.

[24] Riordan, Nathaniel A., Chaturvedi Gogineni, Shane R. Johnson, Xianfeng Lu, Tom Tiedje, Ding Ding, Yong-Hang Zhang, Rafael Fritz, Kolja Kolata, Sangam Chatterjee, Kerstin Volz, and Stephan W. Koch. "Temperature and Pump Power Dependent Photoluminescence Characterization of MBE Grown GaAsBi on GaAs." *Journal of Materials Science: Materials in Electronics* 23, no. 10 (2012): 1799-804.

Conclusion

In this dissertation, the influence of intervalley scattering mechanisms on hot carrier behavior has been investigated through implementation of both electric field-induced scattering and intervalley phonon scattering processes into practical devices. Continuous wave photoluminescence (PL) spectroscopy of bulk InGaAs heterostructure devices has provided robust evidence for hot carrier behavior for the previously unobserved combination of weak illumination intensity and room temperature conditions. The formerly opaque causes of weak power dependence of hot carrier temperature in InAs multi-quantum wells (MQWs) are now explained by hot carrier maintenance through transfer and storage to high energy metastable valleys of the conduction band, a process not dependent on illumination power through either proposed mechanism.

To examine the known temperature dependent Type-II properties of InAs/AlAsSb multi-quantum wells in conjunction with strong intervalley scattering, altered InAs/AlAsSb MQW devices with varied barrier thickness were studied. The electronic properties were greatly improved by altering the top n^+ layer, while current density-voltage (*J*-*V*) measurements provided evidence that the extraction of carriers from intervalley systems was inhibited by barriers to extraction whose subtleties were not yet understood. Through PL spectroscopy, analysis of hot carrier temperatures indicated that there were substantial benefits for hot carrier maintenance via intervalley effects.

As intervalley transfer of carriers is not limited to confined systems, and a move to bulk structures would mitigate limited absorptivity that has hindered previous hot carrier

devices, a more thorough proof of principle for a ‘valley photovoltaic’ approach to maintaining a hot carrier population at enhanced energy was demonstrated in an $In_{0.53}Ga_{0.47}As$ heterostructure. Not only was this result robust with respect to power and temperature dependence, thereby bypassing the primary known hurdles to creating a hot carrier solar cell, PL measurements with above and below valley laser energies both were consistent hot carrier temperatures. This result is most easily and consistently explained by both electric field-aided and intervalley phonon scattering being active in the device and storing the carriers in the same upper valleys.

The primary limitation of the proof-of-concept device was a barrier to carrier extraction, which depreciated the solar cell photovoltaic behavior. To develop these novel hot carrier maintenance techniques into a full-fledged hot carrier solar cell would require substantial work to deconvolute the subtleties of the *J*-*V* response, which was accomplished through study of a series of InGaAs heterostructure devices with altered top n^+ barrier layers. This revealed that momentum conservation can substantially limit real space transfer even between aligned energy levels, necessitating that future hot carrier solar cells based upon intervalley principles account for these limitations through careful design of the n^+ barrier/absorber interface.

Finally, while collaboration with Prof. David K. Ferry at Arizona State University provided a deep understanding of intervalley phonon scattering rates in $In_{0.53}Ga_{0.47}As$, the influence of electric field upon the hot carrier behavior required comprehensive investigation. To capitalize upon the increasingly thorough understanding of the proof-of-principle structure with a 250 nm InGaAs absorber, alteration of the electric field strength across the absorber was accomplished with minimal disruption by decreasing

the absorber thickness. The resulting PL analysis not only evidenced enhanced hot carrier temperatures as a result of enhanced electric field strength, it provided an important demonstration that the phonon bottleneck effect and the intervalley mechanisms are capable of coexisting – and that electric field strength correlates with stronger power dependence without loss of robust low power hot carrier maintenance.

Future designs for the next stage of this project are underway, with design considerations based upon the experimental results presented in this dissertation. Through analysis of the complex band structure to predict tunneling via the imaginary components and better analysis of the precise momentum and energy of upper valleys at the interface to better determine potential barriers for the real space transfer, a proposed n^+ GaAs top barrier/$Al_{0.16}Ga_{0.84}As$/p^+ GaAs structure is anticipated to feature both the desired intervalley scattering supported hot carrier behavior and substantially improved extraction. Additionally, with a more comprehensive understanding of the intervalley mechanisms there is renewed interest in the InAs MQW devices, which continue to demonstrate excellent potential for further development as hot carrier devices.

The challenge that remains for future work is development of an efficient extraction pathway from the high energy carrier populations in the upper valleys of the conduction band. A fully operational hot carrier solar cell will feature enhanced photovoltage and maintain sufficient photocurrent to exceed the single gap efficiency limit. While the studies presented in this dissertation provide a leap forward in practical implementation of hot carrier devices, the remaining steps along this path continue to be non-trivial. Nevertheless, the field of hot carrier studies is progressing rapidly, and with a firm

theoretical and experimental foundation now in place there is genuine promise here for major improvements in solar cell efficiency.

Appendix

Device Processing

The samples examined throughout this thesis were grown by molecular beam epitaxy at the University of Oklahoma via the efforts of Dr. Tetsuya D. Mishima and Prof. Michael B. Santos. The structures are grown epitaxially on half or quarter fractions of 2" substrate wafers, too large for convenient measurement with the size of the available equipment and not prepared for electrical connection. Furthermore, a GaSb cap layer was present in the InAs quantum well samples discussed in Chapter 3, and it is desirable to remove this during the processing steps to better ensure the sample operates as designed.

Device fabrication was performed primarily through the resources of the OU-MREC cleanroom, and consisted of photolithography-enabled wet etching for removing cap layers and etching of a device mesa, photolithography-enabled contact deposition via thermal evaporation, and finalized with rapid thermal annealing of the contacts. Photolithography is a standard microfabrication technique, employing a coating of a photoresist substance sensitive to exposure to ultraviolet (UV) light which may be precisely manipulated to allow etching or metallization only upon non-coated parts of the sample. The UV exposure was at 365 nm wavelength, and performed with a MJB3 Mask Aligner.

An appropriately sized sample from the wafer through the use of a diamond scriber upon the substrate side of the wafer, most often 7 mm on each side to allow for simple processing of a 5 mm by 5 mm device, or 10 mm by 7 mm to fit a cluster of 2.5 mm or 1 mm scale devices for simultaneous processing. The samples are cleaned through

successive three-minute ultrasonic baths in acetone and either methanol or isopropyl alcohol, rinsed in deionized water and dried with nitrogen gas. The samples are dehydrated at 95 ℃ for five minutes, then spin coating with photoresist at 3000 rpm for 60 seconds is performed to ensure a consistent thickness across the top of the sample, enabling consistent selective removal via photoresist developer.

The samples discussed in Chapter 3 and Chapter 4 were processed with the aid of photoresist AZ 5214E, a positive photoresist that becomes soluble to the AZ 300 MIF developer solution when exposed to light. A softbake of the coated sample at 95 ℃ for 60 seconds mitigates the photoresist coating's tendency to stick to the mask, which protects a desired portion of the photoresist from the following 10 second UV light exposure which renders the illuminated AZ 5214E sections vulnerable to the developer. A 60 second exposure to the developer will suffice to remove the vulnerable photoresist regions without dissolving the photoresist protected by the mask. This positive photoresist process was employed to define a mesa for each device, via aligning the blank 'reverse' squares available on the mask rather than the finger or annular contact patterns, allowing selective wet etching of regions without a photoresist coating. This ensures accurate determination of device area and electronically separates multiple devices created on the same sample. The remaining photoresist is later removed through the stripper solution AZ NMP Rinse, to which the photoresist is soluble without the selectivity of the developer.

AZ 5214E may be employed as a negative photoresist as well, rendering the mask-protected region selectively vulnerable to the developer through the addition of additional fabrication steps. After the softbake, and a 2.5 second UV exposure with the

desired mask pattern, a post exposure baking of 120 ℃ for 90 seconds will initiate crosslinking of polymers in the exposed region that hardens the photoresist. Then a 50 second UV exposure without the use of a mask renders the unmodified positive photoresist vulnerable to the developer, with 60 seconds of development time selectively removing the region protected by the mask in the 2.5 second UV exposure step. This facilitated deposition of contacts, leaving a finger or annular pattern uncovered by photoresist, allowing metallization of the sample through thermal evaporation to only produce contacts in that pattern, as the stripper will remove the remaining photoresist and any metal deposited atop it.

Later samples discussed in Chapter 5 and Chapter 6 employed AZ nLOF 2020 for the as a negative photoresist instead, while continuing with the prior procedure for positive photoresist. This allows for faster device processing, only requiring a single UV exposure step. Spincoating at 3000 rpm for 60 seconds followed by a 110 ℃ softbake for 60 seconds will prepare the sample. Then a 4 second UV exposure and a 60 second post exposure bake at 110 ℃ will render the masked region vulnerable to the developer. Development with AZ 300 MIF takes 90 seconds.

Wet etching steps were performed after positive photolithography steps to protect the device region and only etch the mesa. Removal of a GaSb cap layer as previously discussed was selectively performed with NH_3OH : H_2O (1:10) for 1 minute. Mesa etching was performed with HF : H_2O_2 : H_2O (2:1:40), calibrated for each structure to etch to the desired depth: below the p^+ layer for mesa etching, though this etchant was also employed for etching only the n^+ layer of the $GaAs_{0.49}Sb_{0.51}$/

$In_{0.53}Ga_{0.47}As/In_{0.52}Al_{0.48}As/InP$ structure in Chapter 5 to test the effect of the top layer on the photoluminescence spectrum (see Figure 5.10).

Contact deposition was performed with an Edwards E306A Thermal Evaporator. Samples are mounted behind a shutter in a chamber that is pumped to vacuum pressures ($< 10^{-6}$ torr), and a small supply of contact metal is heated electrically within metal crucibles to melt and slowly evaporate. This provides an electrically-controlled vapor flux from the source material to the sample undergoing metallization, with the shutter providing a means to swiftly end the deposition at the desired thickness. In/Au as a top contact and Ni/AuGe (12% Ge by weight) as a bottom contact served as for the InAs quantum well structures in Chapter 3 and the proof-of-concept InGaAs heterostructure in Chapter 4.

With further modification of the top layer from InAlAs to $AlAs_{0.8}Sb_{0.2}$ and $GaAs_{0.49}Sb_{0.51}$, the contacts were developed further, as discussed in Chapter 5. The bottom p-contact became Au/Zn/Au, while the top n-contact had additional Au thickness added for $AlAs_{0.8}Sb_{0.2}$, and for $GaAs_{0.49}Sb_{0.51}$ was altered entirely to Ni/AuGe/Ni/Au. Equipment malfunction ultimately drove a reliance upon the more advanced Lesker Nano36 Evaporator, although evaporation of In or Zn was not permitted. This drove development of Ti/Au as an alternative back contact for p-InP, which proved to be a reasonable alternative to Au/Zn/Au.

Rapid thermal annealing (RTA) as a final processing step permits improved alloying and adhesion of the contacts, but due to the short timescale of heating and swift gas-enhanced cooling provided by the Heatpulse 610, it is viable to avoid issues such as dopant drift is that are detrimental to device performance. Depending on the device, the

process is not guaranteed to be beneficial. 300 °C for 60 seconds was helpful for the InAs quantum well samples and the majority of the InGaAs absorber heterostructures, but experimentation with RTA settings for the $AlAs_{0.8}Sb_{0.2}/In_{0.53}Ga_{0.47}As/In_{0.52}Al_{0.48}As/InP$ device proved to be less effective than neglecting the RTA step altogether.

A portion of the samples were wire bonded for long term electrical connections through the use of copper plates and conductive epoxy for back contacts, and gold wires bonded to the top contacts through conductive epoxy. Non-conductive epoxy provides a means to attach the gold wire to an electrically isolated bus bar soldered to a more stable wire with a standard male connector sized to the needs of the measuring equipment. Soldering such a wire directly to the copper plate provides equivalent electrical contact for the back contact. Where this is a reliable for large devices, albeit slow due to necessary epoxy cure times, greater precision in wiring is a necessity for small devices, especially when fabricated in close proximity on one sample.

The majority of the samples were instead measured using a series of custom sample holders with annular connective regions sized to the mask patterns employed for photolithographic fabrication. The screw alignment of the sample holders is also matched to the cryostat requirements, with substantial benefits to the ease and reliability of experimental setup compared to the non-standardized copper plates. While there is a risk of sample damage in the case of repeated careless mounting efforts, with due caution these sample holders became a fast and effective means of forming the desired electrical connections.

List of Publications

Peer-reviewed Journal Papers

Dorman, Kyle R., Vincent R. Whiteside, David K. Ferry, Tetsuya D. Mishima, Israa Yusuf, Hamidreza Esmaielpour, Michael B. Santos, and Ian R. Sellers. "Electric Field and Its Effect on Hot Carriers in InGaAs Valley Photovoltaic Devices." *IEEE Journal of Photovoltaics* 12, no. 5 (2022): 1175-183.

Dorman, Kyle R., Vincent R. Whiteside, David K. Ferry, Israa G. Yusuf, Tanner J. Legvold, Tetsuya D. Mishima, Michael B. Santos, Stephen J. Polly, Seth M. Hubbard, and Ian R. Sellers. "Toward Hot Carrier Extraction in Intervalley Photovoltaic Devices." *ACS Applied Energy Materials* 5, no. 9 (2022): 11159–1166.

Esmaielpour, Hamidreza, Brandon K. Durant, **Kyle R. Dorman**, Vincent R. Whiteside, Jivtesh Garg, Tetsuya D. Mishima, Michael B. Santos, Ian R. Sellers, Jean-François Guillemoles, and Daniel Suchet. "Hot Carrier Relaxation and Inhibited Thermalization in Superlattice Heterostructures: The Potential for Phonon Management." *Applied Physics Letters* 118, no. 21 (2021): 213902.

Esmaielpour, Hamidreza, **Kyle R. Dorman**, David K. Ferry, Tetsuya D. Mishima, Michael B. Santos, Vincent R. Whiteside, and Ian R. Sellers. "Exploiting Intervalley Scattering to Harness Hot Carriers in III–V Solar Cells." *Nature Energy* 5, no. 4 (2020): 336-43.

Whiteside, Vincent R., Hamidreza Esmaielpour, Tetsuya D. Mishima, **Kyle R. Dorman**, Michael B. Santos, David K. Ferry, and Ian R. Sellers. "The Role of Intervalley Phonons in Hot Carrier Transfer and Extraction in Type-II InAs/AlAsSb Quantum-Well Solar Cells." *Semiconductor Science and Technology* 34, no. 9 (2019): 94001.

Conferences and Symposiums

Dorman, Kyle R., Vincent R. Whiteside, David K. Ferry, Tetsuya D. Mishima, Hamidreza Esmaielpour, Michael B. Santos, and Ian R. Sellers. “Electric Field and its Effect on Hot Carriers in InGaAs Valley Photovoltaic Devices.” 49th IEEE Photovoltaic Specialists Conference. Philadelphia, PA, 2022.

Dorman, Kyle R., Vincent R. Whiteside, David K. Ferry, Tetsuya D. Mishima, Israa G. Yusuf, Hamidreza Esmaielpour, Michael B. Santos, and Ian R. Sellers. “The Effect of Electric Field on Hot Carriers in InGaAs Valley Photovoltaic Devices.” 2022 Oklahoma Photovoltaic Institute Annual Symposium. Norman, OK, 2022.

Dorman, Kyle R., Hamidreza Esmaielpour, David K. Ferry, Vincent R. Whiteside, Tetsuya D. Mishima, Michael B. Santos, and Ian R. Sellers. “The Impact of InGaAs Absorber Thickness on Intervalley Extraction in Hot Carrier Solar Cells.” 21st International Conference on Molecular Beam Epitaxy. Virtual Conference, 2021.

Dorman, Kyle R., Vincent R. Whiteside, David K. Ferry, Israa G. Yusuf, Tanner J. Legvold, Tetsuya D. Mishima, Michael B. Santos, Stephen J. Polly, Seth M. Hubbard, and Ian R. Sellers. “The Role of Valley Degeneracy in Carrier Extraction in Valley

Photovoltaic Solar Cells." 48th IEEE Photovoltaic Specialists Conference. Virtual Conference, 2021.

Dorman, Kyle R., Hamidreza Esmaielpour, David K. Ferry, Tetsuya D. Mishima, Michael B. Santos, Vincent R. Whiteside, Brandon K. Durant, and Ian R. Sellers. "Valley Photovoltaics: An Alternative Approach Towards a Practical Hot Carrier Solar Cell." APS March Meeting 2021. Virtual Conference, 2021.

Whiteside, Vincent R., Hamidreza Esmaielpour, **Kyle R. Dorman**, Tetsuya D. Mishima, David K. Ferry, Michael B. Santos, and Ian R. Sellers. "The Role of Intervalley Phonons in Hot Carrier Transfer and Extraction in InAs/AlAsSb Quantum Well Solar Cells." 35th North American Conference on Molecular Beam Epitaxy. Ketchum, ID, 2019.

Dorman, Kyle R., Vincent R. Whiteside, Hamidreza Esmaielpour, Tetsuya D. Mishima, Michael B. Santos, David K. Ferry, and Ian R. Sellers. "Inhibited Hot Carrier Thermalization in Type-II Quantum Wells: A Practical Route to Hot Carrier Solar Cells?" 2019 Oklahoma Photovoltaic Institute Annual Symposium. Tulsa, OK, 2019.